National Library of Canada
Bibliothèque nationale du Canada

Canadian Theses Service
Services des thèses canadiennes

Ottawa, Canada
K1A 0N4

CANADIAN THESES

THÈSES CANADIENNES

NOTICE

The quality of this microfiche is heavily dependent upon the quality of the original thesis submitted for microfilming. Every effort has been made to ensure the highest quality of reproduction possible.

If pages are missing, contact the university which granted the degree.

Some pages may have indistinct print especially if the original pages were typed with a poor typewriter ribbon or if the university sent us an inferior photocopy.

Previously copyrighted materials (journal articles, published tests, etc.) are not filmed.

Reproduction in full or in part of this film is governed by the Canadian Copyright Act, R.S.C. 1970, c. C-30. Please read the authorization forms which accompany this thesis.

AVIS

La qualité de cette microfiche dépend grandement de la qualité de la thèse soumise au microfilmage. Nous avons tout fait pour assurer une qualité supérieure de reproduction.

S'il manque des pages, veuillez communiquer avec l'université qui a conféré le grade.

La qualité d'impression de certaines pages peut laisser à désirer, surtout si les pages originales ont été dactylographiées à l'aide d'un ruban usé ou si l'université nous a fait parvenir une photocopie de qualité inférieure.

Les documents qui font déjà l'objet d'un droit d'auteur (articles de revue, examens publiés, etc.) ne sont pas microfilmés.

La reproduction, même partielle, de ce microfilm est soumise à la Loi canadienne sur le droit d'auteur, SRC 1970, c. C-30. Veuillez prendre connaissance des formules d'autorisation qui accompagnent cette thèse.

THIS DISSERTATION
HAS BEEN MICROFILMED
EXACTLY AS RECEIVED

LA THÈSE A ÉTÉ
MICROFILMÉE TELLE QUE
NOUS L'AVONS REÇUE

NL 339 (r. 86/01)

Canada

National Library of Canada
Bibliothèque nationale du Canada

Canadian Theses Division
Division des thèses canadiennes

Ottawa, Canada
K1A 0N4

0-315-24812-2

PERMISSION TO MICROFILM — AUTORISATION DE MICROFILMER

• Please print or type — Écrire en lettres moulées ou dactylographier

Full Name of Author — Nom complet de l'auteur

ARDKIA NATHAN

Date of Birth — Date de naissance
15th June 1957

Country of Birth — Lieu de naissance
Penang, W. Malaysia

Permanent Address — Résidence fixe
~~H, Tan Iu Ghee Road~~
~~Penang, W. Malaysia~~
Department of Electrical Engineering
University of Alberta
Edmonton, Canada T6G2E1

Title of Thesis — Titre de la thèse

Numerical Analysis of MOS Magnetic Field Sensors

University — Université
University of Alberta

Degree for which thesis was presented — Grade pour lequel cette thèse fut présentée
Master of Science

Year this degree conferred — Année d'obtention de ce grade
Fall, 1984

Name of Supervisor — Nom du directeur de thèse
Drs. H.P. Baltes
H.G. Schmidt-Weinmar

Permission is hereby granted to the NATIONAL LIBRARY OF CANADA to microfilm this thesis and to lend or sell copies of the film.

The author reserves other publication rights, and neither the thesis nor extensive extracts from it may be printed or otherwise reproduced without the author's written permission.

L'autorisation est, par la présente, accordée à la BIBLIOTHÈQUE NATIONALE DU CANADA de microfilmer cette thèse et de prêter ou de vendre des exemplaires du film.

L'auteur se réserve les autres droits de publication; ni la thèse ni de longs extraits de celle-ci ne doivent être imprimés ou autrement reproduits sans l'autorisation écrite de l'auteur.

October 17th 1984

Date

Signature

NL-91 (4/77)

THE UNIVERSITY OF ALBERTA

NUMERICAL ANALYSIS OF MOS MAGNETIC FIELD SENSORS

by

AROKIA NATHAN

A THESIS

SUBMITTED TO THE FACULTY OF GRADUATE

STUDIES AND RESEARCH IN PARTIAL FULFILMENT

OF THE REQUIREMENTS FOR THE DEGREE OF

MASTER OF SCIENCE

DEPARTMENT OF ELECTRICAL ENGINEERING

EDMONTON, ALBERTA

FALL, 1984

Re M.Sc Thesis (1984)

Copyright and Reprint Permission

for the publications contained in Appendices D, E, F and H of the M.Sc. thesis entitled

"Numerical Analysis of MOS Magnetic Field Sensors"

by A Nathan
Dept. of Electrical Engineering
Univ. of Alberta

Fall 1984.

For Appendix D:

1983 International Electron Devices Meeting
TECHNICAL DIGEST

Papers have been printed without editing as received from the authors.

All opinions expressed in the Digest are those of the authors and are not binding on The Institute of Electrical & Electronics Engineers, Inc.

Publication of a paper in this Digest in no way is intended to preclude publication of a fuller account of the paper elsewhere.

Copies of available volumes of this Digest may be obtained from The Institute of Electrical & Electronics Engineers, Inc., 445 Hoes Lane, Piscataway, N.J.
Library of Congress Catalog Card Number: 78-20188.

IEEE Catalog Number: 83CH1973-7

Copyright and Reprint Permissions: Abstracting is permitted with credit to the source. Libraries are permitted to photocopy beyond the limits of U.S. copyright law for private use of patrons those articles in this volume that carry a code at the bottom of the first page, provided the per-copy fee indicated in the code is paid through the Copyright Clearance Center, 21 Congress St., Salem, MA 01970. Instructors are permitted to photocopy isolated articles for noncommercial classroom use without fee. For other copying, reprint or republication permission, write to Director, Publishing Services, IEEE, 345 E. 47 St., New York, NY 10017. All rights reserved.
Copyright ©1983 by The Institute of Electrical and Electronics Engineers, Inc.

POOR PRINT
Epreuve illisible

For Appendix E

Headquarters Staff

Publications Department

IEEE TRANSACTIONS ON ELECTRON DEVICES is published monthly by The Institute of Electrical and Electronics Engineers, Inc. Headquarters: 345 East 47 Street, New York, NY 10017. Responsibility for the contents rests upon the authors and not upon the IEEE, the Society/Group, or its members. IEEE Service Center (for orders, subscriptions, address changes): Region/Section/Student Services: 1-800-678-IEEE. Telephone: 212-705-7900. To obtain IEEE information (212-705-8 extension): Information: 7900, General Manager: 7910, Controller: 7748, Education Services: 7860, IEEE Network Operations Center: 7870, Technical Services: 7890, IEEE Service Center: 201-981-0060, Professional Services: Washington, DC: 202-785-0017, NY Telecopier: 212-705-7589. Telex: 236-411 (International messages only). Individual copies: IEEE members $6.00 (first copy only), nonmembers $12.00 per copy (first copy only). Subscription prices: IEEE members, dues plus Society fee. Price for nonmembers on request. Available in microfiche and microfilm.

Copyrights and Reprint Permissions: Abstracting is permitted with credit to the source. Libraries are permitted to photocopy beyond the limits of U.S. Copyright law for private use of patrons those articles that carry a code at the bottom of the first page, provided the per-copy fee indicated in the code is paid through the Copyright Clearance Center, 29 Congress Street, Salem, MA 01970. For other copying, reprint or republication permission, write to Director, Publishing Services, IEEE, 345 East 47 Street, New York, NY 10017. All rights reserved. Copyright © 1984 by The Institute of Electrical and Electronics Engineers, Inc.

Second-class postage paid at New York, NY and additional mailing offices. Postmaster: Send address changes to IEEE, 445 Hoes Lane, Piscataway, NJ 08854.

IEEE MAGNETICS SOCIETY

1884 1984 A CENTURY OF ELECTRICAL PROGRESS

For Appendix F.

The Magnetics Society is an association of IEEE members with professional interest in the field of magnetics. All IEEE members are eligible for membership and will receive this TRANSACTIONS upon payment of the annual Society membership fee of $7.00. For information on joining, write the IEEE at the address below. It is possible for members of other professional societies to become Society affiliates as provided by the IEEE Bylaws.

Officers

President
C. E. JOHNSON, JR.
Vertimag Systems Corp.
815 14th Ave. SE
Minneapolis, MN 55414

Vice President
A. B. SMITH
Digital Equipment Corp.
77 Reed Road
Hudson, MA 01749

Secretary-Treasurer
R. M. JOSEPHS
Naval Air Development Center
Code 5023
Warminster, PA 18974

Past President
J. M. LOMMEL
General Electric Co. R&D
P.O. Box 8
Schenectady, NY 12301

Administrative Committee

Term Ending 12/31/84		*Term Ending 12/31/85*		*Term Ending 12/31/86*	
I. A. BEARDSLEY	R. M. JOSEPHS	G. BATE	F. B. HAGEDORN	A. I. BRAGINSKI	B. J. LANGLAND
S. H. CHARAP	J. P. LAZZARI	H. N. BERTRAM	K. LEE	C. E. JOHNSON, JR.	R. O. McCARY
R. B. CLOVER	F. E. LUBORSKY	P. P. BIRINGER	Y. SAKURAI	J. H. JUDY	R. W. PATTERSON
E. DELLA TORRE	E. J. TOROK	D. I. GORDON	J. W. SHILLING	M. H. KRYDER	A. B. SMITH

Department Chairpersons

S. H. CHARAP, *Publications*; D. I. GORDON, *Technical Committees*; G. BATE, *Conference Executive Committee*; D. M. WILSON, *Chapters*; E. J. TOROK

Standing Committee Chairpersons

Awards, P. P. BIRINGER
Centennial Committee, F. J. FRIEDLAENDER
Constitution and Bylaws, F. J. FRIEDLAENDER
Distinguished Lecturer Program, E. E. LUBORSKY
Education, E. DELLA TORRE
Finance, J. W. SHILLING
Membership, B. J. LANGLAND
Nominations, J. M. LOMMEL
Planning, C. E. JOHNSON, JR.
Publicity, R. M. JOSEPHS
Scholarship Program Director, R. B. CLOVER
Standards, R. O. McCARY
Equipment Grant Program, G. BATE

Technical Committee Chairpersons

Amorphous Magnetic Materials, R. HASEGAWA
Control and Power Processing, J. D. HARNDEN, JR.
Cryoelectric Engineering, A. I. BRAGINSKI
Electronic Transformers, R. P. CAREY
Heating by Induction, P. P. BIRINGER
High Frequency Properties of Magnetic Materials, C. VITTORIA
Large Magnet Technology, P. C. MARSTON
Electromagnetic Launch Technology and Levitated Transportation, H. H. KOLM
Magnetics in Life Sciences, R. B. FRANKEL
Magnetic Recording, D. SPELIOTIS
Magnetic Separation, D. R. KELLAND
Magnetometers and Measurements, D. I. GORDON
Magnetooptics, B. E. MACNEAL
Memories, C. D. LUSTIG
Permanent Magnets, R. J. PARKER
Relay Magnetics, D. D. ENGELBRACH
Soft Core Materials, K. J. OVERSHOTT

Representatives

Committee on Man and Radiation, R. B. FRANKEL
Committee on Research and Development, E. W. PUGH
Energy Committee, V. KUSKO
Alternate, D. I. GORDON
Environmental Quality Committee, L. F. SHIVA

IEEE TRANSACTIONS[a] ON MAGNETICS

Editor in Chief
S. H. CHARAP
Department of Electrical and Computer Engineering
Carnegie Mellon University
Schenley Park
Pittsburgh, PA 15213

Reviews Editor
C. E. PATTON
Department of Physics
Colorado State University
Fort Collins, CO 80523

Reviews Editor
R. W. PATTERSON
Hewlett Packard Labs
1651 Page Mill Rd.
Palo Alto, CA 94304

Advances in Magnetics Editor
K. LEE
The Southwall Corporation
3964 East Bayshore Road
Palo Alto, CA 94303

Newsletter Editor
R. M. JOSEPHS
Naval Air Development Center
Code 5023
Warminster, PA 18974

THE INSTITUTE OF ELECTRICAL AND ELECTRONICS ENGINEERS, INC.

Officers

RICHARD J. GOWEN, *President*
DONALD D. KING, *President-Elect*
HENRY L. BACHMAN, *Executive Vice President*
V. PRASAD KODALI, *Secretary*
CYRIL J. TUNIS, *Treasurer*
J. BARRY OAKES, *Vice President, Educational Activities*
RUSSELL C. DREW, *Vice President, Professional Activities*
JOSE B. CRUZ, JR., *Vice President, Publication Activities*
MERRILL W. BUCKLEY, JR., *Vice President, Regional Activities*
STEPHEN KAHNE, *Vice President, Technical Activities*
EMERSON W. PUGH, *Division IV Director*

Headquarters Staff

ERIC HERZ, *Executive Director and General Manager*
ELWOOD K. GANNETT, *Deputy General Manager*
THOMAS W. BARNETT, *Controller*
DONALD CHRISTIANSEN, *Editor of Spectrum*
IRVING ENGELSON, *Staff Director, Technical Activities*
LEO FANNING, *Staff Director, Professional Activities*
SAVA SHERR, *Staff Director, Standards*
DAVID L. STAIGER, *Staff Director, Publishing Services*
DONALD L. SUPPERS, *Staff Director, Field Services*
CHARLES F. STEWART, JR., *Staff Director, Administrative Services*
THOMAS C. WHITE, *Staff Director, Public Information*
JOHN F. WILHELM, *Staff Director, Educational Services*

Publications Department

Production Managers: ANN H. BURGMEYER, CAROLYNE ELENOWITZ, GAIL S. FERENC
Associate Editor: BARBARA A. SOMOGYI

IEEE TRANSACTIONS ON MAGNETICS is published bimonthly by The Institute of Electrical and Electronics Engineers, Inc., 345 East 47 Street, New York, NY 10017. Responsibility for the contents rests upon the authors and not upon the IEEE, the Society, or its members. **IEEE Service Center** (for orders, subscriptions, address changes, Region/Section/Student): 445 Hoes Lane, Piscataway, NJ 08854. **Telephones:** Headquarters 212-705 + extension: Information—7900, General Manager—7910, Controller—7748, Educational Services—7860, Publishing Services—7560, Standards—7960, Technical Services—7890. IEEE Service Center 201-981-0060. Professional Services: Washington Office 202-785-0017. **Telecopier:** 212-752-4929. **Telex:** 236-411 (International messages only). Individual copies: IEEE members $17.50 (first copy only), nonmembers $35.00 per copy. Annual subscription price: IEEE members, dues plus Society fee. Price for nonmembers on request. Available in microfiche and microfilm. **Copyright and Reprint Permissions:** Abstracting is permitted with credit to the source. Libraries are permitted to photocopy beyond the limits of U.S. Copyright Law for private use of patrons: (1) those post-1977 articles that carry a code at the bottom of the first page, provided the per copy fee indicated in the code is paid through the Copyright Clearance Center, 29 Congress Street, Salem, MA 01970; (2) pre-1978 articles without fee. Instructors are permitted to photocopy isolated articles for noncommercial classroom use without fee. For other copying, reprint, or republication permission, write to Director, Publishing Services at IEEE Headquarters. All rights reserved. Copyright © 1984 by The Institute of Electrical and Electronics Engineers, Inc. Printed in U.S.A. Second-class postage paid at New York, NY and at additional mailing offices. **Postmaster:** Send address changes to IEEE, 445 Hoes Lane, Piscataway, NJ 08854.

IEEE JOURNAL OF SOLID-STATE CIRCUITS

1884 1984
A CENTURY OF ELECTRICAL PROGRESS

for Appendix H.

IEEE JOURNAL OF SOLID-STATE CIRCUITS is published by the IEEE Solid State Circuits Council on behalf of the following Groups/Societies: S-Circuits and S-Communications, S-Computer, S-Electron Devices, S-Microwave Theory and Techniques, S-Components, Hybrids, and Manufacturing Technology, G-Sonics, Ultrasonics, and S-Quantum Electronics and Applications. For information on receiving this JOURNAL, write to the IEEE Service Center at the address below.

SOLID-STATE CIRCUITS COUNCIL

President
R. G. MEYER
EECS—Cory Hall
Univ. California
Berkeley, CA 94720

Vice President
E. K. BULLOW
STC Computer Research Corp.
8000 Central Expressway
Santa Clara, CA 95050

Secretary
G. T. BALDWIN
Hewlett-Packard Lab.
1501 Page Mill Road
Bldg. 29-A
Palo Alto, CA 94304

Treasurer
R. N. BERGLUND
[illegible] Corp.
[illegible] S.W. 198th Ave.
Aloha, OR 97007

Representatives

S-CAS
B. A. WOOLLEY
Bell Lab.
Holmdel, NJ 07733

S-COM
S. U. PILLAI
Signal Processing Res. Dept.
Bell Lab., Rm. 4D-633
Holmdel, NJ 07733

G-SC
E. F. CLAIBORNE
Texas Instruments, Inc.
13500 N. Central Exp.
P.O. Box 5936
Dallas, TX 75222

S-ED
R. C. JAEGER
Elec. Eng. Dept.
207 Dunstan Hall
Auburn Univ.
Auburn, AL 36849

S-ED
W. G. OLDHAM
Univ. California
Berkeley, CA 94720

D. O. PEDERSON
EECS—Cory Hall
Univ. California
Berkeley, CA 94720

E. IVANES
Eaton Electric
1091 Bayport Ave.
San Carlos, CA 94070

L. R. MEEKER
Bell Lab.
555 Union Blvd.
Allentown, PA 18103

S. TROBWASSER
IBM T. J. Watson Research Center
P.O. Box 218
Yorktown Heights, NY 10598

B. L. GREGORY
Dep. 2140
Sandia Lab.
Albuquerque, NM 87115

S-MTT
A. G. GELSOMINI
U.S. Army Electron. Command
Attn: DRSEL-TL-IM
Fort Monmouth, NJ 07703

C. T. GREITING
Hughes Research Lab.
3011 Malibu Canyon Rd.
Malibu, CA 90265

S-CHMT
J. LENOYAN
Texas A&M Univ.
Elec. Eng. Dept.
College Station, TX 77843

L. J. PALKUTI
ARACOR
1223 E. Arques Ave.
Sunnyvale, CA 94086

S-QEA
R. C. EDEN
Science Center
Rockwell Int.
P.O. Box 1085
Thousand Oaks,
CA 91360

EXEC. COMM.
ISSCC CHAIRMAN
E. A. A. RAPER
Electron. Lab.
General Electric Co.
Electronics Park
Box 1122
Syracuse, NY 13701

IEEE JOURNAL OF SOLID-STATE CIRCUITS

Editor
W. D. PRICE
A22/965.2
General Technol. Div.
IBM Corp.
Essex Junction, VT 05452

Associate Editors

H. J. BOLL
Bell Lab.
Murray Hill, NJ 07974

B. J. HOSTICKA
Lehrstuhl Bauelemente
der Electrotechnik
Univ. Dortmund
P.O. Box 500500
D-4600 Dortmund 50
Germany

M. NAGATA
Central Research Lab.
Hitachi Ltd.
Tokyo, Japan

R. HEWES
Central Research Lab.
Texas Instruments, Inc.
Dallas, TX 75222

R. MUELLER
Siemens AG, Dep. BAT
Balanstr. 73
D-8000 Munich 80
West Germany

B. A. WOOLLEY
Rm. 4D-631
Bell Telephone Labs.
Holmdel, NJ 07733

THE INSTITUTE OF ELECTRICAL AND ELECTRONICS ENGINEERS, INC.

Officers

JAMES B. OWENS, *President*
RICHARD J. GOWEN, *President-Elect*
CHARLES A. ELDON, *Executive Vice President*
V. PRASAD KODALI, *Secretary*
CYRIL J. TUNIS, *Treasurer*
J. BARRY OAKES, *Vice President, Educational Activities*
EDWARD J. DOYLE, *Vice President, Professional Activities*
G. P. RODRIGUE, *Vice President, Publication Activities*
MERRILL W. BUCKLEY, JR., *Vice President, Regional Activities*
JOSE B. CRUZ, JR., *Vice President, Technical Activities*
STEPHEN KAHNE, *Division I Director*

Headquarters Staff

ERIC HERZ, *Executive Director and General Manager*
ELWOOD K. GANNETT, *Deputy General Manager*
THOMAS W. BARTLETT, *Controller*
DONALD CHRISTIANSEN, *Editor of Spectrum*
IRVING ENGELSON, *Staff Director, Technical Activities*
LEO FANNING, *Staff Director, Professional Activities*
SAVA SHERR, *Staff Director, Standards*
DAVID F. STAMAR, *Staff Director, Publishing Services*
CHARLES F. STEWART, JR., *Staff Director, Administration Services*
DONALD L. SUPPLEE, *Staff Director, Field Services*
THOMAS C. WHITE, *Staff Director, Public Information*
JOHN F. WITHERS, *Staff Director, Educational Services*

Publications Department

Production Managers: ANN H. BURGMEYER, CAROLYNE ELENOWITZ, GAIL S. FERENC
Associate Editor: MARY E. GRANGETIA

IEEE JOURNAL OF SOLID-STATE CIRCUITS is published bimonthly by The Institute of Electrical and Electronics Engineers, Inc. **Headquarters:** 345 East 47th Street, New York, NY 10017 U.S.A. Responsibility for the contents rests upon the authors and not upon the IEEE, the Group/Society, or its members. **IEEE Service Center** (for orders, subscriptions, address changes, Region/Section/Student Services): 445 Hoes Lane, Piscataway, NJ 08854. **Telephones:** Headquarters 212-705 (extension: Information -7900), General Manager -7910, Controller -7748, Educational Services -7860, Publishing Services -7560, Standards -7960, Technical Services -7890, IEEE Service Center 201-981-0060, Professional Services: Washington Office 202-785-0017. **NY Telecopier:** 212-752-4929. **Telex:** 236-411 (International messages only). Individual copies: IEEE members $6.00 (first copy only), nonmembers $12.00 per copy. Annual subscription price: IEEE members, dues plus Group/Society fee. Price for nonmembers on request. Available in microfiche and microfilm. **Copyright and Reprint Permissions:** Abstracting is permitted with credit to the source. Libraries are permitted to photocopy beyond the limits of U.S. Copyright law for private use of patrons: (1) those post-1977 articles that carry a code at the bottom of the first page, provided the per-copy fee indicated in the code is paid through the Copyright Clearance Center, 29 Congress St., Salem, MA 01970; (2) pre-1978 articles without fee. Instructors are permitted to photocopy isolated articles for noncommercial classroom use without fee. For other copying, reprint, or republication permission, write to Director, Publishing Services at IEEE Headquarters. All rights reserved. Copyright © 1984 by the Institute of Electrical and Electronics Engineers, Inc. Printed in U.S.A. Second-class postage paid at New York, NY and at additional mailing offices. **Postmaster:** Send address changes to IEEE, 445 Hoes Lane, Piscataway, NJ 08854.

THE UNIVERSITY OF ALBERTA

RELEASE FORM

NAME OF AUTHOR Arokia Nathan

TITLE OF THESIS Numerical Analysis of MOS Magnetic Field Sensors

DEGREE FOR WHICH THESIS WAS PRESENTED Master of Science

YEAR THIS DEGREE GRANTED Fall 1984

Permission is hereby granted to THE UNIVERSITY OF ALBERTA LIBRARY to reproduce single copies of this thesis and to lend or sell such copies for private, scholarly or scientific research purposes only.

The author reserves other publication rights, and neither the thesis nor extensive extracts from it may be printed or otherwise reproduced without the author's written permission.

(SIGNED) .....

PERMANENT ADDRESS:

Dept. of Electrical Engineering
University of Alberta
Edmonton, Canada. Alta T6G 2E1

DATED Oct. 17 1984

1

THE UNIVERSITY OF ALBERTA

FACULTY OF GRADUATE STUDIES AND RESEARCH

The undersigned certify that they have read, and recommend to the Faculty of Graduate Studies and Research, for acceptance, a thesis entitled, "Numerical Analysis of MOS Magnetic Field Sensors," submitted by Arokia Nathan in partial fulfillment of the requirements for the degree of Master of Science.

(Supervisors)

Date 17th. October 1984

To My Mother and Father

Abstract

Numerical solutions in two dimensions have been computed, for the system of coupled nonlinear partial differential equations which govern drift, diffusion, electrostatic potential, generation and recombination in a semiconductor device in the presence of a magnetic field. Two types of device geometries are considered ; (a) rectangular silicon slabs under doped and intrinsic conditions (b) split-drain N-channel MOSFET's operating in the linear region. The sensitivities associated with the various MOSFET channel geometries are studied and a circuit configuration incorporating a MOSFET magnetic field sensor is presented.

ACKNOWLEDGEMENTS

I express my utmost appreciation to my supervisors, Dr. H. P. Baltes and Dr. H. G. Schmidt-Weinmar for their invaluable help in setting the goals and providing continuous motivation, co-operation and direction during the course of this project.

It is a pleasure to thank Drs. W. Allegretto, L. Andor and A. M. J. Huiser for providing me with necessary assistance and the stimulating discussions throughout the course of the project. I would also like to thank Dr. I. Filanovsky for the useful ideas on electronic circuitry that incorporates sensors and Dr. A. M. Robinson for his invaluable time spent on this thesis. My sincere appreciation to Dr. M. Rudan for his creative suggestions and new ideas towards this thesis as well as future research.

Finally, I would like to give special thanks to Gabriele Baltes for typing the equations and proof reading the thesis.

Table of Contents

Chapter		Page
1.	INTRODUCTION	1
2.	CARRIER TRANSPORT IN MAGNETIC SEMICONDUCTORS	5
	2.1 The Current Density Equations	5
	2.2 Hall Angle	6
	2.3 Current Density Components	7
	2.4 Magnetic Field Effects	8
	2.4.1 Hall effect	8
	2.4.2 Carrier Deflection	9
	2.4.3 Magnetoconcentration	10
3.	ANALYSIS OF A SEMICONDUCTOR SLAB	12
	3.1 Basic Equations	12
	3.2 Boundary Conditions	15
	3.3 Models of Physical Parameters	17
	3.4 Numerical Method	19
	3.4.1 Discretisation	19
	3.4.2 Linearisation of the Field Equations	30
	3.4.3 Solution Procedure	32
	3.5 Results and Discussion	37
4.	ANALYSIS OF THE MOS MAGNETIC FIELD SENSOR	44
	4.1 Assumptions	44
	4.2 Basic Equations	46
	4.3 Boundary Conditions	49
	4.4 Carrier Mobility	51
	4.5 Numerical Method	52
	4.5.1 Discretisation	52

4.5.2 Solution Procedure 57

4.6 Results and Discussion 62

5. CONCLUSION AND OUTLOOK 71

6. REFERENCES 73

APPENDIX A (Linear Interpolation of the Variables p, n and ψ).....78

APPENDIX B (Matrix and Vector Elements for the Slab Boundaries).....82

APPENDIX C (Matrix and Vector Elements for the Bulk).....86

APPENDIX D (Reprint of Ref. [16]).....93

APPENDIX E (Copy of Manuscript of Ref. [17]).....97

APPENDIX F (Reprint of Ref. [38]).....101

APPENDIX G (Matrix and Vector Elements for the Split-Drain MOSFET).....104

APPENDIX H (Preprint of Ref. [43]).....107

APPENDIX I (Listing of Split-Drain MOSFET Simulation Program).....111

List of Figures

Figure		Page
Fig. 2.1	Geometrical representation of a semiconductor slab of length L, width W, and $\vec{B}$ is perpendicular to the device plane	11
Fig. 3.1	Basic slab geometry : semiconductor slab of length L, width W, and thickness, h. $\vec{B}$ is perpendicular to the drawing plane	14
Fig. 3.2	Two dimensional slab geometry	16
Fig. 3.3	A non-uniform rectangular grid	25
Fig. 3.4	Discretisation of equations (3.13)-(3.15) at the floating boundaries (3) and (4)	29
Fig. 3.5	Flow-chart of the Newton-SLOR method	36
Fig. 3.6	Equipotential curves for n-type Si device, V_a = 0.1 V, L = W = 100 μm and $\vec{B}$ = 1 t	39
Fig. 3.7	Current lines corresponding to Fig. 3.6	39
Fig. 3.8	Equipotential curves for p-type Si device, V_a = 0.1 V, L = W = 100 μm and $\vec{B}$ = 1 t	40
Fig. 3.9	Current lines corresponding to Fig. 3.8	40
Fig. 3.10	(a) Equipotential and current lines for an n-type Si device, L = 4W, B_z = 1 t, V = 0.1 V (b) Same as (a) but B_z = 2 t	41
Fig. 3.11	(a) Equipotential and current lines for an n-type Si device, L = W/4, B_z = 1 t (b) Equipotential and current lines for a p-type Si device, L = W/4, B_z = 2 t	41

Fig. 3.12	Electric field component ratio E_x/E_y across the middle ($y = L/2$) of the devices corresponding to Figs. 3.6, 3.10 (a) and 3.11 (a)	42
Fig. 3.13	Current deflection J_x/J_y across the middle ($y = L/2$) of the devices corresponding to Fig. 3.12	42
Fig. 3.14	Intrinsic Si square device ; $L = W = 4$ μm, $V_a = 1$ V, $B_z = 1$ t, $T = 500$°K (a) Hole concentration (b) Electron concentration (c) Space charge distribution (d) Equipotential and current lines	43
Fig. 4.1	Schematic of an N-channel MOSFET	45
Fig. 4.2	MOSFET channel geometry for a split-drain configuration	50
Fig. 4.3	Discretisation of (4.24) at (1)	54
Fig. 4.4	Discretisation of (4.24) at (2)	55
Fig. 4.5	Discretisation of (4.23) at (3)	56
Fig. 4.6	Flow-chart of the solution procedure	61
Fig. 4.7	Equipotential and current lines for $W = L = 4$ μm, $\vec{B} = 1$ t	64
Fig. 4.8	Equipotential and current lines for $W = L = 4$ μm, $\vec{B} = 3$ t	64
Fig. 4.9	Surface charge density for $W = L = 4$ μm, $\vec{B} = 1$ t	65
Fig. 4.10	Equipotential and current lines for $W = L = 4$ μm, $\vec{B} = 1$ t	66
Fig. 4.11	Equipotential and current lines for $W/L = 4$ μm/4 μm, $d = 1.4$ μm, $\vec{B} = 1$ t	67

Fig. 4.12	Equipotential and current lines for W/L = 22 μm/14 μm, d = 7.63 μm, $\vec{B}$ = 1 t	68
Fig. 4.13	Equipotential and current lines for W/L = 14 μm/22 μm, d = 4.9 μm, $\vec{B}$ = 1 t	68
Fig. 4.14	Relative current imbalance, δ as a function of magnetic field, B for a square channel NMOS, W = L = 25 μm, for different relative drain separations : d/W = 0.05 (curve a), d/W = 0.2 (curve b), d/W = 0.6 (curve c)	69
Fig. 4.15	Same as Fig. 4.14 but W/L = 5 μm/25 μm	69
Fig. 4.16	Same as Fig. 4.14 but W/L = 100 μm/25 μm	70
Fig. 4.17	Schematic of the square channel device in circuit	70

List of Symbols

Symbol	Name	Unit
$\vec{B}$	Magnetic induction vector	tesla
C_{ox}	Gate oxide capacitance per unit area	farad/cm^2
D_n	Electron diffusion constants	cm^2/sec
D_p	Hole diffusion constant	cm^2/sec
$\vec{E}$	Electric field vector	volt/cm
E_i	Intrinsic Fermi level	eV
E_t	Energy level of trap centres	eV
E_{Fp}	Bulk Fermi level	eV
I_D	Drain current	ampere
$\vec{J}_n$	Electron current density vector	amp/cm^2
$\vec{J}_p$	Hole current density vector	amp/cm^2
k	Boltzmann's constant	Joule/°K
L	Channel length	μm
n	Electron concentration	cm^{-3}
n_i	Intrinsic carrier concentration	cm^{-3}
N_A	Acceptor concentration	cm^{-3}
N_D	Donor concentration	cm^{-3}
N	Net doping density	cm^{-3}
p	Hole concentration	cm^{-3}
q	Electronic charge	coulomb
Q_n	Surface charge density	coulomb/cm^2
R	Net recombination rate	cm^{-3} sec^{-1}
T	Temperature	°Kelvin

List of Symbols (contd.)

Symbol	Name	Unit
t_{ox}	Oxide thickness	nm
V_G	Gate voltage	volt
V_D	Drain voltage	volt
V_s	Source voltage	volt
V_a	Applied voltage	volt
V_B	Substrate voltage	volt
V_{FB}	Flatband voltage	volt
W	Width of channel	μm
μ_n	Electron drift mobility	cm^2/volt-sec
μ_p	Hole drift mobility	cm^2/volt-sec
μ_n^*	Electron Hall mobility	$tesla^{-1}$
μ_p^*	Hole Hall mobility	$tesla^{-1}$
ϵ	Dielectric constant ($=\epsilon_o\epsilon_s$, for Si, $\epsilon_s=12$)	farad/cm
Θ	Hall angle	degree
ϕ_n	Electron quasi-Fermi potential	volt
ϕ_p	Hole quasi-Fermi potential	volt
τ_n	Electron lifetime in the bulk	sec
τ_p	Hole lifetime in the bulk	sec
ψ	Electrostatic potential	volt
$\vec{\nabla}$	Nabla operator	

1. INTRODUCTION

A magnetic field sensor (MFS) is an input transducer which converts the magnetic induction $\vec{B}$ into an electronic signal. Many MFS exploit the Lorentz force $\vec{F} = q(\vec{v} \times \vec{B})$ on electrons in a metal, a semiconductor or an insulator in some manner [1].

We can distinguish between direct and indirect MFS applications. In direct applications, the MFS gathers information about field magnitude and/or direction. These applications include [1,2]

i. measurement of the earth's magnetic field

ii. reading heads for magnetic tapes/disks

iii. magnetic apparatus control

In indirect applications, the magnetic field is used as an intermediary carrier for detecting nonmagnetic signals. These applications include [1,2]

i. contactless switching

ii. linear and angular displacement detection

iii. wattmeters

iv. biomagnetometry

These groups each have their own sensor requirements since the variation of field strengths from case to case is large. Hence, this broad range cannot be covered by only one type of sensor. The sensitivity of the devices considered in this thesis, is sufficient for the indirect applications (i), (ii) and (iii). In these applications the magnetic induction is in the range of 5-100 mtesla.

There are semiconductor magnetic sensors based on Si, GaAs or InSb technologies. Silicon offers the advantage of cheap mass manufacturing by integrating a basic sensor element with support and processing circuitry in bipolar or CMOS technology. The companies involved in the research and development of MFS include IBM, Philips, Honeywell, Landis & Gyr, Toyota. Sensors developed outside main-stream IC technologies face extra cost and tools as well as reliability and test procedures [1]. The disadvantages in using Si MFS are its temperature limitations, e.g. 150 °C is usually the quoted limit for Si device operations. Si is not an outstanding

magnetosensitive material as its mobility values are inferior to that of GaAs and InSb. Toshiba (Japan) and Siemens (Europe) produce MFS based on GaAs technology. GaAs MFS are useful at temperatures beyond 150°C and GaAs has a mobility which is 5 times higher than that of Si. Research in magnetic field sensors based on InSb thin films or crystal is strongly pursued in Japan by Electrotechnical Laboratory (ETL) and Hitachi. InSb has an extremely high mobility (50-60 times higher than that of Si) but has a drawback of a small band gap (0.25 eV).

The modeling of semiconductor MFS reported in this thesis is based on Si but sensors of other materials like GaAs or InSb can easily be modeled by suitably changing the appropriate material parameters, such as μ, μ^*, ϵ etc..

In the absence of a magnetic field, analytical and numerical modeling of semiconductor devices is a well established art [3-5]. Many devices are generally modeled by the numerical solution, in two dimensions, of the well known three coupled nonlinear elliptic partial differential equations comprising the continuity equations and the Poisson's equation [3-5].

But numerical modeling of magnetic-field-sensitive silicon microtransducers has not kept up with the pace of the rapid research and development of such sensors (see, e.g. [6-12] and references therein). These sensors include bipolar and lateral magnetotransistors, split-drain MOSFET's and CMOS magnetodiodes. The analysis of these devices explained in terms of simple analytical models (such as Lorentz deflection, Hall voltage, emitter efficiency modulation and magnetoconcentration) has led to some dispute [13,14]. The analytical modeling of such devices is not straightforward for the following reasons ;

i. the basic magnetic field effects in a semiconductor are two dimensional, e.g. Hall field, Lorentz deflection and the magnetoconcentration. One or the other of these effects may prevail in different parts of the same device. An analytical superposition of the basic effects is in general not possible. For instance, it is not clear which mechanism prevails generally in magnetotransistors [13,14].

ii. the distributions of carriers and potential in a magnetic-field-sensitive device are governed by the two interconnected mechanisms of the Lorentz deflection and boundary conditions ; for

instance, there is always a strong change in either the carrier concentrations or the electric potential near the open boundaries of such a device. Only if both magnetoconcentration and space charge effects are negligible, will conformal mapping techniques [15] yield a feasible method for description of such a device.

For these reasons, numerical modeling of magnetic field sensors is a highly desirable tool towards a better theoretical understanding of the electronic mechanisms underlying the operation of these devices. The modeling of magnetic-field-sensitive semiconductor devices is made particularly difficult by the fact that the magnetic field breaks some of the symmetries exploited in the modeling of zero field semiconductor devices. This may be the reason why the numerical analysis of semiconductor devices, in the presence of a magnetic field, was done only recently [16,17].

Presented in this thesis are numerical solutions in two dimensions of the system of coupled nonlinear partial differential equations which govern carrier drift, diffusion, electrostatic potential, generation and recombination in semiconductor devices in the presence of a magnetic field and under appropriate physical boundary conditions. The thesis starts with the discussion of the carrier transport equations, in the presence of a magnetic field and the deriving of appropriate relations between $\vec{J}_n$ and $\vec{B}$. Throughout the thesis the magnetic field is considered perpendicular to the device plane. A brief review is given of the basic magnetic effects, such as Hall effect, carrier deflection and magnetoconcentration. Based on each of these effects are devices realised in both bipolar and MOS technology and a few examples of such devices are covered.

Chapter 3 gives the analysis of a homogeneous silicon slab, starting with a review of the basic equations, boundary conditions, and physical models of the carrier mobility and recombination. Then, in the section on numerical method, the discretisation and linearisation of the coupled nonlinear partial differential equations as well as the boundary conditions at the "floating" (open) boundaries are discussed in detail. Here, the discretisation of the continuity equations uses the generalisation of the Scharfetter-Gummel scheme to two dimensions and nonzero magnetic field. The solution technique - SLOR (Successive Line Over Relaxation), an

iterative technique to solve the linear system of equations (after a Newton iterative step) - is described by a flow chart. The results of the slab analysis are covered in appendices D, E and F. Appendices D and E show the influence of the geometrical aspects of uniformly doped silicon slabs on the electric potential and current densities. Appendix F shows the effect of the magnetoconcentration on the electron and hole densities in slabs under intrinsic or "close to" intrinsic conditions, giving rise to space charge effects.

In Chapter 4, a magnetic field sensor based on the split-drain configuration of the MOSFET is analysed for the linear region of operation. The analysis first presents the basic assumptions which reduce the problem (which is originally three dimensional) to two dimensions by integrating the current density over the depth of the channel. This is followed by a description of the basic equations and boundary conditions. The mobility model employed makes use of a decomposition of the electric field into components that are perpendicular and parallel to the current flow. This is to account for the surface scattering to which the carriers in the channel are subjected to. The resulting Laplace's equation, together with the "floating" (open) boundary conditions are then discretised and solved using the SLOR method. An algorithm, briefly describing the procedure, is shown on a flow chart and a program listing of the MOSFET split-drain model is given in Appendix I. Appendix H shows the results of the two dimensional split-drain simulations which include the potential, current density and surface charge distributions in the MOSFET channel for a variety of aspect ratios and drain separations. An optimal device configuration is predicted with its sensitivity studied for different magnetic field strengths, and a suitable circuit that optimises this sensitivity is shown.

The thesis ends with Chapter 5 which presents a summary of this work and outlines the possible areas which require further investigations.

2. CARRIER TRANSPORT IN MAGNETIC SEMICONDUCTORS

When a semiconductor device is placed in a magnetic field, moving charge carriers (electrons and holes) are subject to the Lorentz force. Several phenomena result as a consequence of the Lorentz force, e.g. Hall effect, carrier deflection, magnetoconcentration(MC) and other secondary effects not mentioned in this thesis but which are described in [18]. These effects, or a combination of them, may be exploited in the design of transducers for the detection of static and dynamic magnetic fields [2].

2.1 The Current Density Equations

The presence of a magnetic field explicitly shows up in the transport equations which now become, [18],

$$\vec{J}_n = (q\mu_n n\vec{E} + qD_n\vec{\nabla}n) - \mu_n^* (\vec{J}_n \times \vec{B}) \quad , \tag{2.1}$$

$$\vec{J}_p = (q\mu_p p\vec{E} - qD_p\vec{\nabla}p) + \mu_p^* (\vec{J}_p \times \vec{B}) \quad . \tag{2.2}$$

The second term, the Lorentz force, is dependent on the current density, $\vec{J}_{n,p}$ and the magnetic field, $\vec{B}$. The drift mobilities $\mu_{n,p}$ and the Hall mobilities $\mu^*_{n,p}$ are treated as positive constants.

Consider just the electron current density eqn. (2.1). Let $\vec{A}_n = (q\mu_n n\vec{E} + qD_n \vec{\nabla} n)$ and taking the vector product of $\vec{B}$ with (2.1) we obtain,

$$\vec{B} \times \vec{J}_n = \vec{B} \times \vec{A}_n - \mu_n^* (|\vec{B}|)^2 \vec{J}_n + \mu_n^* (\vec{B} \cdot \vec{J}_n) \vec{B} \quad . \tag{2.3}$$

The dot product of $\vec{B}$ with (2.1) yields

$$\vec{B} \cdot \vec{J}_n = \vec{B} \cdot \vec{A}_n \quad . \tag{2.4}$$

Putting (2.3) and (2.4) into (2.1) and solving for $\vec{J}_n$, we arrive at

$$\vec{J}_n = \frac{1}{1 + (\mu_n^* |\vec{B}|)^2} \left[\vec{A}_n + \mu_n^* (\vec{B} \times \vec{A}_n) + (\mu_n^*)^2 (\vec{B} \cdot \vec{A}_n) \vec{B}\right] \quad (2.5)$$

Eqn. (2.5) is the general expression relating the current density, $\vec{J}_n$ and the magnetic field, $\vec{B}$. We show two cases regarding the direction of the current density, $\vec{J}_n$.

i. When $\vec{J}_n$ is perpendicular to $\vec{B}$, eqn. (2.4) becomes

$$\vec{B} \cdot \vec{J}_n = \vec{B} \cdot \vec{A}_n = 0 \quad (2.6)$$

and substituting (2.6) into (2.5) yields,

$$\vec{J}_n^{\perp} = \frac{1}{1 + (\mu_n^* |\vec{B}|)^2} \left[\vec{A}_n + \mu_n^* (\vec{B} \times \vec{A}_n)\right] . \quad (2.7)$$

ii. When $\vec{J}_n$ is parallel to $\vec{B}$, from eqn. (2.1) we obtain,

$$\vec{J}_n^{\parallel} = \vec{A}_n . \quad (2.8)$$

2.2 Hall Angle

The Hall angle can be defined as the angle between the current density and the resulting gradient of the quasi-Fermi level.

(a) <u>For electrons</u>,

$$\vec{k} \, tg\theta_{Hn} = \frac{\vec{J}_n \times \vec{A}_n}{\vec{J}_n \cdot \vec{A}_n} , \quad (2.9)$$

where $\vec{k}$ is a unit vector indicating the direction of $\vec{J}_n \times \vec{A}_n$, Θ_{Hn} is the Hall angle for electrons, and $\vec{A}_n$ can be expressed as $\vec{A}_n = q\mu_n n \vec{\nabla}\phi_n$. Here, $\vec{\nabla}\phi_n$ denotes the gradient of the quasi-Fermi level for electrons.

From (2.1) we get,

$$\vec{J}_n \times \vec{A}_n = \mu_n^* \left[\vec{J}_n(\vec{B} \cdot \vec{A}_n) - \vec{B}(\vec{J}_n \cdot \vec{A}_n)\right] \quad . \qquad (2.10)$$

If $\vec{J}_n$ is perpendicular to $\vec{B}$, using (2.4), $\vec{B} \cdot \vec{A}_n = 0$. Thus from (2.9) and (2.10), we obtain,

$$\vec{k}\ tg\theta_{Hn} = -\mu_n^* \vec{B} \quad . \qquad (2.11)$$

(b) For holes, with the same definition, if $\vec{J}_p$ is perpendicular to $\vec{B}$, then

$$\vec{k}\ tg\theta_{Hp} = \mu_p^* \vec{B} \quad . \qquad (2.12)$$

2.3 Current Density Components

If $\vec{B}$ is chosen perpendicular to the device plane and parallel to the z-axis, i.e. $\vec{B} = (0,0,B_z)$, the current density components in the device plane can be expressed as the following ;

$$J_{nx} = \frac{1}{1 + (\mu_n^* B_z)^2} \left[(q\mu_n n E_x + qD_n \frac{\partial n}{\partial x}) - \mu_n^* B_z\ (q\mu_n n E_y + qD_n \frac{\partial n}{\partial y})\right] , \qquad (2.13)$$

$$J_{ny} = \frac{1}{1 + (\mu_n^* B_z)^2} \left[(q\mu_n n E_y + qD_n \frac{\partial n}{\partial y}) + \mu_n^* B_z\ (q\mu_n n E_x + qD_n \frac{\partial n}{\partial x})\right] , \qquad (2.14)$$

$$J_{nz} = (q\mu_n n E_z + qD_n \frac{\partial n}{\partial z}) \quad , \qquad (2.15)$$

$$J_{px} = \frac{1}{1 + (\mu_p^* B_z)^2} \left[(q\mu_p p E_x - qD_p \frac{\partial p}{\partial x}) + \mu_p^* B_z\ (q\mu_p p E_y - qD_p \frac{\partial p}{\partial y})\right] , \qquad (2.16)$$

$$J_{py} = \frac{1}{1 + (\mu_p * B_z)^2} \left[(q\mu_p p E_y - qD_p \frac{\partial p}{\partial y}) \right. \tag{2.17}$$

$$\left. - \mu_p * B_z \ (q\mu_p p E_x - qD_p \frac{\partial p}{\partial x}) \right] ,$$

$$J_{pz} = (q\mu_p p E_z - qD_p \frac{\partial p}{\partial z}) \ . \tag{2.18}$$

Eqns. (2.15) and (2.18) are unaffected by the magnetic field as expressed by (2.8). A microscopic treatment of the transport phenomenon in semiconductors under the influence of magnetic fields is given in [2,19].

2.4 Magnetic Field Effects

Consider a slab of semiconductor that is uniformly doped n-type silicon, with metallic contacts at both ends as shown in Fig. 2.1. Current flowing along its length L, in the y-direction, and a magnetic field, $\vec{B}$ applied in the z-direction will result in a Lorentz force in the x-y plane.

2.4.1 Hall effect

If the geometry of the slab shown in Fig. 2.1 was such that $W/L \rightarrow 0$, i.e. $L >> W$, a transverse field develops across the slab (x-direction) to compensate for the Lorentz force. The transverse field gives rise to a Hall voltage [20] set up across the slab.

Based on this effect are devices realised in both bipolar and MOS technology. Gallagher and Corak [21] proposed the use of the channel region of a MOST as a Hall plate with two electrodes arranged along the channel. Theoretical and experimental work has been carried out on this device (see references contained in [2]) and the best sensitivity was achieved with the MOST operated in the saturation region.

Takamiya and Fujikawa [22] proposed incorporating a differential amplifier and a Hall plate in one device : the differential amplification magnetic sensor (DAMS). Large sensitivities were achieved as a result of the amplification of the differential stage; however the nonlinearity became large too. Popovic and Baltes [23] proposed a magnetotransistor in CMOS technology, of which the operation is reminiscent of the SOS magnetodiode [24], but which does not require an $Al_2 O_3$ substrate ; the high recombining interface is replaced by a reverse biased collector junction providing a virtually infinite recombination velocity.

2.4.2 Carrier Deflection

If, on the other hand, the geometry of the slab in Fig. 2.1 was such that, $L/W \rightarrow 0$, i.e. $W >> L$, the transverse field is absent in this case, giving to carrier-deflection. Thus, the current density vector is no longer parallel to the y-axis but rotated by the Hall angle. Note that this situation is in fact complementary to the Hall effect, in which the current density vector is unaffected and the electric field vector is rotated.

Utilising the effect of carrier deflection, Hudson [25] invented the dual collector magnetotransistor and used the difference between the collector currents as a measure of the magnetic flux density. The sensitivity figures achieved using carrier deflection are comparable to or as much as an order of magnitude better than those of Hall plates. Other advantages of devices based on this principle are discussed in [25]. An extensive review of dual and multicollector magnetotransistors, both vertical and lateral structures, as well as carrier domain magnetometers, all based on the bipolar technology is given by [2].

The principle of carrier deflection was also used in MOS transistors and this was carried out by Fry and Hoey [26]. They used the Hall electrodes (discussed previously in the Hall plate model) as a pair of drains additional to or instead of the real drain. Carr and Hong [27] put foward a theoretical treatment of the carrier deflection mechanism in the dual and triple-drain MOSFET's. Popovic and Baltes presented a CMOS MFS [10] which consists of a pair of split-drain MOS transistors in a CMOS differential amplifier-like configuration. This

configuration is reported to have a sensitivity that is appreciably higher than known MOS Hall elements.

2.4.3 Magnetoconcentration

When electrons and holes are simultaneously injected from opposite sides of an intrinsic or "close-to" intrinsic semiconductor slab, the Lorentz force deflects both electrons and holes to the same surface. Since a Hall voltage is prevented from building up (a consequence of electrical neutrality), the Lorentz force is compensated by a carrier concentration gradient perpendicular to the magnetic and electric field vectors. The conductivity of the slab can be changed considerably by allowing recombination of the carriers at the surface which was enhanced (or depleted) of carriers.

Pfleiderer [18] presented theoretical and experimental analysis of the magnetodiode which is a device based on this effect. Kamarinos *et al.* [24] proposed a silicon-on-sapphire (SOS) magnetodiode which employs a $Si\text{-}SiO_2$ interface on top for obtaining a low recombination velocity (s_1) and a $Si\text{-}Al_2O_3$ interface at the bottom for a high recombination velocity (s_2). Crucial requirements to achieve a high sensitivity are : a large surface recombination velocity difference ($s_1 - s_2$) and a diode thickness that is much smaller than the ambipolar diffusion length.

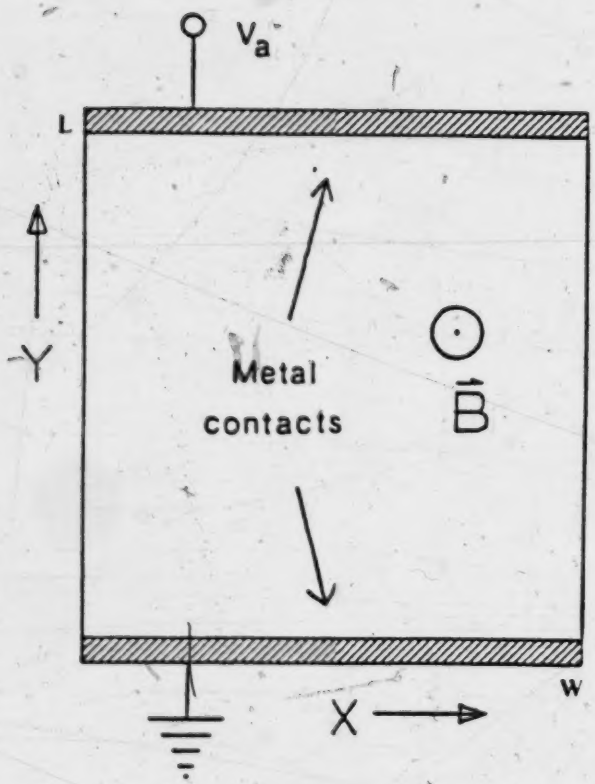

Fig. 2.1 Geometrical representation of a semiconductor slab of length L, width W, and $\vec{B}$ is perpendicular to the device plane

3. ANALYSIS OF A SEMICONDUCTOR SLAB

Consider a uniformly doped rectangular silicon slab with metallic contacts at two edges as shown in Fig. 3.1. Current flowing through the slab in the y-direction and a magnetic field, $\vec{B} = (0,0,B_z)$ applied perpendicular to the slab surface will result in a Lorentz force in the x-y plane. The thickness, h of the slab is chosen large enough, hence any surface effects at z = 0 and z = h can be neglected. Furthermore, by using the assumption that the electrostatic potential ψ, the concentrations n and p, the mobilities μ_n, μ_n^*, μ_p, μ_p^* are all independent of z, we can reduce our problem (which is three dimensional) to that of two dimensions.

3.1 Basic Equations

Similar to the case of zero magnetic field, $J_{nz} = J_{pz} = 0$. Using $\vec{E} = -\vec{\nabla}\psi$ and Einstein's relations, $D = \mu\, kT/q$, eqns. (2.13)-(2.18) are now simplified to two dimensional current density equations, viz.

$$J_{nx}(x, y) = \frac{\mu_n}{1 + (\mu_n^* B_z)^2} \left\{ -\frac{\partial\psi}{\partial x}(x, y) + \frac{kT}{q}\frac{\partial}{\partial x} - \mu_n^* B_z \left[-\frac{\partial\psi}{\partial y}(x, y) + \frac{kT}{q}\frac{\partial}{\partial y} \right] qn(x, y) \right\}, \tag{3.1}$$

$$J_{ny}(x, y) = \frac{\mu_n}{1 + (\mu_n^* B_z)^2} \left\{ -\frac{\partial\psi}{\partial y}(x, y) + \frac{kT}{q}\frac{\partial}{\partial y} + \mu_n^* B_z \left[-\frac{\partial\psi}{\partial x}(x, y) + \frac{kT}{q}\frac{\partial}{\partial x} \right] qn(x, y) \right\}, \tag{3.2}$$

$$J_{px}(x, y) = \frac{-\mu_p}{1 + (\mu_p^* B_z)^2} \left\{ \frac{\partial\psi}{\partial x}(x, y) + \frac{kT}{q}\frac{\partial}{\partial x} + \mu_p^* B_z \left[\frac{\partial\psi}{\partial y}(x, y) + \frac{kT}{q}\frac{\partial}{\partial y} \right] qp(x, y) \right\}, \tag{3.3}$$

$$J_{py}(x, y) = \frac{-\mu_p}{1 + (\mu_p * B_z)^2} \left\{ \frac{\partial \psi}{\partial y}(x, y) + \frac{kT}{q} \frac{\partial}{\partial y} \right.$$

$$\left. - \mu_p * B_z \left[\frac{\partial \psi}{\partial x}(x, y) + \frac{kT}{q} \frac{\partial}{\partial x} \right] qp(x, y) \right\} . \qquad (3.4)$$

The current continuity equations (for the time stationary case) and Poisson's equation remain the same as for zero magnetic field and are given by [4,5].

$$\frac{1}{q} \vec{\nabla} \cdot \vec{J}_n = R \quad , \qquad (3.5)$$

$$- \frac{1}{q} \vec{\nabla} \cdot \vec{J}_p = R \quad , \qquad (3.6)$$

$$\nabla^2 \psi = - \frac{q}{\varepsilon} (p - n + N) \quad . \qquad (3.7)$$

Here, R denotes the net recombination rate and N the net doping density, $N_D - N_A$. The form of eqns. (3.1)-(3.4) are suitable for the choice of the unknown variables p,n and ψ and will be considered as the fundamental set of unknown variables throughout the thesis.

In some cases different choices of variables such as ϕ_n, ϕ_p and ψ are used [4,28] in which case the equations (3.1)-(3.4), (3.7) must be suitably modified [4,28]. The quasi-Fermi potentials are defined by [4,28],

$$n = n_i \exp \left[\frac{q}{kT} (\psi - \phi_n) \right] \quad , \qquad (3.8)$$

$$p = n_i \exp \left[\frac{q}{kT} (\phi_p - \psi) \right] \quad . \qquad (3.9)$$

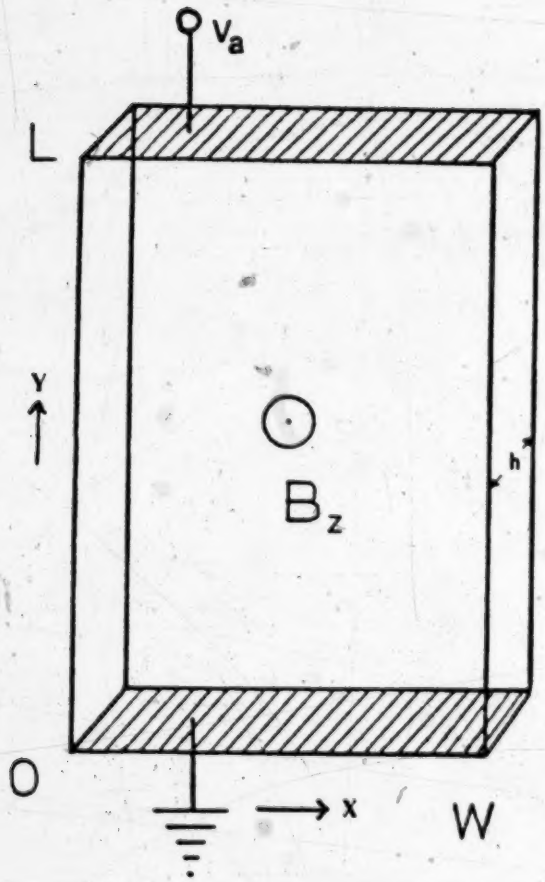

Fig. 3.1 Basic slab geometry : semiconductor slab of length L, width W, and thickness, h. $\vec{B}$ is perpendicular to the drawing plane

3.2 Boundary Conditions

In this section, two types of boundary conditions are considered :

(a) Fixed boundary conditions

With reference to Fig. 3.2, the fixed boundaries are denoted by (1) and (2). Along these "fixed" boundaries the values p, n and ψ are given by infinite contact recombination velocities and charge neutrality [4,5,28]. Hence, carriers are in thermodynamic equilibrium (in terms of quasi-Fermi potentials, $\phi_n = \phi_p = V_a$)

$$p \cdot n = n_i^2 \quad , \tag{3.10}$$

$$p - n + N = 0 \quad . \tag{3.11}$$

Boundary values of ψ are determined from the definition of quasi-Fermi potentials, (3.8) and (3.9) and the space charge neutrality condition (3.11), yielding [4,5,28],

$$\psi = V_a + \frac{kT}{q} \sinh^{-1} \left(\frac{N}{2n_i}\right) \quad . \tag{3.12}$$

(b) Floating boundary conditions

The floating boundaries are denoted by (3) and (4) in Fig. 3.2. At these boundaries, a zero normal component for the electron and hole current densities is assumed (characterising zero surface recombination) [4,5,28] ;

$$J_{nx} = 0 \quad , \tag{3.13}$$

$$J_{px} = 0 \quad . \tag{3.14}$$

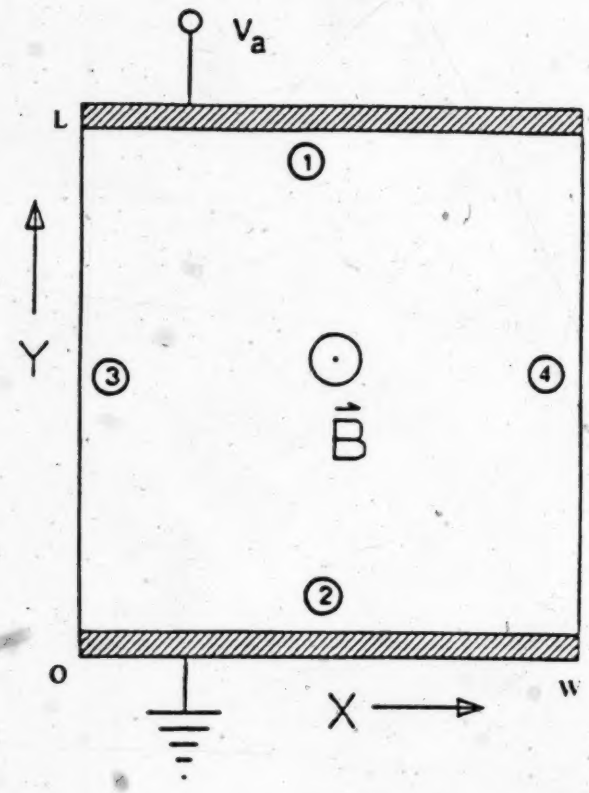

Fig. 3.2 Two dimensional slab geometry

For the required third boundary condition with nonzero magnetic field, one cannot adopt any of the conditions commonly used in the cases of zero magnetic field. A zero normal component of the electric field [4,28] would be inconsistent with the presence of a Hall field. If a zero space charge variation normal to the surface is asssumed [5], the electron and hole concentrations at the boundaries would be too tightly coupled. This leads to the choice of a condition that is somewhat different than the conditions commonly used [4,5] along the floating boundaries ; that is

$$\frac{\partial^2}{\partial x^2} (p - n + N) = 0 \quad . \tag{3.15}$$

However, it still ensures that the space charge is a smooth function of the spatial coordinates. A more advanced analysis will have to take into account surface states [4,29] and possibly the external electric field.

3.3 Models of Physical Parameters

The field equations contain quantities, e.g., net recombination rate R, the mobilities μ_n, μ_p and the Hall mobilities μ_n^*, μ_p^*, which themselves are the results of rather complicated physical mechanisms. These quantities are not constant but could depend on the local values of carrier densities, impurity concentrations and fields.

(a) Carrier mobility

In general, carriers are scattered by phonons and lattice defects and in addition Coulomb scattering at ionized impurity atoms results in a further reduction of the mobility. By fitting experimental data [30], an empirical expression for the drift mobilities is :

$$\mu = \mu_{min} + \frac{\mu_{max} - \mu_{min}}{1 + (N_T/N_{REF})^{\alpha}} \quad . \tag{3.16}$$

Here, $N_T = N_D + N_A$ is the total doping concentration, and the values of the constants are

shown below :

	μ_n	μ_p
$N_{REF}(cm^{-3})$	8.5×10^{16}	6.3×10^{16}
α	0.72	0.76
$\mu_{max}(cm^2/Vs)$	1330	495
$\mu_{min}(cm^2/Vs)$	65	47.7

For the Hall mobility, the approximation

$$\mu^* = r\,\mu \qquad (3.17)$$

is used [19,31] with $r \equiv \langle \tau^2 \rangle / \langle \tau \rangle^2$, where $\langle\ \rangle$ denotes the expectation value. The parameter τ is the mean free time between carrier collisions which depends on the carrier energy. r takes a value of 1.18 for phonon scattering and 1.92 in the case of ionised impurity scattering. In all computations shown in this thesis, a value of 1.92 is adopted for r.

(b) Recombination and generation

The bulk recombination rate, R is assumed to follow the Shockley-Read-Hall (SRH) recombination model [32], viz.

$$R = \frac{p\,n - n_i^2}{\tau_n \left[p + n_i \exp\left(\frac{E_i - E_t}{kT}\right)\right] + \tau_p \left[n + n_i \exp\left(\frac{E_t - E_i}{kT}\right)\right]} \qquad (3.18)$$

Here, τ_n and τ_p are the bulk carrier lifetimes, E_t denotes the energy level of trap centers and E_i the intrinsic Fermi level. Usually E_t is not known and following common practice [4,5], $E_t = E_i$ is assumed in the computations.

3.4 Numerical Method

The partial differential eqns. (3.1)-(3.7), (3.18), and the boundary conditions (3.10)-(3.15) have to be discretised for numerical solutions. In view of the rectangular geometry of the slab, a finite difference technique was implemented on a nonuniform, rectangular grid (see Fig. 3.4). This technique allowed the use of the SLOR (Succesive Line Over Relaxation) method, achieving reasonably fast convergence when the equations, (3.1)-(3.7) were solved simultaneously [5].

Eqns. (3.1)-(3.7) and (3.18) are discretised and then linearised by a Newton iteration scheme [5]. The linear system thus obtained are, however, in many cases unsuitable for iterative solution schemes because of the numerical values of the out-of-diagonal elements. The problem of achieving diagonal dominance can be removed by employing the well known Scharfetter-Gummel scheme [33] but generalized for the case of two dimensions [34,35] and nonzero magnetic field. This generalization is discussed in the following section.

3.4.1 Discretisation

(a) Continuity equations

The analysis of this section is carried out for the electron continuity equation. The same analysis holds for the continuity equation for holes.

Applying Gauss' theorem to eqn. (3.5), we obtain for the stationary case,

$$\int_{V_i} \vec{\nabla} \cdot \vec{J}_n \, dV = \int_{S_i} \vec{J}_n \cdot d\vec{S} = \int_{V_i} qR \, dV \quad . \qquad (3.19)$$

With reference to Fig. 3.3, V_i denotes the volume element of the cell with the central node i. The surface S_i encloses the volume, V_i . The basic assumptions [34,35], of this method are that the current density $\vec{J}_n$, electric field, $\vec{E}$ and the diffusion constant, D_n remain constant inside each of the triangles shown in Fig. 3.3 (e.g. the triangle specified by the central node i and two neighbouring nodes, j=1,2). Then, the surface integral in (3.19) is readily simplified to

$$\int_{S_i} J_n \cdot dS = h \sum_j d_{ij} J_{nij} \quad , \tag{3.20}$$

where J_{nij} is the electron current density component flowing from node i to a neighbouring node j, d_{ij} is the length of the common boundary between node i and node j (see Fig. 3.3) and h denotes the thickness of the slab. To obtain J_{nij} eqn. (2.7) was used in a modified form. Denoting the derivative in the ij-direction by $\partial / \partial S$, the derivative normal to ij (in the counter-clockwise direction) by $\partial / \partial a$ and the component of current normal to J_{nij} as $J^{\perp}_{nij}$, we obtain

$$J_{nij} + \mu_n * B_z J^{\perp}_{nij} = - q \left(\mu_n n \frac{\partial \psi}{\partial S} - \frac{kT}{q} \mu_n \frac{\partial n}{\partial S}\right)$$

$$= kT \mu_n \exp\left(\frac{q\psi}{kT}\right) \frac{\partial}{\partial S} \left[n \exp\left(- \frac{q\psi}{kT}\right)\right] \quad , \tag{3.21}$$

$$J^{\perp}_{nij} - \mu_n * B_z J_{nij} = - q \left(\mu_n n \frac{\partial \psi}{\partial a} - \frac{kT}{q} \mu_n \frac{\partial n}{\partial a}\right)$$

$$= kT \mu_n \exp\left(\frac{q\psi}{kT}\right) \frac{\partial}{\partial a} \left[n \exp\left(- \frac{q\psi}{kT}\right)\right] \quad . \tag{3.22}$$

The derivatives with respect to 'a' are estimated at auxilliary grid points A,B,C,D (see Fig. 3.3) and these pairs of points are denoted by dummy variables (k,ℓ) = (A,B), (B,C), (C,D), (D,A). Keeping in mind our basic assumptions that current densities, electric field and mobilities are constants within each of the triangles shown in Fig. 3.3, (3.21) and (3.22) are integrated over s (between i and j) and over 'a' (between k and ℓ) respectively. Denoting the electron concentrations at i, j, k, ℓ as n_i, n_j, n_k and n_ℓ and the electrostatic potentials at i, j, k, ℓ as ψ_i, ψ_j, ψ_k, ψ_ℓ, we obtain from (3.21) and (3.22),

$$J_{nij} + \mu_n {}^*B_z J^{\perp}_{nij} = \frac{kT}{S_{ij}} \mu_n \left[n_j \frac{\frac{q}{kT}(\psi_j - \psi_i)}{\exp\left[\frac{q}{kT}(\psi_j - \psi_i)\right] - 1} - \frac{n_i \frac{q}{kT}(\psi_i - \psi_j)}{\exp\left[\frac{q}{kT}(\psi_i - \psi_j)\right] - 1} \right] , \quad (3.23)$$

$$J^{\perp}_{nij} - \mu_n {}^*B_z J_{nij} = \frac{kT}{d_{ij}} \mu_n \left[n_\ell \frac{\frac{q}{kT}(\psi_\ell - \psi_k)}{\exp\left[\frac{q}{kT}(\psi_\ell - \psi_k)\right] - 1} - \frac{n_k \frac{q}{kT}(\psi_k - \psi_\ell)}{\exp\left[\frac{q}{kT}(\psi_k - \psi_\ell)\right] - 1} \right] . \quad (3.24)$$

By introducing the "Bernoulli coefficients" [34,35],

$$B_{ij} = \frac{(\psi_i - \psi_j)\, q/kT}{\exp\left[(\psi_i - \psi_j)\, q/kT\right] - 1} \quad (3.25)$$

eqns. (3.23) and (3.24) can be simplified to :

$$J_{nij} + \mu_n {}^*B_z J^{\perp}_{nij} = \frac{kT}{S_{ij}} \mu_n \left[n_j B_{ji} - n_i B_{ij} \right] , \quad (3.26)$$

$$J^{\perp}_{nij} - \mu_n {}^*B_z J_{nij} = \frac{kT}{d_{ij}} \mu_n \left[n_\ell B_{\ell k} - n_k B_{k\ell} \right] . \quad (3.27)$$

Eliminating $J^{\perp}_{nij}$ from (3.26) and (3.27), we obtain for J_{nij}.

$$J_{nij} = \frac{kT\mu_n}{1 + (\mu_n * B_z)^2} \left[\frac{n_j B_{ji} - n_i B_{ij}}{S_{ij}} - \mu_n * B_z \frac{n_\ell B_{\ell k} - n_k B_{k\ell}}{d_{ij}} \right] . \quad (3.28)$$

The net recombination rate (3.19) is assumed to have an average value R_i inside the volume $V_i = A_i \times h$, where A_i denotes the areas of the square ABCD (see Fig. 3.3). Thus eqn. (3.19) becomes,

$$\int_{S_i} J_n \cdot dS = qA_i h R_i \quad . \quad (3.29)$$

Substituting (3.28) into (3.20) and equating the result to (3.29), we obtain,

$$R_i = \frac{1}{1 + (\mu_n * B_z)^2} \mu_n \frac{kT}{q} \frac{1}{A_i} \left[\sum_j \frac{d_{ij}}{S_{ij}} (n_j B_{ji} - n_i B_{ij}) \right.$$

$$\left. - \mu_n * B_z \sum_{k,\ell} (n_\ell B_{\ell k} - n_k B_{k\ell}) \right] . \quad (3.30)$$

Eqn. (3.30) shows the discretised version of the electron continuity eqn. (3.5) in the presence of a magnetic field. Applying the same treatment to (3.6), yields the discretised hole continuity equation in the presence of a magnetic field, viz.

$$R_i = - \frac{1}{1 + (\mu_p * B_z)^2} \frac{kT}{q} \mu_p \frac{1}{A_i} \left[\sum_j \frac{d_{ij}}{S_{ij}} (p_j B_{ij} - p_i B_{ji}) \right.$$

$$\left. - \mu_p * B_z \sum_{k,\ell} (p_\ell B_{k\ell} - p_k B_{\ell k}) \right] . \quad (3.31)$$

The advantage of this discretisation technique is that it handles any type of grid stucture. For the rectangular grid structure, shown in Fig. 3.3, (3.30) and (3.31) are simplified further by linearly interpolating the values of the variables p, n and ψ at the auxilliary grid points A, B, C, D, using the values of these variables at the main grid points. The interpolated values of p, n, ψ and the simplification of the Bernoulli coefficients are shown in Appendix A. With reference to Fig. 3.3, the electron continuity equation is simplified to (see Appendix A) ;

$$R_i = \frac{1}{1 + (\mu_n * B_z)^2} \frac{kT}{q} \mu_n \frac{1}{A_i} \left[n_1 \left\{ \frac{d_{i1}}{S_{i1}} B_{1i} - \mu_n * B_z \frac{q}{4kT} (\psi_4 - \psi_2) \right\} \right.$$

$$+ n_2 \left\{ \frac{d_{i2}}{S_{i2}} B_{2i} - \mu_n * B_z \frac{q}{4kT} (\psi_1 - \psi_3) \right\}$$

$$+ n_3 \left\{ \frac{d_{i3}}{S_{i3}} B_{3i} - \mu_n * B_z \frac{q}{4kT} (\psi_2 - \psi_4) \right\} \qquad (3.32)$$

$$+ n_4 \left\{ \frac{d_{i4}}{S_{i4}} B_{4i} - \mu_n * B_z \frac{q}{4kT} (\psi_3 - \psi_1) \right\}$$

$$\left. - n_i \left\{ \frac{d_{i1}}{S_{i1}} B_{i1} + \frac{d_{i2}}{S_{i2}} B_{i2} + \frac{d_{i3}}{S_{i3}} B_{i3} + \frac{d_{i4}}{S_{i4}} B_{i4} \right\} \right] .$$

The discretised recombination term R_i , from (3.18) reads,

$$R_i = \frac{p_i n_i - n_{ii}^2}{\tau_n \left[p_i + n_{ii} \right] + \tau_p \left[n_i + n_{ii} \right]} \qquad (3.33)$$

In eqns. (3.32) and (3.33), n_1, n_2, n_3, n_4, n_i and ψ_1, ψ_2, ψ_3, ψ_4, ψ_i denote the electron concentration and the potential at the main points (M,N-1), (M+1,N), (M,N+1), (M-1,N) and (M,N) respectively. Note that n_{ii} denotes the intrinsic carrier concentration, n_i at node (M,N). From Fig. 3.3, we note the following ;

$$\begin{aligned}
\frac{d_{i1}}{S_{i1}} &= \frac{h_x(M-1) + h_x(M)}{2h_y(N-1)} \\
\frac{d_{i2}}{S_{i2}} &= \frac{h_y(N-1) + h_y(N)}{2h_x(M)} \\
\frac{d_{i3}}{S_{i3}} &= \frac{h_x(M-1) + h_x(M)}{2h_y(N)} \\
\frac{d_{i4}}{S_{i4}} &= \frac{h_y(N-1) + h_y(N)}{2h_x(M-1)}
\end{aligned} \tag{3.34}$$

Eqn. (3.31) treated in a similar fashion yields the hole continuity equation as ;

$$\begin{aligned}
R_i = -\frac{1}{1 + (\mu_p^* B_z)^2} \frac{kT}{q} \mu_p \frac{1}{A_i} \Bigg[& p_1 \left\{ \frac{d_{i1}}{S_{i1}} B_{i1} + \frac{\mu_p^* B_z q}{4kT} (\psi_4 - \psi_2) \right\} \\
& + p_2 \left\{ \frac{d_{i2}}{S_{i2}} B_{i2} + \frac{\mu_p^* B_z q}{4kT} (\psi_1 - \psi_3) \right\} \\
& + p_3 \left\{ \frac{d_{i3}}{S_{i3}} B_{i3} + \frac{\mu_p^* B_z q}{4kT} (\psi_2 - \psi_4) \right\} \\
& + p_4 \left\{ \frac{d_{i4}}{S_{i4}} B_{i4} + \frac{\mu_p^* B_z q}{4kT} (\psi_3 - \psi_1) \right\} \\
& - p_i \left\{ \frac{d_{i1}}{S_{i1}} B_{1i} + \frac{d_{i2}}{S_{i2}} B_{2i} + \frac{d_{i3}}{S_{i3}} B_{3i} + \frac{d_{i4}}{S_{i4}} B_{4i} \right\} \Bigg] ,
\end{aligned} \tag{3.35}$$

where p_1, p_2, p_3, p_4 and p_i denote the hole concentrations at the main points (M,N-1), (M+1,N), (M,N+1), (M-1,N) and (M,N) respectively. The term, R_i is given by eqn. (3.33).

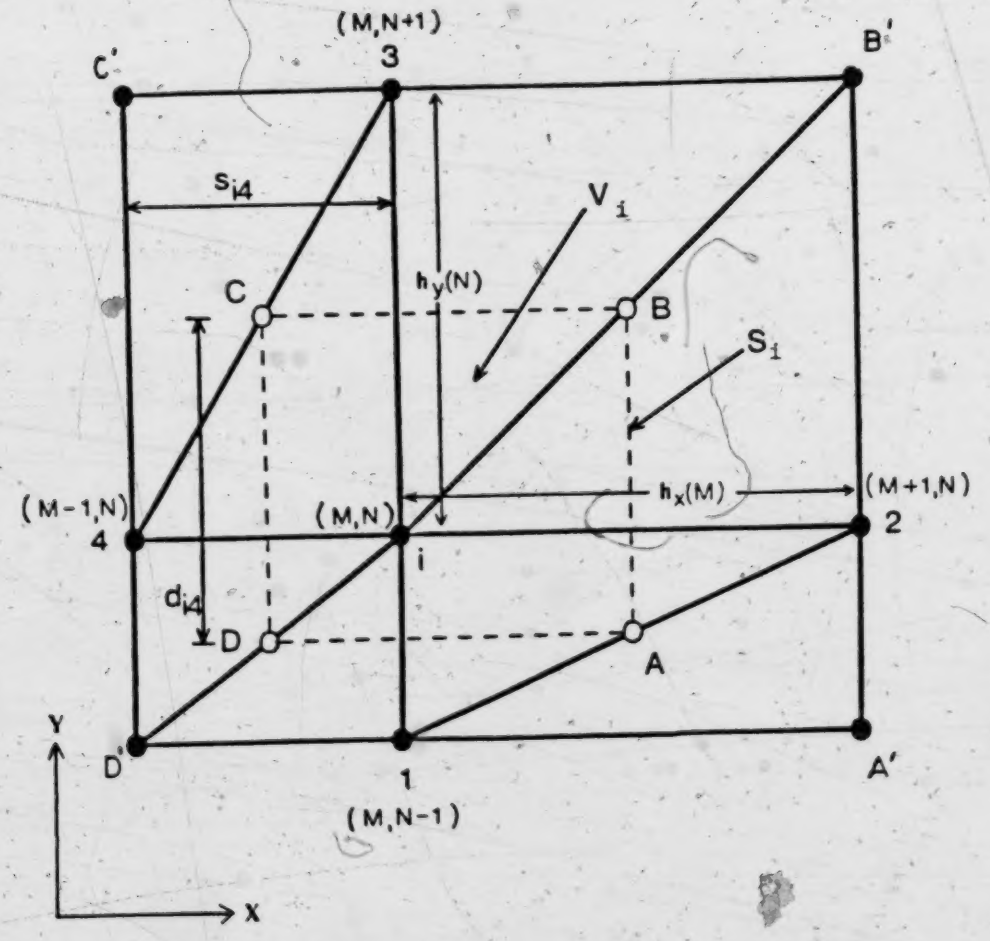

Fig. 3.3 A non-uniform rectangular grid

(b) Poisson's equation

Using a finite difference technique, eqn. (3.7) is discretised by estimating the variables p,n and ψ at the main points (see Fig. 3.3), and we obtain as a direct consequence of eqn. (3.7), the discretised version of Poisson's equation :

$$\frac{2}{h_y(N-1)\,[h_y(N) + h_y(N-1)]}\,\psi_1 + \frac{2}{h_x(M)\,[h_x(M) + h_x(M-1)]}\,\psi_2$$

$$+ \frac{2}{h_y(N)\,[h_y(N) + h_y(N-1)]}\,\psi_3 + \frac{2}{h_x(M)\,[h_x(M) + h_x(M-1)]}\,\psi_4$$

$$- \left[\frac{2}{h_x(M)\;h_x(M-1)} + \frac{2}{h_y(N)\;h_y(N-1)}\right]\psi_i \qquad (3.36)$$

$$+ \frac{q}{\varepsilon_{Si}}\,p_i - \frac{q}{\varepsilon_{Si}}\,n_i = -\frac{q}{\varepsilon_{Si}}\,N_i \;,$$

where N_i denotes the net doping at node (M,N).

(c) Floating boundary conditions

Eqns. (3.13)-(3.15) are discretised on the nonuniform grid shown in Fig. 3.4, for the boundaries (3) and (4) (see Fig. 3.2). At these floating boundaries, the variables p, n and ψ at the meshpoint on the floating line are expressed in terms of the variables at the neighbouring inner points [5]. This is described in the following section :

From eqn. (2.13), the discretised version of (3.13) for boundary (3) (see Fig. 3.2) reads ;

$$n(1,\,N) = n(2,\,N)\,\exp\left\{\frac{q}{kT}\,[\psi(1,\,N) - \psi(2,\,N)] + k_n\right\}, \qquad (3.37)$$

where,

$$k_n = b_n \left\{ \frac{q}{kT} \left[\psi(2, N-1) - \psi(2, N+1)\right] - \ln \frac{n(2, N-1)}{n(2, N+1)} \right\} \quad (3.38)$$

and $$b_n = -\mu_n * B_z h_x(1) / [h_y(N) + h_y(N-1)] \ . \quad (3.39)$$

From eqn. (2.16), the discretised version of (3.14) reads ;

$$p(1, N) = p(2, N) \exp \left\{ \frac{-q}{kT} \left[\psi(1, N) - \psi(2, N)\right] + k_p \right\} \ , \quad (3.40)$$

where,

$$k_p = b_p \left\{ \frac{q}{kT} \left[\psi(2, N+1) - \psi(2, N-1)\right] - \ln \frac{p(2, N-1)}{p(2, N+1)} \right\} \quad (3.41)$$

and

$$b_p = \mu_p * B_z h_x(1) / [h_y(N) + h_y(N-1)] \ . \quad (3.42)$$

The discretised version of (3.15) reads ;

$$p(1, N) - n(1, N) = p(2, N) \left[1 + \frac{h_x(1)}{h_x(2)}\right] - n(2, N) \left[1 + \frac{h_x(1)}{h_x(2)}\right]$$

$$- \frac{h_x(1)}{h_x(2)} p(3, N) + \frac{h_x(1)}{h_x(2)} n(3, N) \quad (3.43)$$

$$- \left[N(1, N) - N(2, N) - \frac{h_x(1)}{h_x(2)} \left\{ N(2, N) - N(3, N) \right\} \right].$$

As eqns. (3.37) and (3.40) are nonlinear in p, n and ψ, we express $p(M,N) = p^0(M,N) + \delta p(M,N)$, $n(M,N) = n^0(M,N) + \delta n(M,N)$, $\psi(M,N) = \psi^0(M,N) + \delta\psi(M,N)$ and apply Taylor's expansion theorem [5] to the nonlinear

functions, neglecting higher order terms. The linearised versions of (3.37) and (3.40) are put into (3.43), hence obtaining the linearised ψ (1,N). We realise that following this procedure, the linearisation is introduced prior to applying the boundary conditions. In general, this may lead to errors due to subtractive cancellation; however, we have verified that the results obtained by Kurata's procedure [5] agree with those obtained by applying the boundary conditions prior to linearisation.

The linearised versions of eqns. (3.37) and (3.40), together with eqn. (3.43) can be summarised in matrix vector notation as

$$\begin{aligned}\theta(1,\ N) = {} & G_T(2,\ N)\ \theta(2,\ N+1) + H_T(2,\ N)\ \theta(2,\ N-1) \\ & + I_T(2,\ N)\ \theta(2,\ N) + J_T(2,\ N)\ \theta(3,\ N) + K(N)\ ,\end{aligned} \tag{3.44}$$

where in general,

$$\theta(X,\ N) = \left[p(X,\ N)\quad n(X,\ N)\quad \psi(X,\ N)\right]^T \tag{3.45}$$

and G_T , H_T , I_T , J_T are 3 x 3 matrices whose elements are given in Appendix B. The constant vector K(N) is a 1 x 3 matrix whose elements are given in Appendix B,

In the same way, we obtain a matrix vector equation for boundary (4) as (see Fig. 3.2)

$$\begin{aligned}\theta(XMAX,\ N) = {} & G_T(XMAX-1,\ N)\ \theta(XMAX-1,\ N+1) \\ & + H_T(XMAX-1,\ N)\ \theta(XMAX-1,\ N-1) \\ & + I_T(XMAX-1,\ N)\ \theta(XMAX-1,\ N) \\ & + J_T(XMAX-1,\ N)\ \theta(XMAX-2,\ N) + L(N)\ .\end{aligned} \tag{3.46}$$

The elements of the matrices, G_T , H_T , I_T , J_T and L for this floating boundary (4) are in Appendix B.

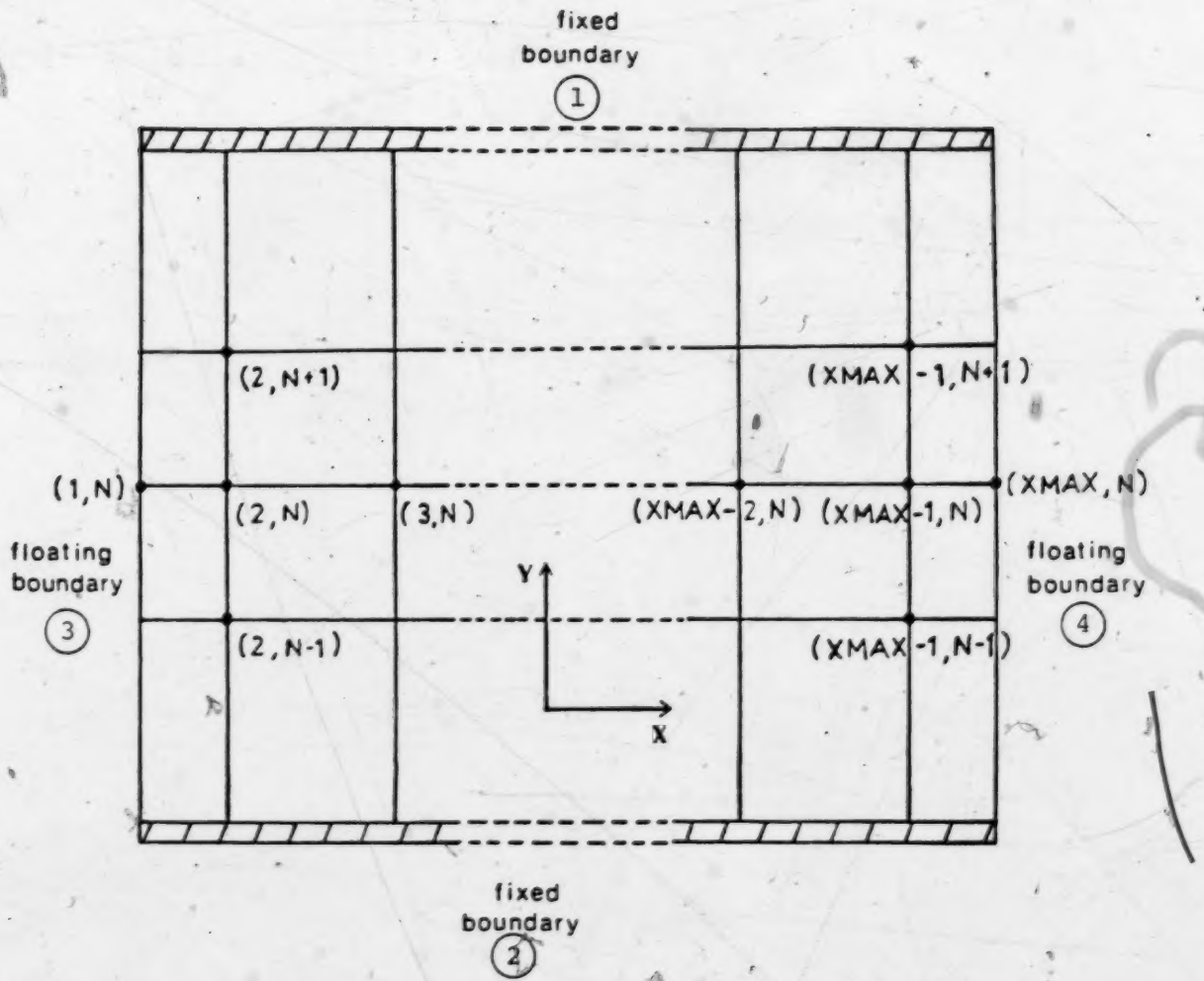

Fig. 3.4 Discretisation of equations (3.13)-(3.15) at the floating boundaries (3) and (4)

3.4.2 Linearisation of the Field Equations

As eqns. (3.5)-(3.7) are nonlinear with respect to the fundamental variables p, n and ψ, Newton's method is used to linearise these equations, leading to the simultaneous solution of p, n and ψ [5]. As in [4,35], the eqns. (3.5)-(3.7) can be written in the form:

$$F_p(p, n, \psi) = \frac{1}{q} \vec{\nabla} \cdot \vec{J}_p + R = 0 \quad , \tag{3.47}$$

$$F_n(p, n, \psi) = -\frac{1}{q} \vec{\nabla} \cdot \vec{J}_n + R = 0 \quad , \tag{3.48}$$

$$F_\psi(p, n, \psi) = \nabla^2 \psi + \frac{q}{\epsilon_{Si}} (p-n+N) = 0 \quad , \tag{3.49}$$

where the RHS of eqns. (3.47)-(3.49) are given by (3.32)-(3.36). We can express p, n and ψ as

$$p = p^0 + \delta p \quad , \qquad n = n^0 + \delta n \quad , \qquad \psi = \psi^0 + \delta \psi \quad ,$$

where, p°, n° and ψ° are trial values (or values from a previous iteration) and δp, δn, $\delta \psi$ represent the 'correction' or 'improvement' on p°, n°, ψ° respectively, through a Newton iteration step. Applying Taylor's expansion theorem to the nonlinear functions, neglecting the higher order terms, we get

$$\begin{bmatrix} \frac{\partial F_p^k}{\partial p} & \frac{\partial F_p^k}{\partial n} & \frac{\partial F_p^k}{\partial \psi} \\ \frac{\partial F_n^k}{\partial p} & \frac{\partial F_n^k}{\partial n} & \frac{\partial F_n^k}{\partial \psi} \\ \frac{\partial F_\psi^k}{\partial p} & \frac{\partial F_\psi^k}{\partial n} & \frac{\partial F_\psi^k}{\partial \psi} \end{bmatrix} \cdot \begin{bmatrix} \delta p^{k+1} \\ \delta n^{k+1} \\ \delta \psi^{k+1} \end{bmatrix} = \begin{bmatrix} -F_p^k \\ -F_n^k \\ -F_\psi^k \end{bmatrix} \tag{3.50}$$

Here,

$$\frac{\partial F^{k}(p,\ n,\ \psi)}{\partial (p,\ n,\ \psi)}$$

is the Jacobian matrix evaluated at $(p,\ n, \psi)^{k}$ and $(\delta p,\ \delta n,\ \delta\psi)^{k+1}$ is the correction at iteration step $(k+1)$, given by

$$\begin{aligned} p^{k+1} &= p^{k} + \delta p^{k+1} \quad , \\ n^{k+1} &= n^{k} + \delta n^{k+1} \quad , \\ \psi^{k+1} &= \psi^{k} + \delta \psi^{k+1} \quad , \end{aligned} \tag{3.51}$$

where $k = 0, 1, 2,..$ and p^{k} , n^{k} , ψ^{k} are the initial guess values. Eqn. (3.50) represents the basic equation for a single node (meshpoint). Taking into account all the five nodes (see Fig. 3.3), where the coefficients and constants carry different values at each of the nodes, we can summarise the two dimensional problem to yield a matrix vector equation that treats p, n and ψ as our unknowns [5] ;

$$\begin{aligned} &A_T(M,\ N)\ \theta(M,\ N-1) + B_T(M,\ N)\ \theta(M,\ N) + C_T(M,\ N)\ \theta(M,\ N+1) \\ &+ D_T(M,\ N)\ \theta(M-1,\ N) + E_T(M,\ N)\ \theta(M+1,\ N) = F_T(M,\ N) \ , \end{aligned} \tag{3.52}$$

where

$$\theta(M,\ N) = \theta^{0}(M,\ N) + \delta\theta(M,\ N) = \begin{bmatrix} p(M,\ N) \\ n(M,\ N) \\ \psi(M,\ N) \end{bmatrix} \ .$$

The definitions of the matrices and vectors ;

$$A_T(M, N) = a_{ij} \quad , \quad B_T(M, N) = b_{ij} \quad , \quad C_T(M, N) = c_{ij} \quad ,$$

$$D_T(M, N) = d_{ij} \quad , \quad E_T(M, N) = e_{ij} \quad , \quad F_T(M, N) = f_i \qquad (3.53)$$

$$i = 1, 3 \quad , \quad j = 1, 3 \quad ,$$

whose elements are related to the coefficients of the continuity and Poisson's equations, are given in Appendix C.

3.4.3 Solution Procedure

Eqn. (3.52) is solved for every meshpoint in our nonuniform grid with the necessary modifications by (3.45) and (3.46) at the floating boundaries. For example, with a grid size of $1 \leq M \leq 50$, $1 \leq N \leq 50$, we have 2500 equations that must be solved simultaneously. Since there are three unknown variables at each meshpoint, the total number of unknown variables for our two dimensional system is 7500. Direct methods such as Gaussian elimination to solve such a system will not be appropriate. This led to the choice of the SLOR (Succesive Line Over Relaxation) method [5,37] to solve the linear system of equations (3.52). The SLOR is an iterative method, one in which the computation must be iterated until an accurate solution for the system of linear equations (3.52) is obtained.

Once the linear system of equations is solved, a single Newton iteration is over. Another Newton step is carried out where the matrix vector coefficients of eqns. (3.52) is updated with the most recent values of the variables. The Newton iterations are continued until the original system of nonlinear equations is solved sufficiently well. The Newton-SLOR method described consists of outer iterations (Newton) and inner iterations (SLOR). Fig. 3.5 illustrates a flow chart description of the method.

A specific feature of the SLOR method is to regard the unknown quantities on two neighbouring points $\Theta(M,N-1)$ and $\Theta(M,N+1)$ as already known quantities [5]. This simplifies eqn. (3.52) to

$$B_T(M, N)\ \theta(M, N) + D_T(M, N)\ \theta(M-1, N) + E_T(M, N)\ \theta(M+1, N)$$

$$= F(M) \quad \text{for} \quad 1 \leq M \leq XMAX-1 \ , \tag{3.54}$$

where,

$$F(M) = F_T(M, N) - A_T(M, N)\ \theta(M, N-1) - C_T(M, N)\ \theta(M, N+1) \ .$$

Eqn. (3.54) is solved with the necessary modification in coefficients [5] according to the boundary conditions (3.44)-(3.46), to fit each individual case.

Using a nonuniform grid of 50 x 50 nodes and working with double precision arithmetic, the computation of one solution required approximately 2Mbytes of memory and 50-200 secs. of CPU time on the Amdahl 580 computer. For every Newton cycle, 15-30 SLOR iterations were implemented. For a relative precision of 10^{-4} typically 8-20 Newton cycles were required. In the SLOR iterations, the relaxation parameter, w (see Fig. 3.5) varied between 0.1 and 1.9 depending on the device parameters and the initial guess values of Θ. Depending on the initial guess, the computations may require up to one third more CPU time than the case of zero magnetic field [38].

To check if the true solution was actually obtained for the given equations, the following tests were made [5] ;

i. both sides of eqn. (3.52) were checked for agreement at desired meshpoints to see if the line equations are really solved through the SLOR method.

ii. the discretised nonlinear eqns. (3.32), (3.35) and (3.36) were checked at desired meshpoints to see if there was agreement between the left and right hand sides.

iii. check for conservation of the terminal currents.

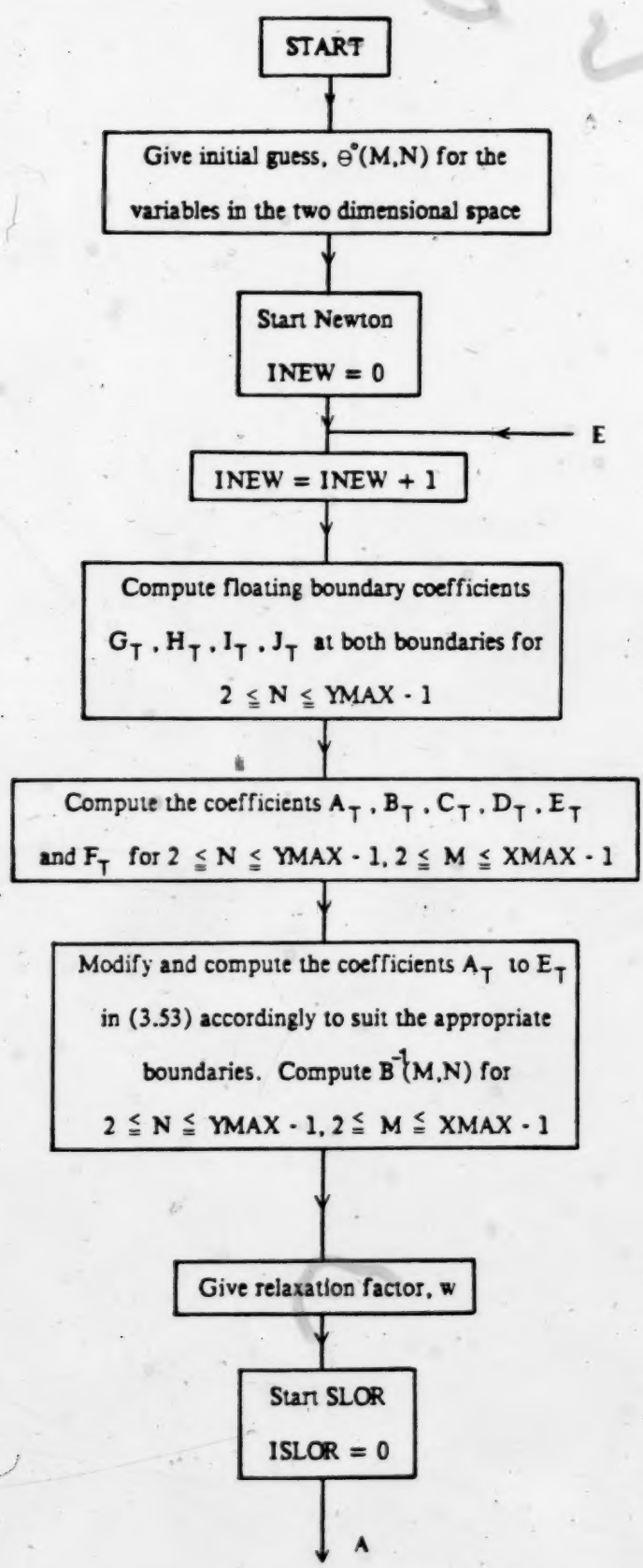
START
Give initial guess, $\theta^{\circ}(M,N)$ for the variables in the two dimensional space
Start Newton
INEW = 0
E
INEW = INEW + 1
Compute floating boundary coefficients G_T , H_T , I_T , J_T at both boundaries for $2 \leq N \leq YMAX - 1$
Compute the coefficients A_T , B_T , C_T , D_T , E_T and F_T for $2 \leq N \leq YMAX - 1$, $2 \leq M \leq XMAX - 1$
Modify and compute the coefficients A_T to E_T in (3.53) accordingly to suit the appropriate boundaries. Compute $B^{-1}(M,N)$ for $2 \leq N \leq YMAX - 1$, $2 \leq M \leq XMAX - 1$
Give relaxation factor, w
Start SLOR
ISLOR = 0
A

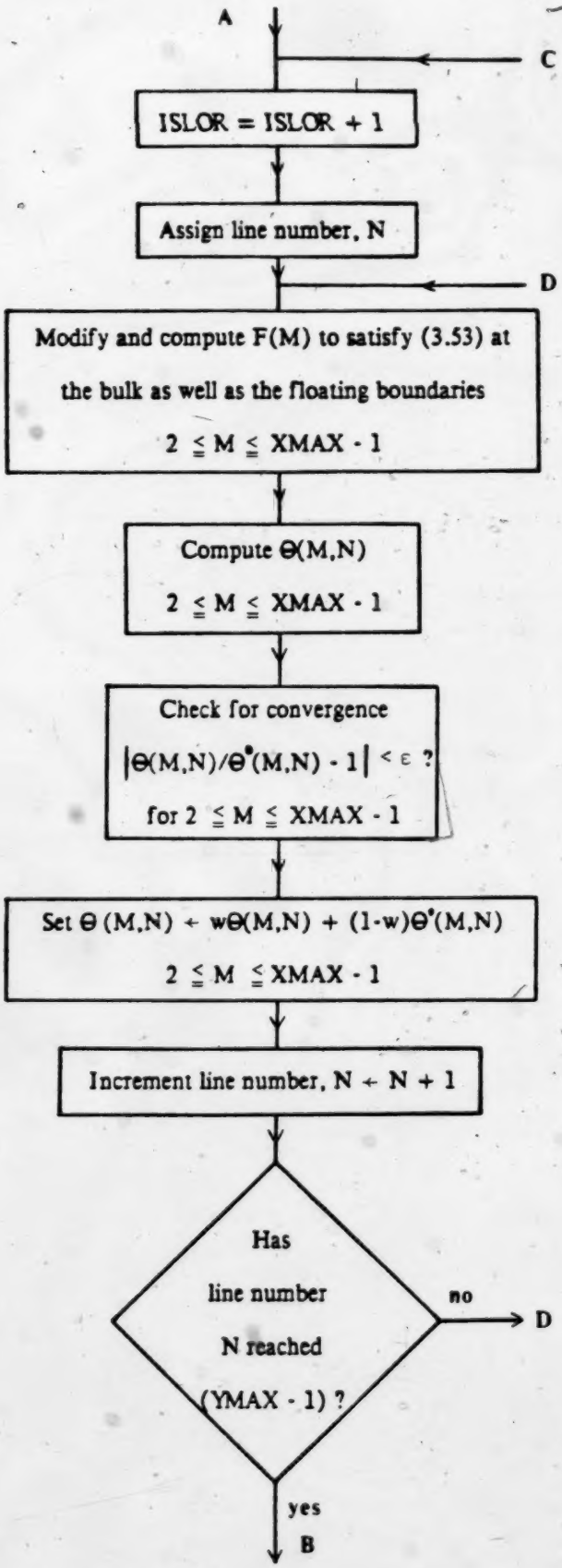
A
C
ISLOR = ISLOR + 1
Assign line number, N
D
Modify and compute F(M) to satisfy (3.53) at the bulk as well as the floating boundaries
2 ≦ M ≦ XMAX - 1
Compute Θ(M,N)
2 ≦ M ≦ XMAX - 1
Check for convergence
|Θ(M,N)/Θ*(M,N) - 1| < ε ?
for 2 ≦ M ≦ XMAX - 1
Set Θ (M,N) ← wΘ(M,N) + (1-w)Θ*(M,N)
2 ≦ M ≦ XMAX - 1
Increment line number, N ← N + 1
Has line number N reached (YMAX - 1) ?
no
D
yes
B

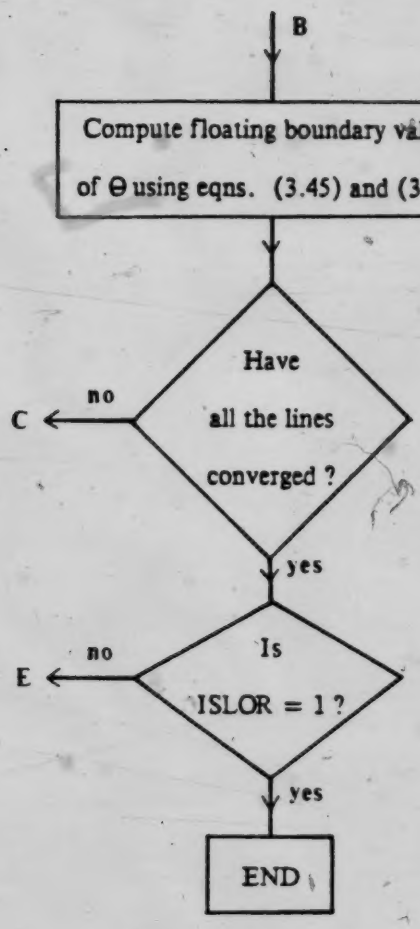

Fig. 3.5 Flow-chart of the Newton-SLOR method

3.5 Results and Discussion

In this section, distributions of interest, such as equipotential lines, current lines and carrier concentrations are shown for uniformly doped rectangular slabs of different slab geometries and for different magnetic field strengths, the magnetic field being perpendicular to the device plane.

The electric potential and current densities were computed for a square silicon slab with metal contacts and with doping levels of 10^{16} cm^{-3} for both p and n-type material [16]. Plots of the equipotential curves and current lines in the slab are shown for magnetic field strengths of $\vec{B}$ = 1 t and 10 t (see Figs. 3.6 - 3.9). Equipotential lines are parallel close to the metal boundary and the current lines are parallel close to the 'floating' (open) boundary. But far from the boundaries, however, the physical mechanisms in the slab cannot be visualised in terms of Lorentz deflection nor Hall voltage ; both these mechanisms are involved in a complex way [16].

The dependence of the electric potential and current density on the device geometry is shown in [17]. Computations were made for various geometries and plots of the equipotential curves and current lines are shown for two cases, W/L = 1/4 and W/L = 4 (see Figs. 3.10 and 3.11). In the case of the long slab (W/L = 1/4), current lines are parallel to the open slab boundaries except for regions close to the metal contacts. There is a constant Hall field, E_x across the width of the slab. In the case of the short slab (with wide contacts, W/L = 4), carrier deflection prevails in most of the device area [17]. There is no presence of the Hall field ($E_x = 0$) and the current lines are skewed by the Hall angle. The variations of the electric field component ratio E_x / E_y and the current density components J_{nx} / J_{ny} across the width of the slab for the geometries discussed is shown in Figs. 3.12 and 3.13. Both these ratios have a maximum value of $\tan \Theta_{Hn} = \mu_n^* B_z$, where $\tan \Theta_{Hn}$ is the Hall angle for electrons.

In our discussion so far, we have only considered doped material, i.e. when the doping level is much greater than the intrinsic concentration. Under such conditions [16,17], the magnetoconcentration effects were insignificant. However, if the doping level is much smaller than the intrinsic concentration [38], the magnetoconcentration dominates the hole and electron

densities as shown in Figs. 3.14 (a) and 3.14 (b). The intrinsic condition is modeled by an assumed elevated temperature of 500 °K using the expression [5] $n_i(T) = 1.22 \times 10^{16} \cdot T^{3/2} \exp(-1.15 / 2kT)$. At 500 °K, the intrinsic concentration is approximately $2.2 \times 10^{14} / cm^3$. Fig. 3.14 (c) shows the combined effects of magnetoconcentration and metal boundaries resulting in concentration gradients in both x and y-directions, yielding an unusual space charge distribution. Under such conditions [38], the equipotential lines show only small gradients (i.e. small Hall field components), while the current lines crowd on the high concentration side of the device indicating a local conductivity change (see Fig. 3.14 (d)).

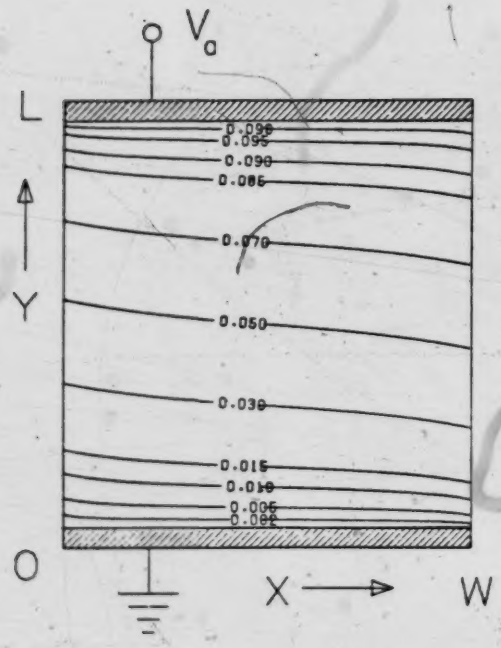

Fig. 3.6 Equipotential curves for n-type Si device, V_a = 0.1 V, L = W = 100 μm and $\vec{B}$ = 1 t

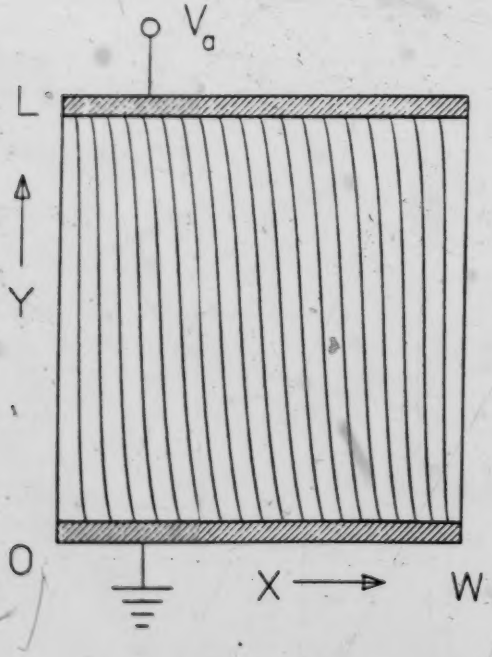

Fig. 3.7 Current lines corresponding to Fig. 3.6

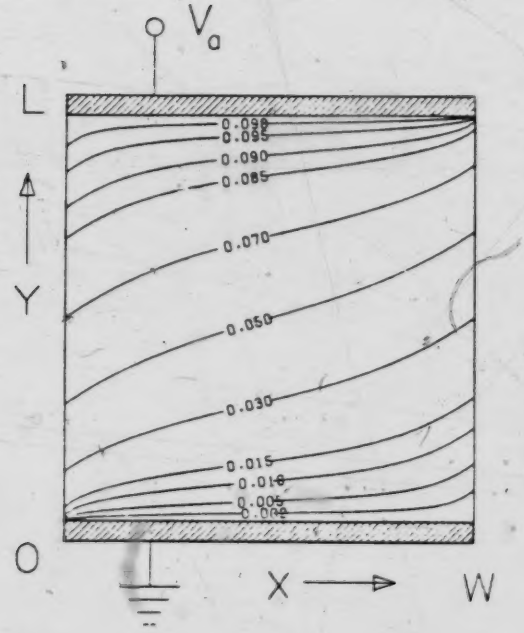

Fig. 3.8 Equipotential curves for p-type Si device, V_a = 0.1 V, L = W = 100 μm and $\vec{B}$ = 10 t

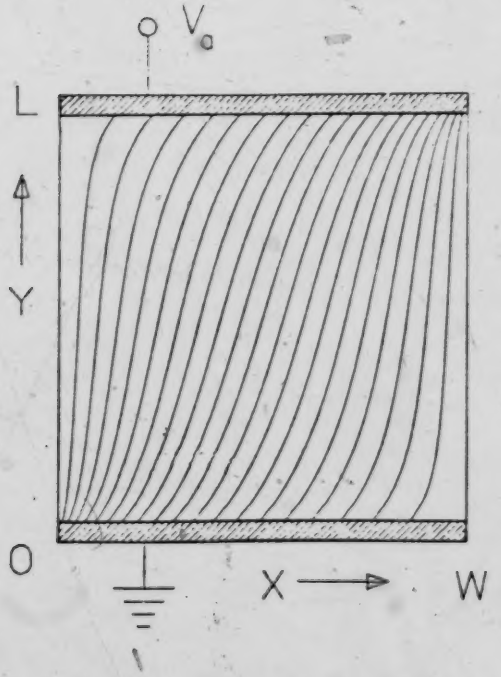

Fig. 3.9 Current lines corresponding to Fig. 3.8

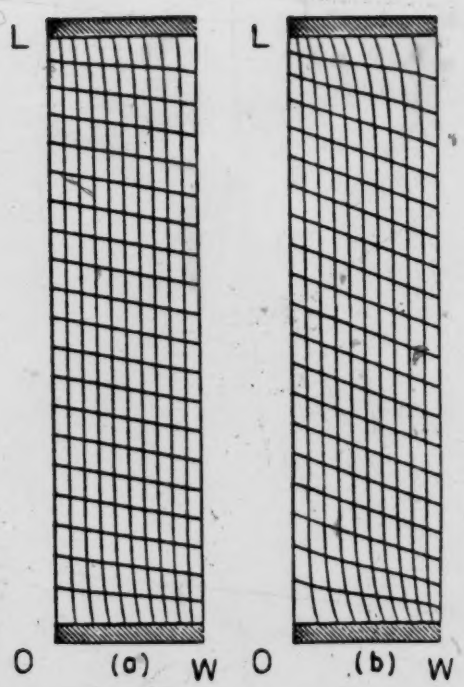

Fig. 3.10 (a) Equipotential and current lines for an n-type Si device, L = 4W, B_z = 1 t, V_a = 1 V

(b) Same as (a) but B_z = 2 t

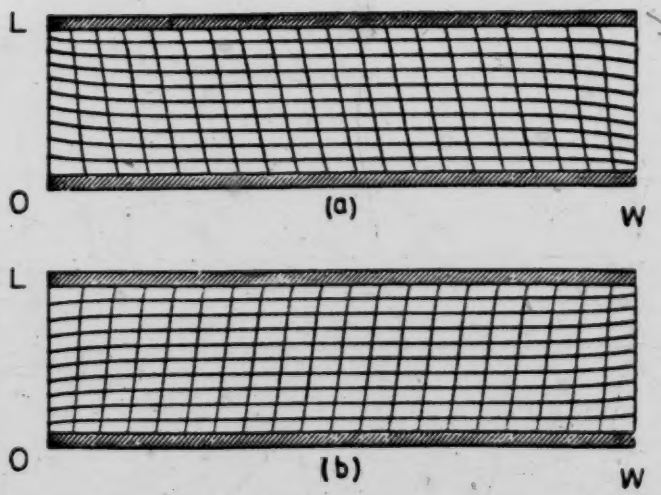

Fig. 3.11 (a) Equipotential and current lines for an n-type Si device, L = W/4, B_z = 1 t

(b) Equipotential and current lines for a p-type Si device, L = W/4, B_z = 2 t

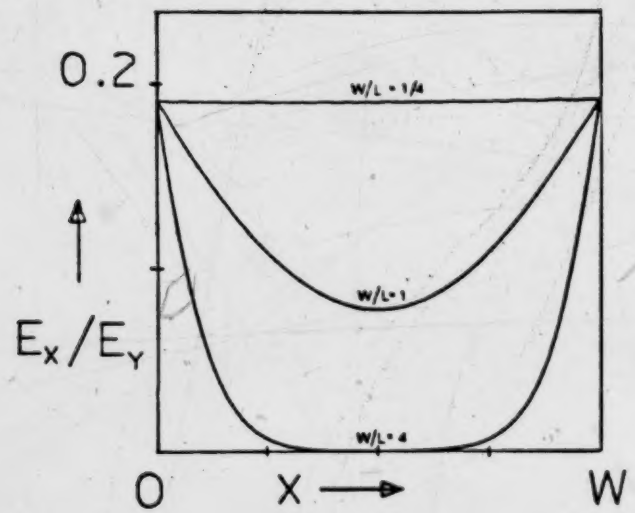

Fig. 3.12 Electric field component ratio E_x/E_y across the middle (y = L/2) of the devices corresponding to Figs. 3.6, 3.10 (a) and 3.11 (a)

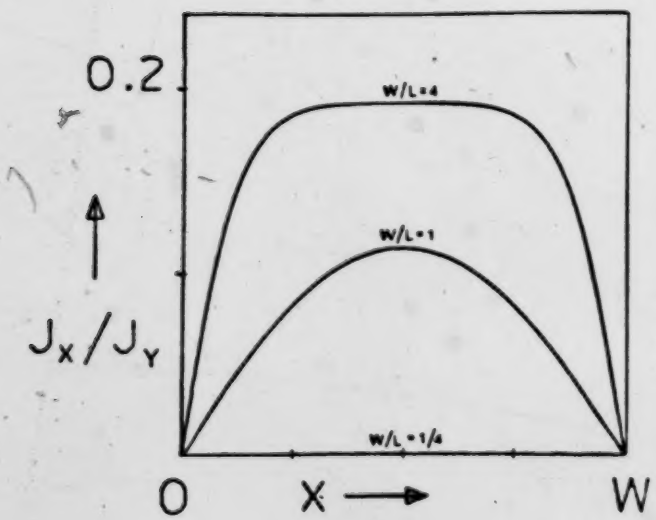

Fig. 3.13 Current deflection J_x/J_y across the middle (y = L/2) of the devices corresponding to Fig. 3.12

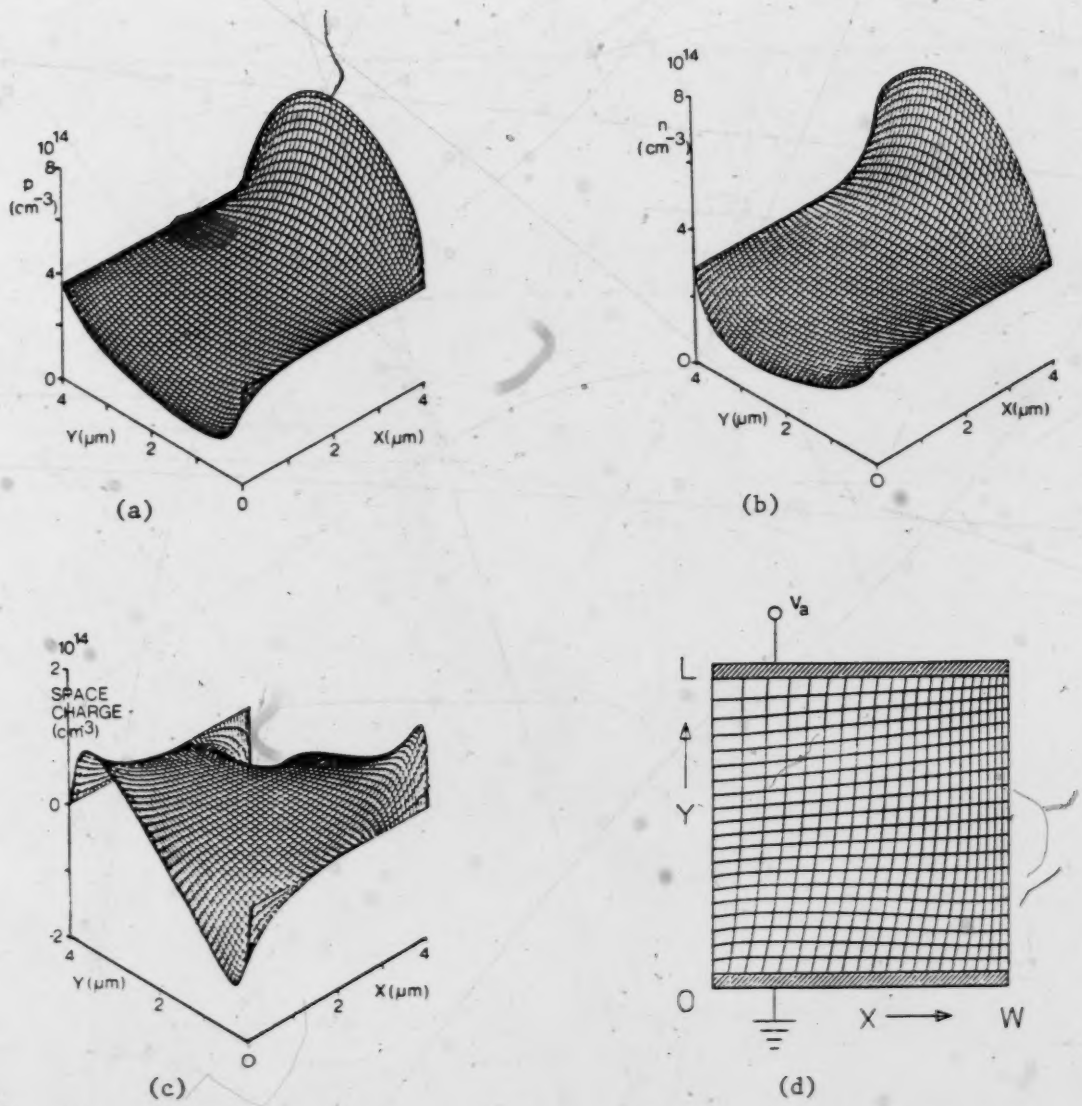

Fig. 3.14 Intrinsic Si square device ;

$L = W = 4\ \mu m$, $V_a = 1$ V, $B_z = 1$ t, $T = 500^{\circ}K$

(a) Hole concentration

(b) Electron concentration

(c) Space charge distribution

(d) Equipotential and current lines

4. ANALYSIS OF THE MOS MAGNETIC FIELD SENSOR

Consider an N-channel MOSFET operated in the linear region as shown in Fig. 4.1. The magnetic field, $\vec{B}$ is assumed to be perpendicular to the channel, i.e. $\vec{B} = (0,0,B_z)$; thus the Lorentz force acts in the plane of the channel (x-y plane). As in the case of zero magnetic field, we assume no current flow in the z-direction.

4.1 Assumptions

In the following, the assumptions made in the analysis of the MOSFET are discussed [4,31] :

(a) the gate structure corresponds to an ideal MOS diode so that any interface traps, fixed oxide charges or work function differences can be neglected. In a nonideal gate, the effect of fixed charges and difference in work functions cause a voltage shift corresponding to the flatband voltage, V_{FB} . This in turn causes a change in the threshold voltage, V_T .

(b) the doping in the channel is uniform.

(c) the drift and Hall mobilities in the inversion layer are constants for given gate and drain bias voltages. This is done so by neglecting $\frac{\partial \mu_n}{\partial z}$, $\frac{\partial \mu^*_n}{\partial z}$ across the channel and assuming no lateral dependence of μ_n , μ^*_n (for MOSFET's operating in the linear region under low gate bias voltages, $E_z(x,y)$ can be assumed to be constant).

(d) the reverse leakage current is negligibly small.

(e) the transverse field, $E_z >> E_y$, the longitudinal field in the channel, corresponding to the so-called Gradual Channel Approximation. This means that the charges in the system are governed by the vertical field only.

(f) within the inversion layer, the hole current density can be neglected since $\vec{J}_p << \vec{J}_n$ for $V_D \geq 0$ and $V_B \leq 0$. The net recombination rate can be assumed zero in the channel. This yields the drain current, I_D to be an electron current of vanishing divergence.

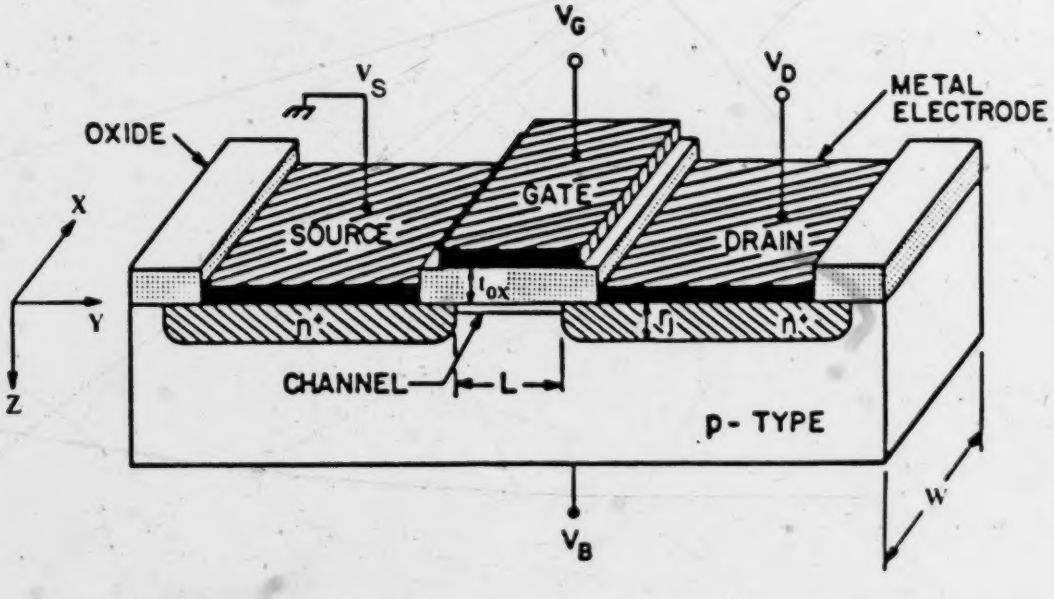

Fig. 4.1 Schematic of an N-channel MOSFET

4.2 Basic Equations

Following these assumptions and considering only drift currents, the charge in the inversion layer is given by [31]

$$Q_n(x, y) = C_{ox} \cdot [V(x, y) + 2\psi_B - V_G] + \sqrt{2\varepsilon_{Si} q N_A \cdot [V(x, y) + 2\psi_B]} \quad . \tag{4.1}$$

Here, V (x,y) denotes the reverse bias voltage between a point (x,y) in the channel and the source electrode (which is assumed grounded). C_{ox} is the gate oxide capacitance per unit area ;

$$C_{ox} = \varepsilon_{SiO_2}/t_{ox} \quad , \tag{4.2}$$

where t_{ox} is the oxide thickness. ψ_B is the potential difference between the bulk Fermi level (E_{Fp}) and the intrinsic Fermi level (E_i). ψ_B is given by

$$\psi_B = \frac{kT}{q} \log_e \left(\frac{N_A}{n_i}\right) \quad , \tag{4.3}$$

where kT/q = 25.7 mV at room temperature, N_A the bulk doping density and n_i the intrinsic concentration. As an approximation, the surface potential ψ_S at inversion can be expressed as [31]

$$\psi_S(x, y) = 2\psi_B + V(x, y) \quad . \tag{4.4}$$

In the following, we discuss a two dimensional approximation to the exact solution which is obtained by integrating the electron current density (3.1) and (3.2) over the channel depth, t. This was carried out using the assumptions discussed previously (in particular assumption (c)) and further neglecting the dependence of $\frac{\partial V}{\partial x}, \frac{\partial V}{\partial y}$ on z. The integration yields two dimensional line current densities (current per unit length) and they read ;

$$\hat{J}_{nx}(x, y) = \frac{-1}{1 + (\mu_n * B_z)^2} \left[\mu_n \frac{\partial V}{\partial x} + \mu_n * B_z \left(\mu_n \frac{\partial V}{\partial y} \right) \right] Q_n(x, y), \quad (4.5)$$

$$\hat{J}_{ny}(x, y) = \frac{-1}{1 + (\mu_n * B_z)^2} \left[\mu_n \frac{\partial V}{\partial y} - \mu_n * B_z \left(\mu_n \frac{\partial V}{\partial x} \right) \right] Q_n(x, y). \quad (4.6)$$

Here,

$$\hat{J}_{nx}(x, y) = \int_0^t J_{nx}(x, y, z)\, dz \quad , \quad (4.7)$$

$$\hat{J}_{ny}(x, y) = \int_0^t J_{ny}(x, y, z)\, dz \quad , \quad (4.8)$$

$$Q_n(x, y) = q \int_0^t n\,(x, y, z)\, dz \quad . \quad (4.9)$$

The integration is carried out from the semiconductor-oxide interface ($z = 0$) to the point ($z = t$) at which E_i intersects E_{Fn} (the quasi-Fermi level for electrons).

Integrating (4.1) from the source (0 V) to a potential V, at any arbitrary point (x,y) in the channel [39], viz.

$$\int_0^V Q_n(V')\, dV' = \hat{Q}_n(V) \quad , \quad (4.10)$$

where V' is a dummy variable. From (4.10) we note the following :

$$\frac{\partial V}{\partial x} Q_n(V) = \frac{\partial \hat{Q}_n(V)}{\partial x} \quad , \quad (4.11)$$

$$\frac{\partial V}{\partial y} Q_n(V) = \frac{\partial \hat{Q}_n(V)}{\partial y} \quad . \quad (4.12)$$

Substituting (4.11) and (4.12) into (4.5) and (4.6) and introducing a new function

$$u = \frac{kT}{q} Q_n(V) - \mathcal{Q}_n(V) \tag{4.13}$$

we can simplify (4.5), (4.6) as follows :

$$\hat{J}_{nx}(x, y) = \frac{\mu_n}{1 + (\mu_n * B_z)^2} \left[\frac{\partial u}{\partial x} - \mu_n * B_z \frac{\partial u}{\partial y}\right] , \tag{4.14}$$

$$\hat{J}_{ny}(x, y) = \frac{\mu_n}{1 + (\mu_n * B_z)^2} \left[\frac{\partial u}{\partial y} + \mu_n * B_z \frac{\partial u}{\partial x}\right] . \tag{4.15}$$

The electron continuity eqn. (3.5), using assumption (f) becomes

$$\frac{\partial}{\partial x} \hat{J}_{nx}(x, y) + \frac{\partial}{\partial y} \hat{J}_{ny}(x, y) = 0 . \tag{4.16}$$

Hence from (4.14), (4.15) and (4.16) we arrive at

$$\frac{\partial^2 u}{\partial x^2} + \frac{\partial^2 u}{\partial y^2} = 0 . \tag{4.17}$$

Note that to arrive at (4.17), we assumed that diffusion current is negligible along the channel. u can be determined from (4.1), (4.10) and (4.13) to read

$$u = \frac{kT}{q} (2\psi_B - V_G) C_{ox} + C_{ox} (\frac{kT}{q} - 2\psi_B + V_G) V$$

$$- \frac{C_{ox}}{2} V^2 + \frac{kT}{q} (2\epsilon_{Si} N_A q V + 4\epsilon_{Si} N_A q \psi_B)^{1/2} \tag{4.18}$$

$$- \frac{1}{3\epsilon_{Si} N_A q} (2\epsilon_{Si} N_A q V + 4\epsilon_{Si} N_A q \psi_B)^{3/2} .$$

4.3 Boundary Conditions

Eqn. (4.17), $\Delta u = 0$ requires boundary conditions in order to completely specify the boundary value problem to be solved. With reference to Fig. 4.2 the boundary conditions are the following :

(a) Ohmic contacts

At these contacts (drain and source electrodes) infinite contact recombination velocity (3.10) and space charge neutrality (3.11) are assumed, hence carriers are in thermodynamic equilibrium. At the drains, eqn. (4.18) yields :

$$u_{D1} = u\Big|_{V = V_{D1}} , \tag{4.19}$$

$$u_{D2} = u\Big|_{V = V_{D2}} . \tag{4.20}$$

At the source (which is grounded), using (4.18) we obtain ;

$$u_S = u\Big|_{V = V_S = 0\ V} . \tag{4.21}$$

(b) Floating boundaries

At these boundaries (denoted by (1), (2) and (3) in Fig. 4.2) the normal component of electron current density is assumed to be zero, yielding

$$\vec{n} \cdot \vec{J}_n = 0 . \tag{4.22}$$

For the region between the drains, i.e. the floating boundary denoted by (3) in Fig. 4.2, we apply condition (4.22), $\hat{J}_{ny} = 0$, which from (4.15) yields

$$\frac{\partial u}{\partial y} = -\mu_n^* B_z \frac{\partial u}{\partial x} \quad . \tag{4.23}$$

Along the remaining floating boundaries (1) and (2) shown in Fig. 4.2, we maintain the condition (4.22), $\hat{J}_{nx} = 0$, which from (4.14) yields

$$\frac{\partial u}{\partial x} = \mu_n^* B_z \frac{\partial u}{\partial y} \quad . \tag{4.24}$$

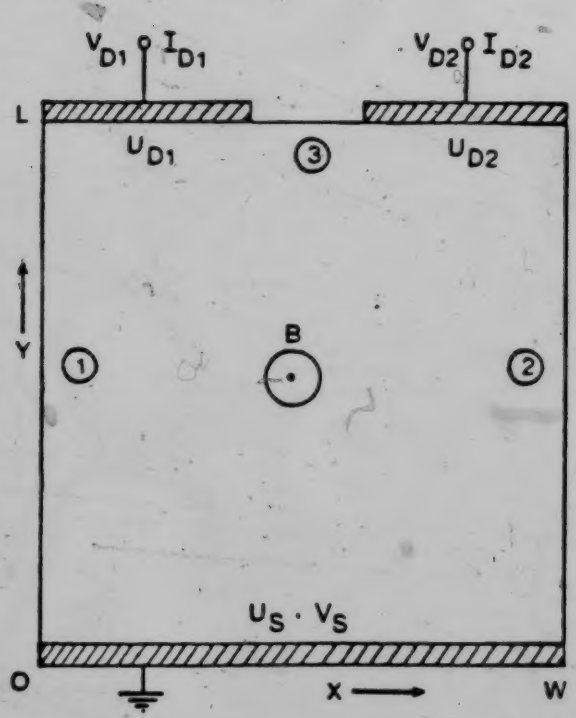

Fig. 4.2 MOSFET channel geometry for a split-drain configuration

4.4 Carrier Mobility

Apart from the usual scattering mechanisms, mentioned in the previous chapter, carriers in the channel of MOSFET devices are further subject to surface scattering or surface roughness which strongly degrades the mobility even further. Following [40] this effect is taken into account by assuming the mobility to be a product of two functions, each of which includes a field component perpendicular or parallel to the current flow [40], viz.

$$\mu_n(N_A, E_y, E_z) = \mu_0 \, f(N_A, E_y) \, g(E_z) \quad . \qquad (4.25)$$

Here, E_z is the field component perpendicular to the current flow and E_y is the component of field parallel to the current flow. μ_o denotes the low field mobility of electrons in intrinsic Si and a value of 1500 cm^2 / Vs is assumed [31].

The function $f(N_A, E_y)$ represents the property of bulk mobility in Si and is approximately given by [33].

$$f(N_A, E_y) = \left[1 + \frac{N_A}{N_A/S + N} + \frac{(E_y/A)^2}{E_y/A + F} + \left(\frac{E_y}{B}\right)^2 \right]^{-1/2} \quad . \qquad (4.26)$$

Here, S, N, A, F and B are constants whose values are given below.

S	N	A	F	B
350	3×10^{16} / cm^3	3.5×10^3 V / cm	8.8	7.4×10^3 V / cm

N_A is the bulk doping density and a constant E_y field is assumed in the channel, viz.

$$E_y = \left| (V_D - V_S)/L \right| \quad , \qquad (4.27)$$

where L is the channel length.

The function $g(E_z)$ represents the property of surface mobility [40]. Surface mobility decreases with increasing gate field and this property can be approximately expressed as [40]

$$g = (1 + \alpha E_z)^{-1/2} \quad . \qquad (4.28)$$

For an N-channel MOSFET, $\alpha = 1.539 \times 10^{-5}$ cm / V and E_z is averaged over the channel length to obtain

$$E_z = \frac{C_{ox}}{\epsilon_{Si}} (V_G - 2\psi_B - \frac{V_D}{2}) \quad . \qquad (4.29)$$

For the Hall mobility, μ_n^* the approximation (3.17) is used.

4.5 Numerical Method

The partial differential eqn. (4.17), $\Delta u = 0$ and the boundary conditions (4.23) and (4.24) are descretised and numerically solved using the SLOR technique (discussed in the previous chapter). As the geometry of the MOSFET channel is rectangular, the discretisation was based on a finite difference scheme implemented on a nonuniform grid (as shown in Fig. 3.3).

4.5.1 Discretisation

(a) Laplace's Equation

Following the same technique as done in obtaining the discretised Poisson's eqn. (3.36), the discretised $\Delta u = 0$ reads ;

$$\frac{2}{h_y(N-1)\,[h_y(N) + h_y(N-1)]}\; u(M,\ N-1)$$

$$- \left[\frac{2}{h_x(M)\,h_x(M-1)} + \frac{2}{h_y(N) + h_y(N-1)}\right]\; u(M,\ N)$$

$$+ \frac{2}{h_y(N)\,[h_y(N) + h_y(N-1)]}\; u(M,\ N+1) \qquad (4.30)$$

$$+ \frac{2}{h_x(M-1)\,[h_x(M) + h_x(M-1)]}\; u(M-1,\ N)$$

$$+ \frac{2}{h_x(M)\,[h_x(M) + h_x(M-1)]}\; u(M+1,\ N) \;=\; 0 \quad .$$

Eqn. (4.30) yields a vector equation for the two dimensional problem :

$$A_T(M,\ N)\ u(M,\ N-1) + B_T(M,\ N)\ u(M,\ N) + C_T(M,\ N)\ u(M,\ N+1)$$
$$+ D_T(M,\ N)\ u(M-1,\ N) + E_T(M,\ N)\ u(M+1,\ N) = F_T(M,\ N) \qquad (4.31)$$

with definitions of vectors given in Appendix G.

(b) Boundary Conditions

At the fixed boundaries, the value of u is definite so that the relevant terms in eqn. (4.31) are transferred to the right-hand side to be added to the constant term F_T (M,N).

At the floating boundaries, the variable u at a meshpoint on the floating line is expressed by those at the neighbouring inner points [5]. This is described in the following section:

(i) At boundaries (1) and (2), we discretise eqn. (4.24), (see Figs. 4.3 and 4.4) and summarising the results in vector form, as :

$$u(1, N) = G_T(2, N)\, u(2, N+1) + H_T(2, N)\, u(2, N-1) + I_T(2, N)\, u(2, N) + J_T(2, N)\, u(3, N) , \tag{4.32}$$

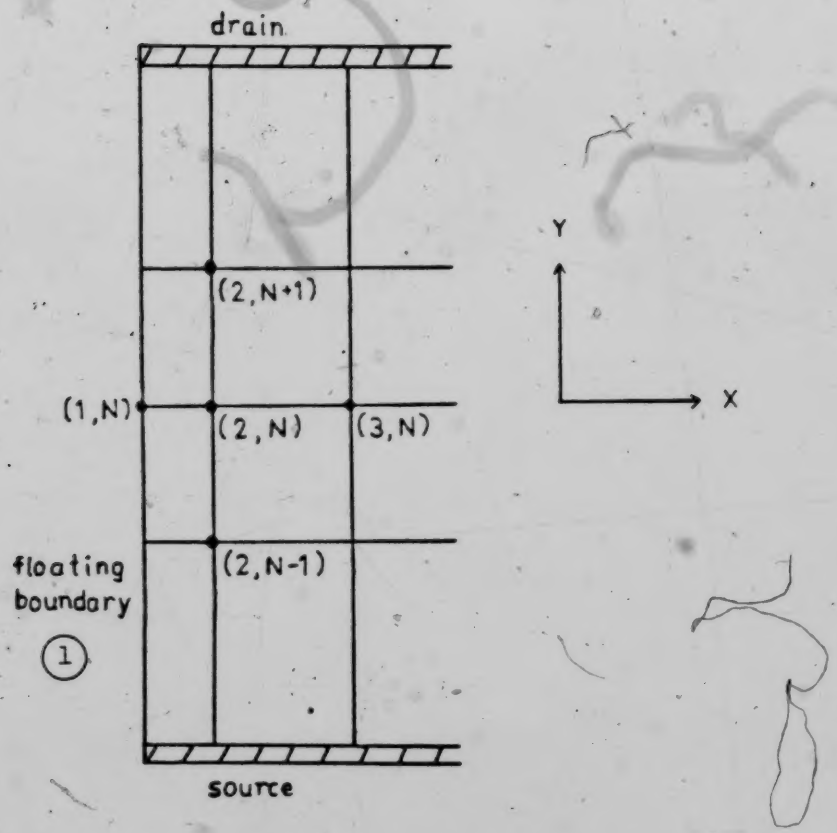

Fig. 4.3 Discretisation of (4.24) at (1)

$$
\begin{aligned}
u(XMAX, N) = {} & G_T(XMAX-1, N)\ u(XMAX-1, N+1) \\
& + H_T(XMAX-1, N)\ u(XMAX-1, N-1) \\
& + I_T(XMAX-1, N)\ u(XMAX-1, N) \\
& + J_T(XMAX-1, N)\ u(XMAX-2, N)
\end{aligned}
\qquad (4.33)
$$

The coefficients of the variables at the inner mesh points are given in Appendix G.

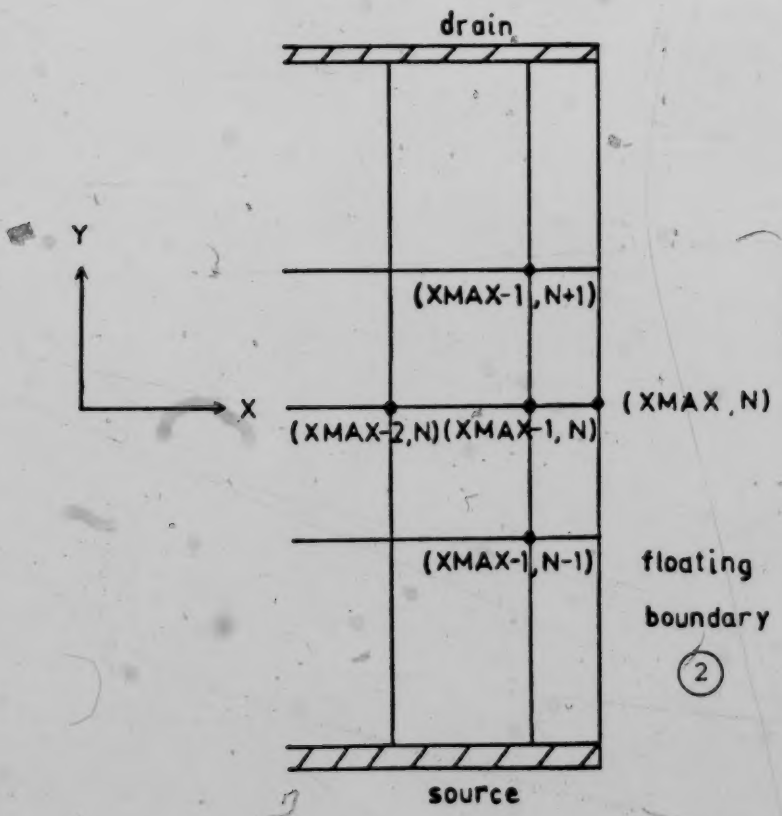

Fig. 4.4 Discretisation of (4.24) at (2)

(ii) At the region between the drains (denoted by (3) in Fig. 4.2) we discretise eqn. (4.23), (see Fig. 4.5) and summarising the results in vector form :

$$
\begin{aligned}
u(M,\ YMAX) = {} & P_T(M,\ YMAX-1)\ u(M+1,\ YMAX-1) \\
& + Q_T(M,\ YMAX-1)\ u(M-1,\ YMAX-1) \\
& + R_T(M,\ YMAX-1)\ u(M,\ YMAX-1) \\
& + S_T(M,\ YMAX-1)\ u(M,\ YMAX-2)
\end{aligned}
\qquad (4.34)
$$

The coefficients of the variables at the inner mesh points, i.e. P_T , Q_T , R_T and S_T are given in Appendix G. The variables at the mesh points on the floating boundary lines (specified by regions (1), (2) and (3) are eliminated from eqn. (4.31) by (4.32), (4.33) and (4.34).

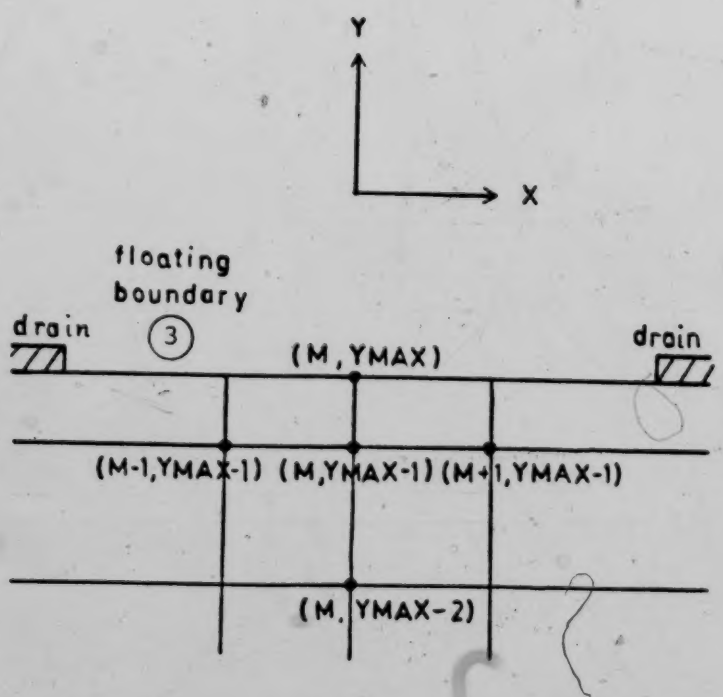

Fig. 4.5 Discretisation of (4.23) at (3)

4.5.2 Solution Procedure

The solution of eqn.(4.31) is a very large problem because of the number of mesh points in both the x and y-directions, e.g. $1 \leq M \leq 50$ and $1 \leq N \leq 50$ would result in 2500 equations being solved simultaneously. Hence, the choice of an iterative method (SLOR) [5,37], as opposed to a direct solution method such as Gaussian elimination.

A specific feature of the SLOR method is to regard the unknown quantities on two neighbouring points u(M,N-1) and u(M,N+1) as already known. Hence, eqn. (4.31) becomes,

$$B_T(M, N)\ u(M, N) + D_T(M, N)\ u(M-1, N) + E_T(M, N)\ u(M+1, N) = F(M) \quad , \tag{4.35}$$

where

$$F(M) = F_T(M, N) - A_T(M, N)\ u(M, N-1) - C_T(M, N)\ u(M, N+1)$$

for $1 \leq M \leq XMAX-1$.

Eqn. (4.35) is solved with the necessary modification in coefficients [5] according to the boundary conditions to fit each individual case. The execution of the SLOR method is described in the flow chart shown in Fig. 4.6.

The actual computation time and the number of SLOR cycles depend on the initial guess values of u, the choice of the relaxation parameter w and the device geometry, i.e. the aspect ratios and drain separations. For example, a MOSFET with dimensions W = L = 4 μm, a drain separation, d = 2 μm, V_{GS} = 3 V and V_{DS} = 1 V needs approximately 1500-2000 SLOR cycles for full convergence. This was for a relative precision, $\varepsilon = 10^{-4}$ (see Fig. 4.6). Working with double-precision floating-point arithmetic and a grid size of 50 x 50 nodes (XMAX = 50, YMAX = 50), the two dimensional simulations of the split-drain magnetic field sensor required 0.75 to 1 Mbyte of memory. As for the initial guess, the variable u was provided with linear

values, i.e.

$$u^0(M,\ N) = \left[\frac{u_{D1} + u_{D2}}{2} - u_S \ \Big/\ (YMAX-1)(N-1) \right] + u_S \qquad (4.36)$$

for $1 \leq N \leq YMAX$ and $1 \leq M \leq XMAX$,

where u_{D1} , u_{D2} and u_S are defined by (4.19), (4.20) and (4.21) respectively. A value of w between 1.5 and 1.75 was found to be an optimum range for the nature of the given initial guess (4.36) and for a variety of drain separations and bias voltages.

For the Newton-Raphson iterations [41], V was provided with linear initial guess values, i.e.

$$V^0(M,\ N) = \left[\frac{V_{D1} + V_{D2}}{2} - V_S \ \Big/\ (YMAX-1)(N-1) \right] + V_S \qquad (4.37)$$

for $1 \leq N \leq YMAX$ and $1 \leq M \leq XMAX$,

where V_{D1} , V_{D2} are the voltages at the drains and V_S is the source voltage (see Fig. 4.2).

The CPU time, on the Amdahl 580, is approximately 20-30 seconds for the modeling of the split-drain MOSFET's. At present, the iterations converge for not too large products of B_z and Hall mobility, say $tg\ \Theta_{Hn} \leq 0.6$.

To check if the true solution was obtained, the computed results were subject to the same series of tests described in section 3.4.3.

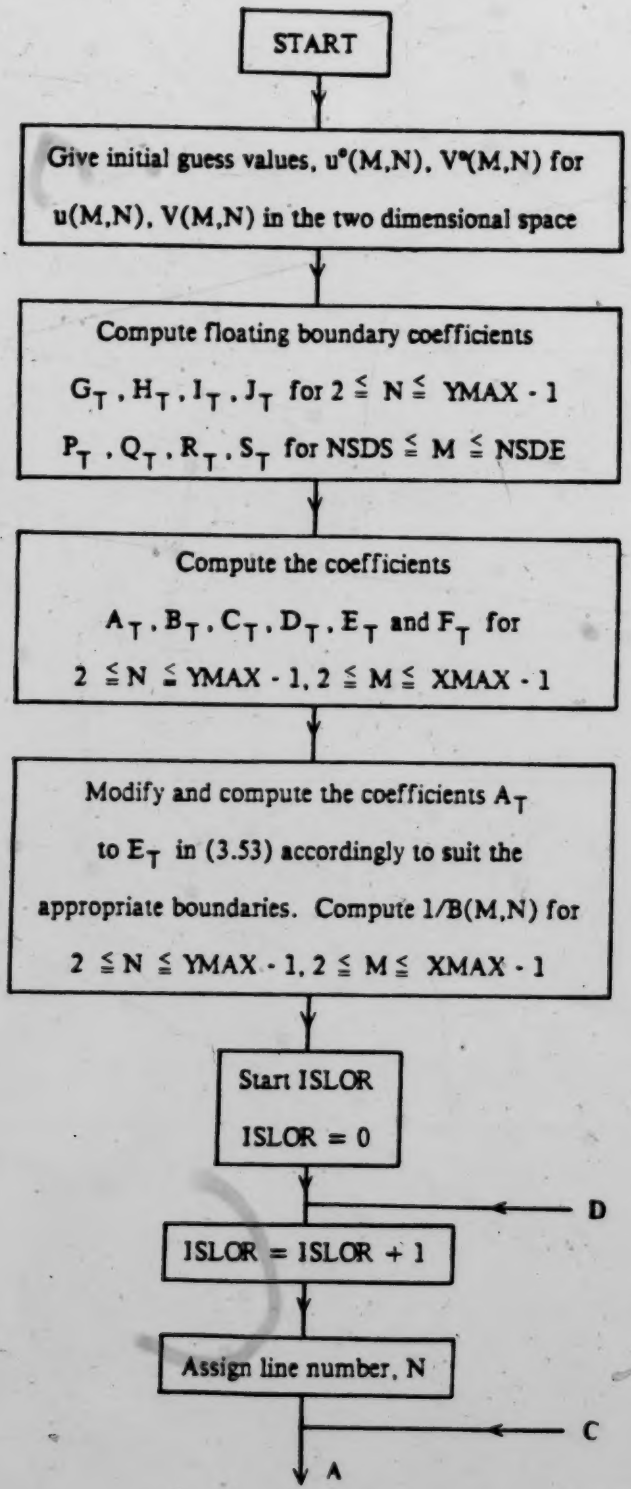
START
Give initial guess values, u°(M,N), V°(M,N) for u(M,N), V(M,N) in the two dimensional space
Compute floating boundary coefficients G_T, H_T, I_T, J_T for $2 \leq N \leq YMAX - 1$ P_T, Q_T, R_T, S_T for $NSDS \leq M \leq NSDE$
Compute the coefficients A_T, B_T, C_T, D_T, E_T and F_T for $2 \leq N \leq YMAX - 1, 2 \leq M \leq XMAX - 1$
Modify and compute the coefficients A_T to E_T in (3.53) accordingly to suit the appropriate boundaries. Compute 1/B(M,N) for $2 \leq N \leq YMAX - 1, 2 \leq M \leq XMAX - 1$
Start ISLOR
ISLOR = 0
D
ISLOR = ISLOR + 1
Assign line number, N
C
A

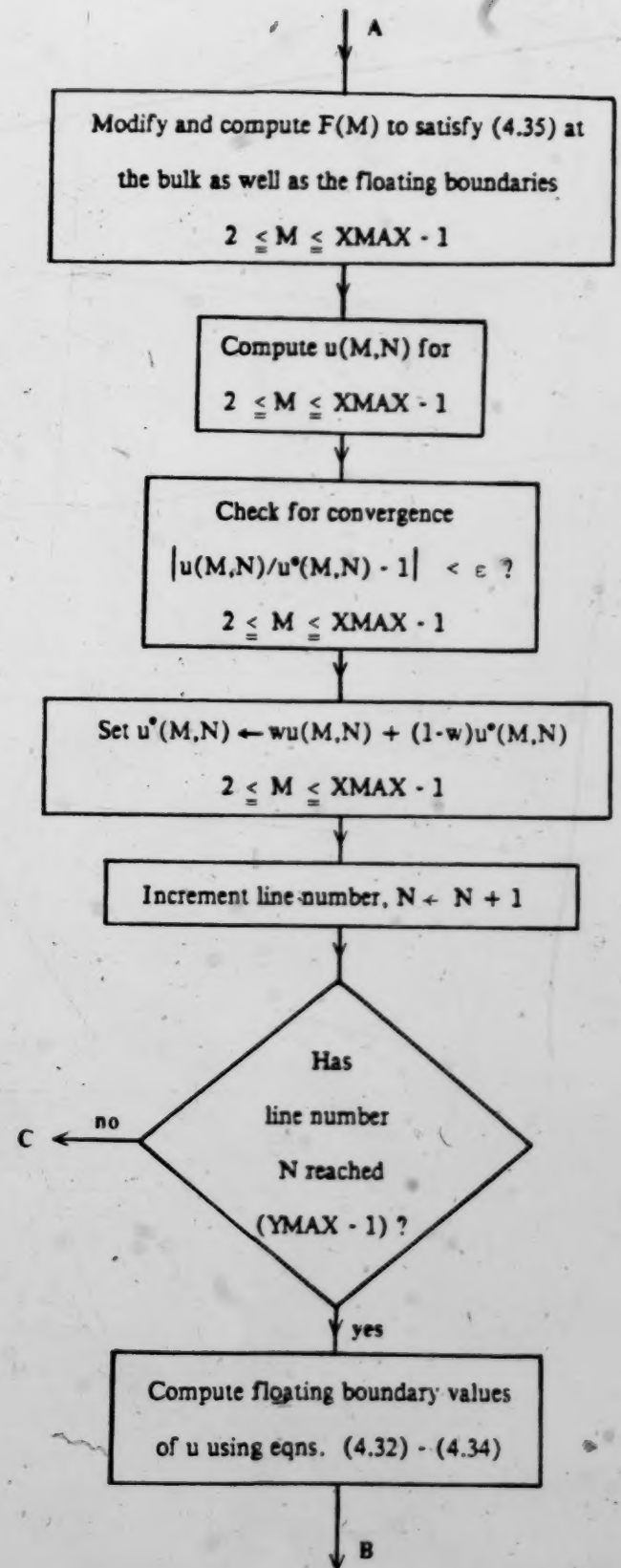
A
Modify and compute F(M) to satisfy (4.35) at the bulk as well as the floating boundaries
2 ≤ M ≤ XMAX - 1
Compute u(M,N) for
2 ≤ M ≤ XMAX - 1
Check for convergence
|u(M,N)/u*(M,N) - 1| < ε ?
2 ≤ M ≤ XMAX - 1
Set u*(M,N) ← wu(M,N) + (1-w)u*(M,N)
2 ≤ M ≤ XMAX - 1
Increment line number, N ← N + 1
Has line number N reached (YMAX - 1) ?
no
C
yes
Compute floating boundary values of u using eqns. (4.32) - (4.34)
B

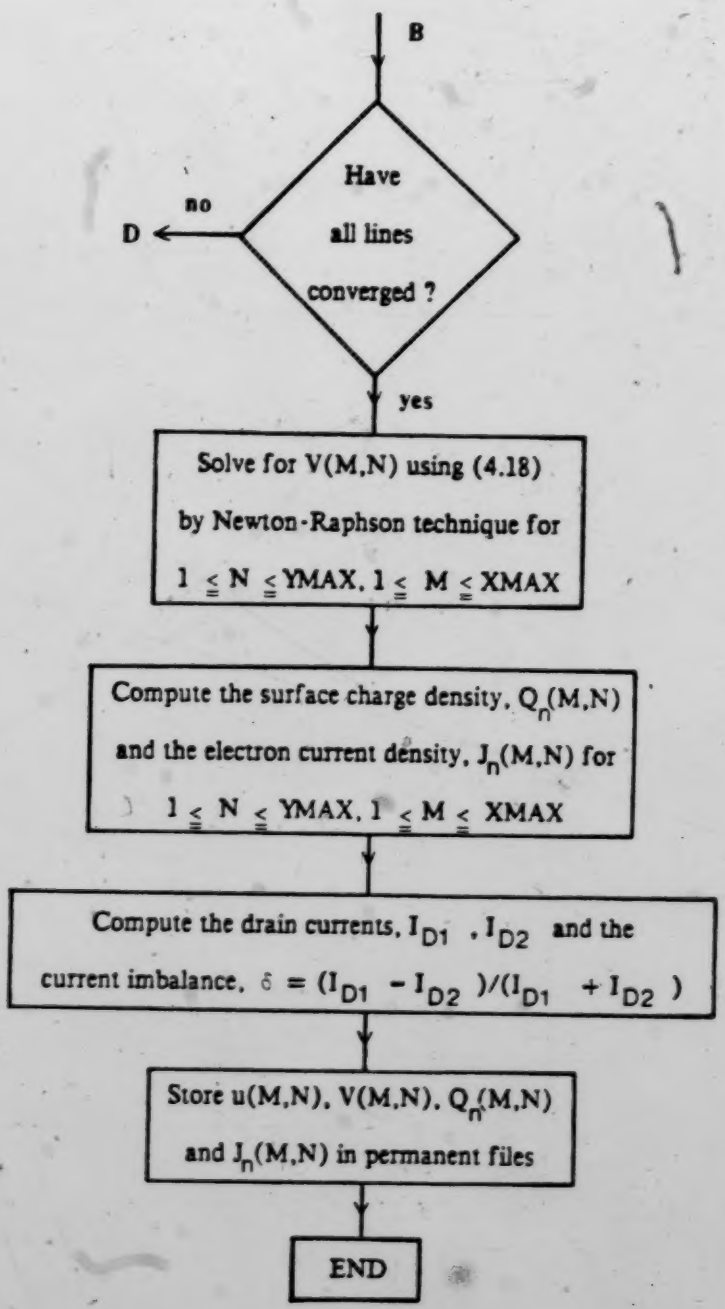
B
Have all lines converged ?
no
D
yes
Solve for V(M,N) using (4.18) by Newton-Raphson technique for 1 ≤ N ≤ YMAX, 1 ≤ M ≤ XMAX
Compute the surface charge density, Q_n(M,N) and the electron current density, J_n(M,N) for 1 ≤ N ≤ YMAX, 1 ≤ M ≤ XMAX
Compute the drain currents, I_{D1} , I_{D2} and the current imbalance, $\delta = (I_{D1} - I_{D2})/(I_{D1} + I_{D2})$
Store u(M,N), V(M,N), Q_n(M,N) and J_n(M,N) in permanent files
END

Fig. 4.6 Flow-chart of the solution procedure

4.6 Results and Discussion

The distributions of electric potential, current density and surface charge are computed for N-channel MOSFET's (uniform and split-drain configurations) for a variety of aspect ratios, drain separations, operating voltages and field strengths. The magnetic field is perpendicular to the device plane. The devices are in the linear region of operation [42] with bulk doping density, $N_A = 10^{15}$ cm^{-3}, oxide thickness, $t_{ox} = 100$ nm and threshold voltage, $V_T = 1$ V.

Figs. 4.7 and 4.8 compare equipotential and current lines in a uniform drain NMOS [42], for field strengths of 1 t and 3 t. Here $V_{DS} = 1$ V, $V_{GS} = 3$ V and $V_S = 0$ V. In Fig. 4.9, we see the surface charge density for the device operated close to the pinch-off region, $V_{DS} = 3.2$ V, $V_{GS} = 5$ V and $V_S = 0$ V. As the device is operated closer to the saturation region, a somewhat distributed pinch-off region is found because of the magnetic field. Fig. 4.10 shows equipotential and current lines for the device shown in Fig. 4.9. As opposed to the results obtained previously for the n-type silicon slab [16,17], the potential lines tend to crowd at the vicinity of the drain. Figs. 4.11-4.13 illustrate equipotential and current lines for a split-drain MOSFET for different aspect ratios, W/L and drain separations, d. The operating voltages are $V_{D1S} = V_{D2S} = 1$ V, $V_{GS} = 3$ V, $V_S = 0$ V and the magnetic field strength is 1 t.

The sensitivity defined in terms of the relative current imbalance in the two drains, viz. $\delta = (I_{D1} - I_{D2})/(I_{D1} + I_{D2})$, is studied for the various MOSFET geometries mentioned above [42]. There is no notable change in sensitivity with fluctuations in the operating voltages. The sensitivity change becomes notable only when fluctuations in the gate bias are large, e.g. doubling the gate voltage leads to a significant drop in sensitivity. This is due to the strong dependence of the mobility of the electric field in the z-direction (see Fig. 4.1).

The results suggest that the relative current imbalance, δ, depends more strongly on the absolute values of L or W rather than the aspect ratio [42,43]. This is shown in Figs. 4.14 - 4.16 for aspect ratios W/L = 25 μm/25 μm, W/L = 5 μm/25 μm and W/L = 100 μm/25 μm respectively. It is found that narrowing the channel down from 25 μm to 5 μm (Fig. 4.15) leads to only a slight increase in sensitivity, while making the channel broader leads to a less abrupt carrier

deflection close to the drains, resulting in a substantial sensitivity decrease (Fig. 4.16).

From the point of view of keeping the device small, but allowing for the minimal drain separation required by the design rules, the square geometry seems to be favourable [43]. A circuit configuration matched to the square device (W = L =25 μm, d = 5μm) is shown in Fig. 4.17. To achieve the maximum attainable sensitivities the drain voltages V_{D1S}, V_{D2S} are put at the same potential in order to avoid any shunting effects between the drains and the device is operated at low gate voltages, e.g. $V_T < V_{GS} < 5$ V.

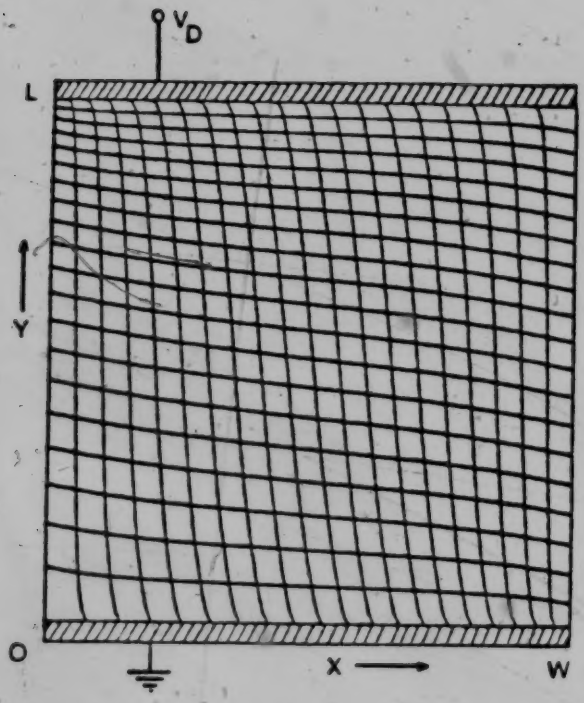

Fig. 4.7 Equipotential and current lines for

W = L = 4 μm, B = 1 t

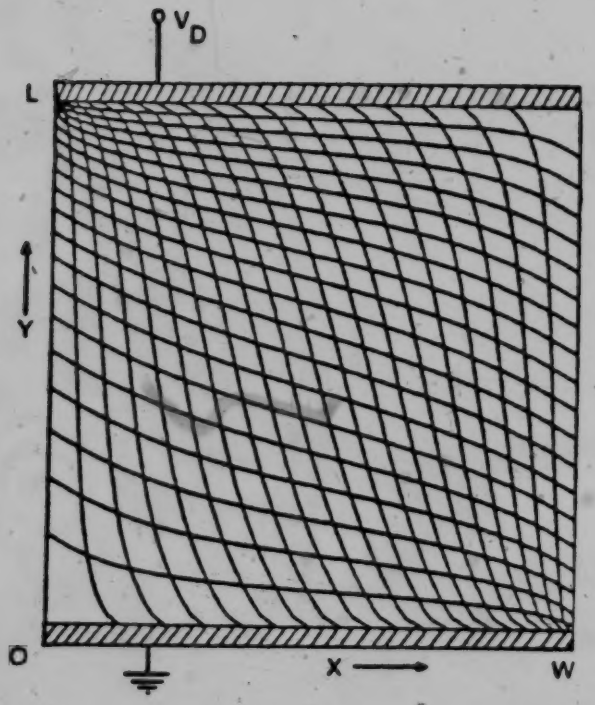

Fig. 4.8 Equipotential and current lines for

W = L = 4 μm, B = 3 t

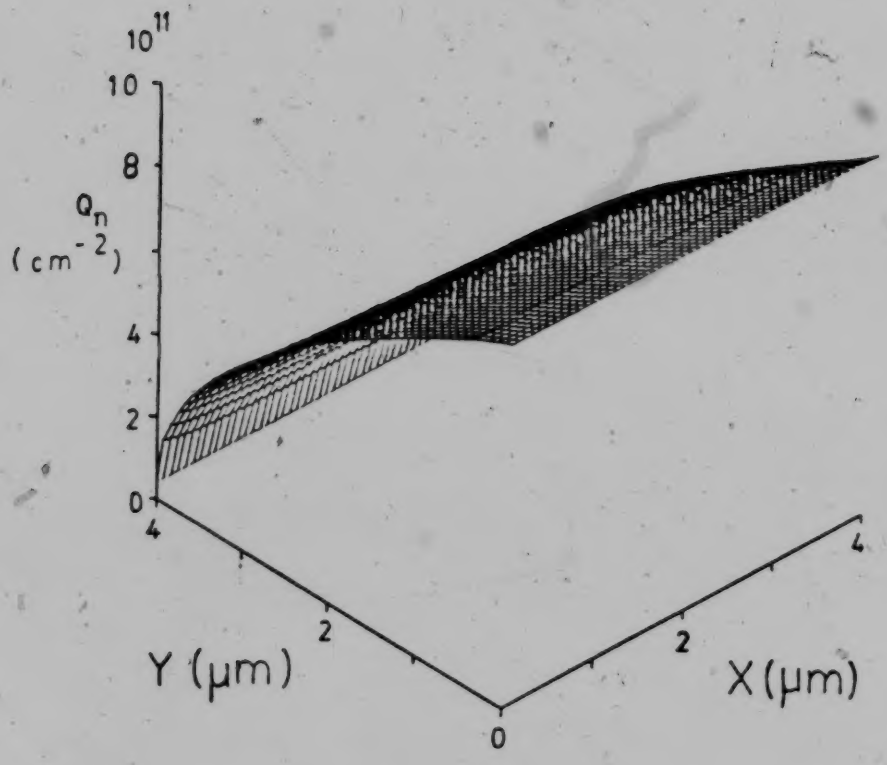

Fig. 4.9 Surface charge density for W = L = 4 μm, B = 1 t

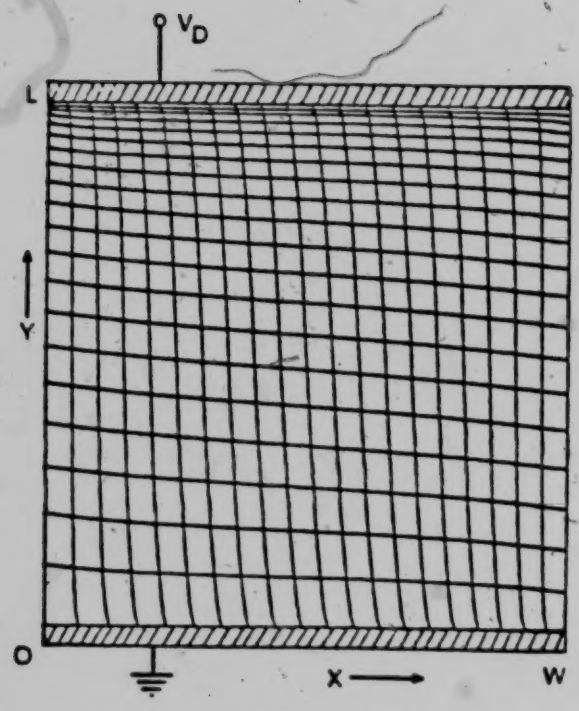

Fig. 4.10 Equipotential and current lines for W = L = 4 μm, B = 1 t

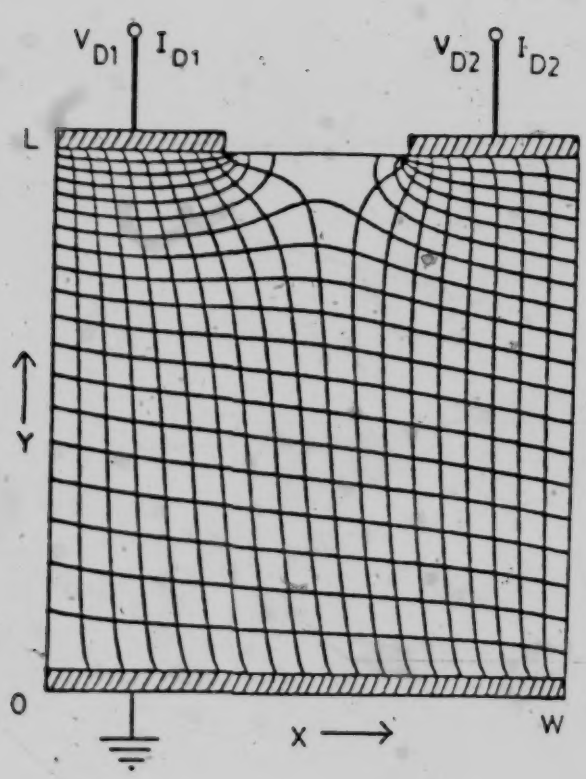

Fig. 4.11 Equipotential and current lines for W/L = 4 μm/4 μm, d = 1.4 μm, B = 1 t

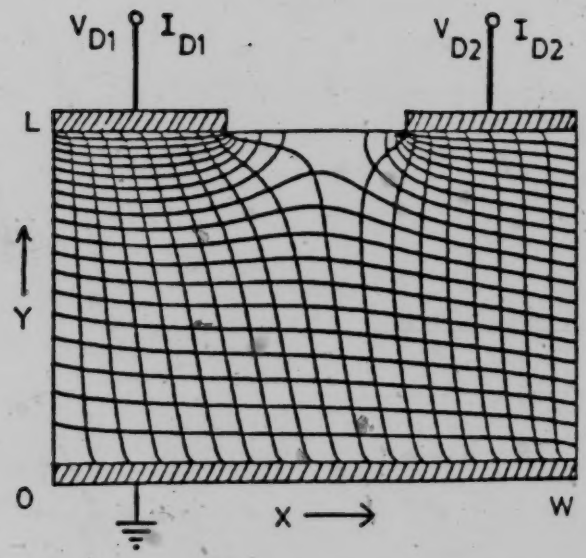

Fig. 4.12 Equipotential and current lines for W/L = 22 μm/14 μm, d = 7.63 μm, B = 1 t

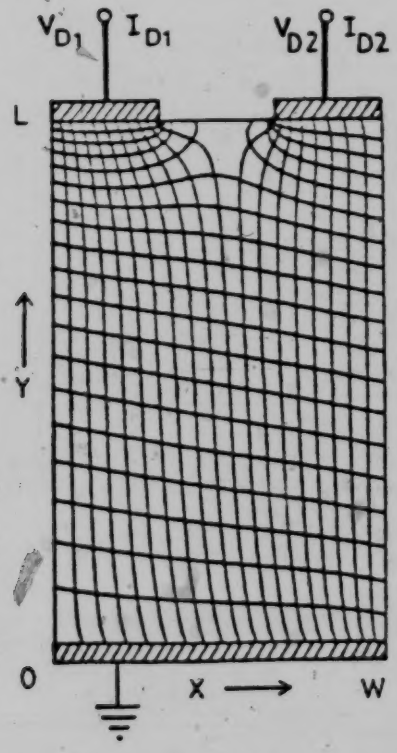

Fig. 4.13 Equipotential and current lines for W/L = 14 μm/22 μm, d = 4.9 μm, B = 1 t

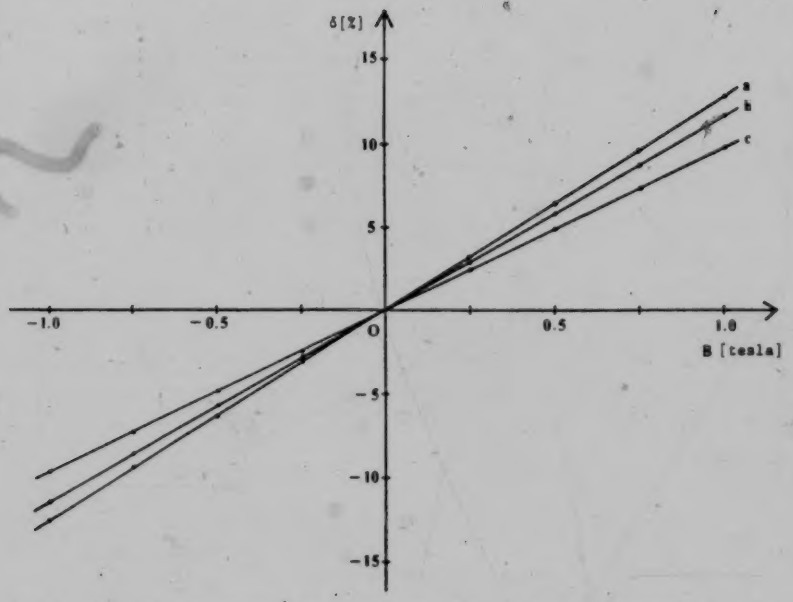

Fig. 4.14 Relative current imbalance, δ as a function of magnetic field, B for a square channel NMOS, W = L = 25 μm, for different relative drain separations : d/W = 0.05 (curve a), d/W = 0.2 (curve b), d/W = 0.6 (curve c)

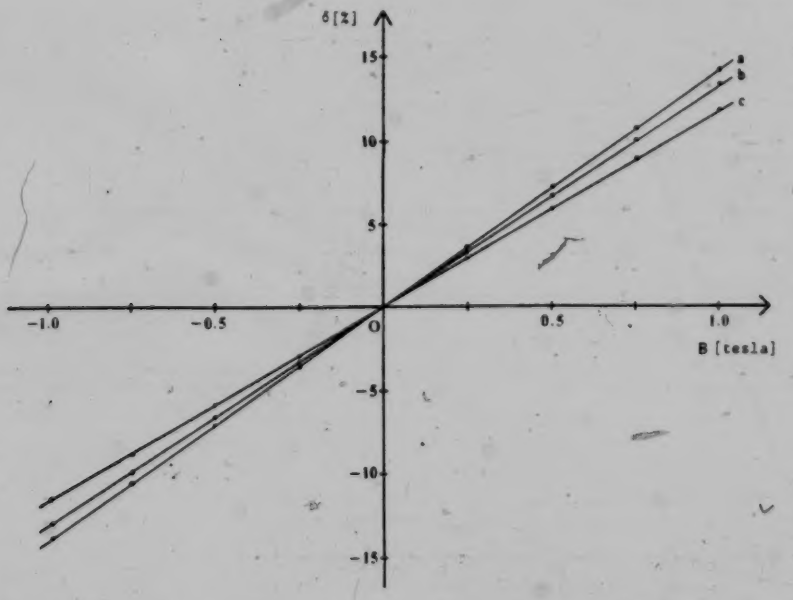

Fig. 4.15 Same as Fig. 4.14 but W/L = 5 μm/25 μm

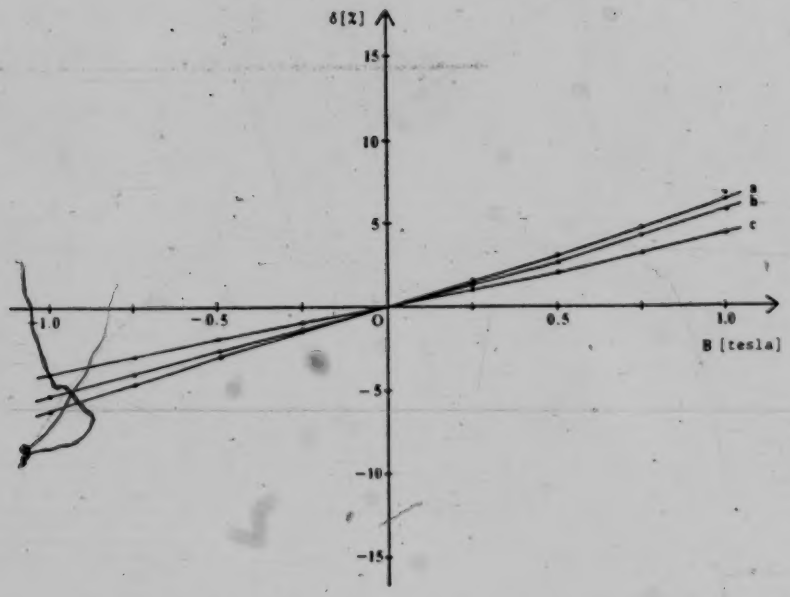

Fig. 4.16 Same as Fig. 4.14 but W/L = 100 μm/25 μm

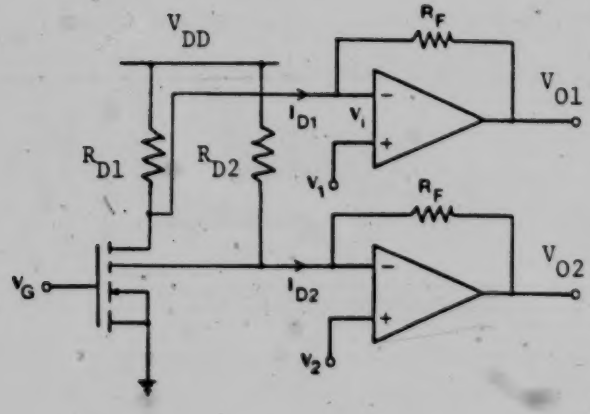

Fig. 4.17 Schematic of the square channel device in circuit

5. CONCLUSION AND OUTLOOK

Semiconductor devices subject to an external magnetic field have been modeled numerically using standard methods [3-5,28,44] but incorporating the magnetic field into the current density equations and the boundary conditions. To obtain a stable solution method, the generalisation of the well-known Scharfetter-Gummel scheme has been used in the case of two dimensions and nonzero magnetic field. The results show the important point that the two dimensional distributions of potential and current density cannot be easily described in terms of the simple analytical models such as Hall voltage, Lorentz deflection or magnetoconcentration ; this is due to the intricate combination of the magnetic field and the boundary conditions. Only in certain limits of the device geometry can the action of the field be visualised in terms of these simple analytical models.

Presently, the algorithm is being extended to p^+-i-n^+ devices and triple-drain MOSFET's. In the p^+-i-n^+ device, split-contacts are incorporated and the sensitivity of the device to the magnetic field is measured as the relative current imbalance between the contacts [36]. It has been found that, if the diffusion lengths of the carriers are adjusted suitably to the width and length of the p^+-i-n^+ device, sensitivity figures superior to those of Hall plate devices are achieved. With split-drain MOSFET's, by introducing an additional drain in the 'split' region, the sensitivity figures obtained are substantially higher than those of dual-drain devices [45]. The sensitivity of the triple-drain MOSFET's is taken to be the relative current imbalance between the outer two drains.

With these results, future work may extend the numerical algorithm to magnetotransistors for a variety of device configurations and investigating the signal-to-noise ratio limitations on the sensitivity of the devices modeled so far. In low frequency applications (e.g. 60 Hz), the dominant type of noise in MOSFET's is flicker (1/f) noise. Efforts should be concentrated on being able to include the magnetic-field effects in one of the existing circuit simulation programs, e.g. SPICE, thus allowing the evaluation and testing of the different sensor models for future computer aided design of monolithic integrated magnetic-field sensors that could include digital signal processing

such as sampling and A/D conversion. This would also allow the optimisation of the design rules such that 'stray' magnetic fields have little or no influence on device characteristics when operated in a magnetic environment.

Integrated Si MFS share problems of noise, temperature-coefficient, offset, nonlinearity and frequency-dependence with comparable nonmagnetic devices and analog IC's of the same technology, e.g. the offset due to nonideal device geometry and the piezoresistive effect of Si. Some of those problems can possibly be overcome by using procedures known from analog IC design and careful process technology [1].

6. REFERENCES

[1] H. P. Baltes, 'Magnetic Sensors', *European Physics Society, 6th General Conference "Trends in Physics"*, Prague, Aug. 27-31, 1984, Technical Digest, p. 513 and Proceedings in press.

[2] V. Zieren, 'Integrated silicon multicollector magnetotransistors', *Ph.D Thesis*, Delft Technical University, 1983.

[3] Proc. NASECODE III, Galway, *Numerical Analysis of Semiconductor Devices and Integrated Circuits*, ed. by J. J. H. Miller, Boole Press, Dublin, 1983.

[4] W. L. Engl, H. K. Dirks and B. Meinerzhagen, 'Device Modeling', *Proc. IEEE*, vol. 71, pp. 10-33, 1983.

[5] M. Kurata, *Numerical Analysis of Semiconducter Devices*, Lexington, Toronto, 1982.

[6] V. Zieren and B. P. M. Duyndam, 'Magnetic-field-sensitive multi-collector n-p-n transistor', *IEEE Trans. Electron Devices*, ED-29, pp. 83-90, 1980.

[7] A. W. Vinal and N. A. Masnari, 'Magnetic transistor behavior explained by modulation of emitter injection, not carrier deflection', *IEEE Electron Device Lett.*, EDL-3, pp. 203-205, 1982.

[8] R. S. Popovic and H. P. Baltes, 'An investigation of the sensitivity of the magnetotransistors', *IEEE Electron Device Lett.*, EDL-4, pp. 51-53, 1983.

[9] Solid State Transducers 1983, Technical Digest, pp. 55-56 and 78-79.

[10] R. S. Popovic and H. P. Baltes, 'A CMOS Magnetic Field Sensor', *IEEE J. Solid-State Circuits*, SC-18, pp. 426-428, 1983.

[11] S. Kordic, V. Zieren and S. Middelhoek, *IEDM 1983, Technical Digest*, pp. 631-634.

[12] R. S. Popovic, H. P. Baltes and F. Rudolf, 'An integrated silicon magnetic field sensor using the magnetodiode principle', *IEEE Trans. Electron Devices*, ED-31, No. 3, pp. 286-291, 1984.

[13] V. Zieren, S. Kordic, and S. Middelhoek, 'Comment on magnetic transistor behaviour explained by modulation of emitter injection, not carrier deflection', *IEEE Electron Device Lett.*, EDL-3, pp. 394-395, 1982.

[14] A. W. Vinal and N. A. Masnari, ''Response to 'Comment on magnetic transistor behaviour explained by modulation of emitter injection, not carrier deflection''', *IEEE Electron Device Lett.*, EDL-3, pp. 396-397, 1982.

[15] R. F. Wick, 'Solution of the field problem of the Germanium Gyrator', *J. of Applied Physics*, vol.25, pp. 741-756, 1954.

[16] L. Andor, H. P. Baltes, A. Nathan, and H. G. Schmidt-Weinmar, 'Carrier transport in semiconductor magnetic field sensors', *IEDM 1983, Technical Digest*, pp. 635-638.
(see Appendix D)

[17] H. P. Baltes, L. Andor, A. Nathan and H. G. Schmidt-Weinmar, 'Two-dimensional numerical analysis of a silicon magnetic field sensor', *IEEE Trans. Electron Devices*, ED-31, No. 7, pp. 996-999, 1984.
(see Appendix E)

[18] H. Pfleiderer, 'Magnetodiode model', *Solid State Electronics*, vol. 15, pp. 335-353, 1972.

[19] R. A. Smith, '*Semiconductors*', Cambridge University Press, 2nd ed., Cambridge, 1977.

[20] E. H. Hall, 'On a new action of the magnet on electric currents', *Am. J. Math.*, 2, pp. 287-292, 1879.

[21] R. C. Gallagher and W. S. Corak, 'A metal-oxide-semiconductor (MOS) Hall element', *Solid-State Electronics*, vol. 9, pp. 571-580, 1966.

[22] S. Takamiya and K. Fujikawa, 'Differential amplification magnetic sensor', *IEEE Trans. Electron Devices*, ED-19, no. 10, pp. 1085-1090, 1972.

[23] R. S. Popovic and H. P. Baltes, 'Magnetic field effect and negative differential resistance in bipolar transistors', *Proc. 12th ESSDERC*, Munich (FRG), pp. 96-97, 1982.

[24] G. Kamarinos, P. Viktorovitch, S.Christoloveneau, J. Borrel and R.Staderini, 'Silicon on sapphire magnetodiodes of high sensitivities', *IEDM Dig. Tech. papers*, Washington, D.C.(USA), pp. 114a-114c, 1977.

[25] E. C. Hudson, Jr., 'Semiconductive magnetic transducer', U. S. Patent, no. 3, 389, 230, patented June 18, 1968.

[26] P. W. Fry and S. J. Hoey, 'A silicon MOS magnetic field transducer of high sensitivity', *IEEE Trans. Electron Devices*, ED-16, no. 1, pp. 35-39, 1969.

[27] W. N. Carr and S. T. Hong , 'The MAGFET : a new integrated circuit building block', *SWIEECO Record of Tech. papers*, 22, pp. 166-170, 1970.

[28] H. H. Heimeier, 'A two-dimensional numerical analysis of a silicon N-P-N transistor', *IEEE Trans. Electron Devices*, ED-20, pp. 708-714, 1973.

[29] J. L. Blue and C. L. Wilson, 'Two-dimensional analysis of semiconductor devices using general-purpose interactive PDE software', *IEEE Trans. Electron Devices*, ED-30, no. 9, pp. 1056-1070, 1983.

[30] D. M. Caughey and R. F. Thomas, 'Carrier mobilities in silicon empirically related to doping and field', *Proc. of IEEE (Letters)*, pp. 2192-2193, 1967.

[31] S. M. Sze, *Physics of Semiconductor Devices*, 2nd ed., New York : Wiley, 1981.

[32] R. N. Hall, 'Electron-hole recombination in germanium', *Physical Review*, 87, pp. 387, 1952, and W. Shockley and W. T. Read, 'Statistics of the recombination of holes and electrons', *Physical Review*, 87, pp. 835, 1952.

[33] D. L. Scharfetter and H. K. Gummel, 'Large-signal analysis of a silicon read diode oscillator', *IEEE Trans. Electron Devices*, ED-16, pp. 64, 1969.

[34] M. Rudan and R. Guerrieri, 'Relevant problems in the numerical simulation of semiconductor devices using the finite element method', in : *Numerical Analysis of Semiconductor Devices and Integrated Circuits*, ed. by J. J. H. Miller, Boole Press, Dublin, 1983.

[35] P. E. Cottrell and E. M. Buturla, 'Two-dimensional static and transient simulation of mobile carrier transport in a semiconductor', *Proc. of NASECODE I Conference*, B. T. Browne and J. J. H. Miller eds., Boole Press, Dublin, pp. 31-64, 1979.

[36] L. Andor, H. P. Baltes, A. Nathan and H. G. Schmidt-Weinmar, 'Numerical modeling of magnetic-field-sensitive semiconductor devices', *IEEE Trans. Electron Devices*, submitted.

[37] R. S. Varga, *Matrix Iterative Analysis*, Prentice Hall, 1962.

[38] H. G. Schmidt-Weinmar, L. Andor, H. P. Baltes and A. Nathan, 'Numerical modeling of silicon magnetic field sensors : magnetoconcentration effects in split-metal-contact devices', *IEEE-Intermag 1984*, to be published in *IEEE Trans. on Magnetics*, Sept. (1984).
(see Appendix F)

[39] G. D' Emma, private communication.

[40] K. Yamaguchi, 'Field-dependent mobility model for two-dimensional numerical analysis of MOSFET's', *IEEE Trans. Electron Devices*, ED-26, pp. 1068-1074, 1979.

[41] R. L. Burden, J. D. Faires, A. C. Reynolds, *Numerical Analysis*, Prindle, Weber and Schmidt, Boston, 1978.

[42] H. P. Baltes, L. Andor, A. Nathan and H. G. Schmidt-Weinmar, 'Advances in modeling magnetic semiconductor devices', *Proc. MIEL-84*, pp. 104-116, May 7-9, Nis, Yugoslavia, 1984.

[43] A. Nathan, L. Andor, H. P. Baltes and H. G. Schmidt-Weinmar, 'Two-dimensional modeling of a MOS magnetic field sensor', *IEEE J. Solid-State Circuits*, in press.
(see Appendix H)

[44] M. S. Mock, *Analysis of Mathematical Models of Semiconductor Devices*, Boole Press, Dublin, 1983.

[45] A. Nathan, A. M. J. Huiser, H. P. Baltes and H. G. Schmidt-Weinmar, 'A triple drain MOSFET magnetic field sensor', *Second Canadian Semiconductor Technology Conference*, Ottawa, Aug. 22-24, pp. 27-28, 1984, to be published in *Can. J. of Physics*.

APPENDIX A

Linear Interpolation of the Variables p, n and ψ.

The interpolation of the variables p, n, ψ and the simplification of the Bernoulli coefficients used in obtaining (3.30) is explained in this appendix. With reference to Fig. 3.3,

$$\psi_{A'} = \frac{\psi_1 - \psi_4 + \psi_2 - \psi_3}{2} + \psi_i \quad ,$$

$$\psi_A = \frac{\psi_i + \psi_1 + \psi_{A'} + \psi_2}{4} \quad ,$$

$$\rightarrow \quad \psi_A = \frac{\psi_i}{2} + \frac{3\psi_1}{8} + \frac{3\psi_2}{8} - \frac{\psi_3}{8} - \frac{\psi_4}{8} \quad .$$

Similarly,

$$\psi_B = \frac{\psi_i}{2} - \frac{\psi_1}{8} + \frac{3\psi_2}{8} + \frac{3\psi_3}{8} - \frac{\psi_4}{8} \quad ,$$

$$\psi_C = \frac{\psi_i}{2} - \frac{\psi_1}{8} - \frac{\psi_2}{8} + \frac{3\psi_3}{8} + \frac{3\psi_4}{8} \quad ,$$

$$\psi_D = \frac{\psi_i}{2} + \frac{3\psi_1}{8} - \frac{\psi_2}{8} - \frac{\psi_3}{8} + \frac{3\psi_4}{8} \quad ,$$

$$\psi_{AD} = \psi_A - \psi_D = 1/2\ (\psi_2 - \psi_4) \quad ,$$

$$\psi_{BA} = \psi_B - \psi_A = 1/2\ (\psi_3 - \psi_1) \quad ,$$

$$\psi_{CB} = \psi_C - \psi_B = 1/2\ (\psi_4 - \psi_2) \quad ,$$

$$\psi_{DC} = \psi_D - \psi_C = 1/2\ (\psi_1 - \psi_3) \quad .$$

The Bernoulli coefficients in the expanded version of eqn. (3.30) can be simplified as follows;

$$B_{BA} = B_{CD} = B_{31/2} = \frac{\frac{q}{kT} \cdot \frac{1}{2}\ (\psi_3 - \psi_1)}{\exp\left[\frac{q}{kT} \cdot \frac{1}{2}\ (\psi_3 - \psi_1)\right] - 1} \quad .$$

Similarly,

$$B_{AB} = B_{DC} = B_{13/2} \quad , \qquad B_{CB} = B_{DA} = B_{42/2} \quad , \qquad B_{BC} = B_{AD} = B_{24/2} \quad .$$

At this stage eqn. (3.30) now reads

$$R_i = \frac{1}{1 + (\mu_n * B_z)^2}\ \mu_n \frac{kT}{q} \cdot \frac{1}{A_i} \left[\sum_{j=1}^{4} \frac{d_{ij}}{S_{ij}}\ (n_j B_{ji} - n_i B_{ij}) \right.$$

$$- \mu_n * B_z \{ B_{31/2}(n_B - n_C) + B_{13/2}(n_D - n_A) \qquad \text{(A.1)}$$

$$\left. + B_{24/2}(n_A - n_B) + B_{42/2}(n_C - n_D) \} \right] \quad .$$

By linearly interpolating n_A, n_B, n_C and n_D in the same fashion ψ_A, ψ_B, ψ_C and ψ_D was interpolated, we obtain

$$n_A - n_B = 1/2\ (n_1 - n_3)\ , \qquad n_C - n_D = 1/2\ (n_3 - n_1)\ ,$$

$$n_B - n_C = 1/2\ (n_2 - n_4)\ , \qquad n_D - n_A = 1/2\ (n_4 - n_2)\ .$$

Hence (A.1) can be further simplified to,

$$R_i = \frac{1}{1 + (\mu_n * B_z)^2} \frac{kT}{q} \cdot \mu_n \frac{1}{A_i} \left[\sum_{j=1}^{4} \frac{d_{ij}}{S_{ij}} (n_j B_{ji} - n_i B_{ij}) \right. \qquad (A.2)$$

$$\left. - \frac{\mu_n * B_z q}{4kT} \{(n_1 - n_3)(\psi_4 - \psi_2) + (n_4 - n_2)(\psi_3 - \psi_1)\} \right] .$$

In obtaining (A.2) the following simplification was used,

$$B_{xy} - B_{yx} = \frac{\frac{q}{kT}(\psi_x - \psi_y)}{e^{\frac{q}{kT}(\psi_x - \psi_y)} - 1} - \frac{\frac{q}{kT}(\psi_y - \psi_x)}{e^{\frac{q}{kT}(\psi_y - \psi_x)} - 1}$$

$$= (\psi_y - \psi_x) \frac{q}{kT} \quad .$$

The hole continuity equation was simplified on the same basis of interpolation.

A better interpolation technique for the variables p, n and ψ maintaining consistency with Scharfetter-Gummel scheme is described below.

$$\psi_A = \frac{1}{2} (\psi_1 + \psi_2) \quad ,$$

$$\psi_B = \frac{1}{2} (\psi_i + \psi_{B'}) \quad ,$$

$$\psi_C = \frac{1}{2} (\psi_3 + \psi_4) \quad ,$$

$$\psi_D = \frac{1}{2} (\psi_i + \psi_{D'}) \quad .$$

Equating the integrals obtained when eqn. (3.21) was integrated over s (first between i and A', then between i and A) we obtain after simplifications,

$$n_A = \frac{2[n_{A'} B_{A'i} - n_i B_{iA'}]}{B_{Ai}} + \frac{n_i B_{iA}}{B_{Ai}} \quad .$$

In a similar fashion n_B, n_C and n_D are obtained. The same treatment holds for the simplification of the hole continuity equation.

APPENDIX B

Matrix and Vector Elements for the Slab Boundaries

The matrix and vector elements for the floating boundaries of the slab (see Fig. 3.2), given by eqns. (3.44) and (3.46), are described in this appendix. To avoid the lengthy expressions contained in the matrix and vector elements, we define the following ;

$$A_0 = \frac{kT}{q[p^0(I, N) + n^0(I, N)]} \quad ,$$

$$A_1 = \frac{p^0(I, N)\ n^0(I, N)\ (b_p - b_n)}{p^0(I, N) + n^0(I, N)} \left(\frac{q}{kT}\right) \quad ,$$

$$\gamma = N(I, N) - N(J, N) - HXR\ [N(J, N) - N(K, N)] \quad ,$$

$$\psi_0 = \psi^0(J, N+1) - \psi^0(J, N+1) \quad ,$$

$$\beta = p^0(I, N)\ b_p - n^0(I, N)\ b_n \quad ,$$

$$T_p = -\frac{q}{kT} p^0(I, N) \quad , \qquad T_n = \frac{q}{kT} n^0(I, N) \quad ,$$

$$\varepsilon^0 = \exp\{\frac{q}{kT} [p^0(I, N) - p^0(J, N)]\} \quad ,$$

$$\varepsilon_{k_p}^{0} = \exp\left\{b_p \frac{q}{kT}\left[\psi^0(J, N+1) - \psi^0(J, N-1)\right] - b_p \ln\left[\frac{p^0(J, N-1)}{p^0(J, N+1)}\right]\right\},$$

$$\varepsilon_{k_n}^{0} = \exp\left\{b_n \frac{q}{kT}\left[\psi^0(J, N-1) - \psi^0(J, N+1)\right] - b_n \ln\left[\frac{n^0(J, N-1)}{n^0(J, N+1)}\right]\right\}.$$

Here, $p^0(M, N)$, $n^0(M, N)$ and $\psi^0(M, N)$ are initial guess values specified at every meshpoint.

The matrix elements are:

$$g_{11} = \frac{p^0(I, N)}{p^0(J, N+1)} A_0 b_p T_n, \quad g_{12} = -\frac{n^0(I, N)}{n^0(J, N+1)} b_n A_0 T_p,$$

$$g_{13} = A_1, \quad g_{21} = g_{11}, \quad g_{22} = g_{12}, \quad g_{23} = g_{13},$$

$$g_{31} = \frac{1}{T_n} g_{11}, \quad g_{32} = \frac{1}{T_p} g_{12}, \quad g_{33} = A_0 \beta \frac{q}{kT}.$$

$$h_{11} = \frac{p^0(I, N)}{p^0(J, N-1)} A_0 b_p T_n, \quad h_{12} = \frac{n^0(I, N)}{n^0(J, N-1)} A_0 b_n T_p,$$

$$h_{13} = -A_1, \quad h_{21} = h_{11}, \quad h_{22} = h_{12}, \quad h_{23} = h_{13},$$

$$h_{31} = \frac{1}{T_n} h_{11} , \quad h_{32} = \frac{1}{T_p} h_{12} , \quad h_{33} = -A_0 \beta \frac{q}{kT} .$$

$$i_{11} = A_0 \left[T_n \frac{\varepsilon_{k_p}^0}{\varepsilon^0} - T_p (HXR + 1) \right] ,$$

$$i_{12} = A_0 T_p \left[- \varepsilon^0 \varepsilon_{k_n}^0 + (HXR + 1) \right] , \quad i_{13} = 0 ,$$

$$i_{21} = A_0 T_n \left[\frac{\varepsilon_{k_p}^0}{\varepsilon^0} - (HXR + 1) \right] ,$$

$$i_{22} = A_0 \left[T_n (HXR + 1) - T_p \varepsilon^0 \varepsilon_{k_n}^0 \right] , \quad i_{23} = 0 ,$$

$$i_{31} = \frac{1}{T_n} i_{21} , \quad i_{32} = \frac{1}{T_p} i_{12} , \quad i_{33} = 1 .$$

$$j_{11} = A_0 T_p HXR , \quad j_{12} = - j_{11} , \quad j_{13} = 0 ,$$

$$j_{21} = A_0 T_n HXR , \quad j_{22} = - j_{21} , \quad j_{23} = 0 ,$$

$$j_{31} = \frac{1}{T_p} j_{11} , \quad j_{32} = - j_{31} , \quad j_{33} = 0.$$

The vector elements are:

$$k_1 = A_1 \psi_0 + A_0 T_p \gamma , \qquad k_2 = A_1 \psi_0 + A_0 T_n \gamma ,$$

$$k_3 = \psi^0(I, N) - \psi^0(J, N) + A_0 \left(\gamma + \psi_0 \beta \frac{q}{kT}\right) .$$

$$\ell_1 = k_1 , \qquad \ell_2 = k_2 , \qquad \ell_3 = k_3 .$$

For the floating boundary (3) (see Fig. 3.2),

$$b_n = -\frac{\mu_n^* B_z h_x(1)}{h_y(N) + h_y(N-1)} , \qquad b_p = \frac{\mu_p^* B_z h_x(1)}{h_y(N) + h_y(N-1)} ,$$

$$HXR = h_x(1)/h_x(2) , \qquad I = 1 , \qquad J = 2 \text{ and } K = 3 .$$

For the floating boundary (4) (see Fig. 3.2) ,

$$b_n = \frac{\mu_n^* B_z h_x(XMAX - 1)}{h_y(N) + h_y(N - 1)} , \qquad b_p = -\frac{\mu_p^* B_z h_x(XMAX - 1)}{h_y(N) + h_y(N - 1)} ,$$

$$HXR = h_x(XMAX - 1)/h_x(XMAX - 2) , \qquad I = XMAX , \qquad J = XMAX - 1$$

and K = XMAX - 2.

APPENDIX C

Matrix and Vector Elements for the Bulk

In this appendix, the matrix and vector elements related to the coefficients of the continuity and Poisson's equations given by eqn. (3.50), are described. To avoid the lengthy expressions contained in the elements, the following definitions are made :

$$\beta_x(M) = \frac{q}{kT}\left[\psi^0(M,\ N) - \psi^0(M+1,\ N)\right] \quad ,$$

$$\beta_y(N) = \frac{q}{kT}\left[\psi^0(M,\ N) - \psi^0(M,\ N+1)\right] \quad .$$

$$D_p = \frac{\mu_p^*\, B_z}{1 + (\mu_p^*\, B_z)^2} \quad \frac{\mu_p}{\left[h_y(N) + h_y(N-1)\right]\left[h_x(M) + h_x(M-1)\right]} \quad ,$$

$$D_n = \frac{-\,\mu_n^*\, B_z}{1 + (\mu_n^*\, B_z)^2} \quad \frac{\mu_n}{\left[h_y(N) + h_y(N-1)\right]\left[h_x(M) + h_x(M-1)\right]} \quad ,$$

$$\psi_0(M) = \psi^0(M-1,\ N) - \psi^0(M+1,\ N) \quad , \qquad \psi_0(N) = \psi^0(M,\ N-1) - \psi^0(M,\ N+1) \quad ,$$

$$C_p(M) = \frac{2\mu_p}{1 + (\mu_p^*\, B_z)^2} \quad \frac{1}{\left[h_x(M) + h_x(M-1)\right]} \quad ,$$

$$C_p(N) = \frac{2\mu_p}{1 + (\mu_p^*\, B_z)^2} \quad \frac{1}{\left[h_y(N) + h_y(N-1)\right]} \quad ,$$

$$C_n(M) = \frac{2\mu_n}{1 + (\mu_n^* B_z)^2} \quad \frac{1}{[h_x(M) + h_x(M-1)]} ,$$

$$C_n(N) = \frac{2\mu_n}{1 + (\mu_n^* B_z)^2} \quad \frac{1}{[h_y(N) + h_y(N-1)]} ,$$

$$\text{Bern}\{x\} = \frac{x}{e^x - 1} , \qquad \text{Bernm}\{x\} = \frac{x}{1 - e^{-x}} ,$$

$$\text{DBern}\{x\} = \frac{1}{e^x - 1} - \frac{xe^x}{(e^x - 1)^2} , \quad \text{DBernm}\{x\} = \frac{xe^x}{(e^x - 1)^2} - \frac{1}{1 - e^{-x}} .$$

The matrix and vector elements are:

$$a_{11} = -\frac{kT}{q} \frac{C_p(N)}{h_y(N-1)} \text{Bernm}\{\beta_y(N-1)\} + D_p \psi_0(M) , \quad a_{12} = 0 ,$$

$$a_{13} = \frac{C_p(N)}{h_y(N-1)} [p^0(M, N-1) \text{ DBernm}\{\beta_y(N-1)\}$$

$$+ p^0(M, N) \text{ DBern}\{\beta_y(N-1)\}] + D_p [p^0(M+1, N) - p^0(M-1, N)] ,$$

$$a_{21} = 0 , \quad a_{22} = \frac{kT}{q} \frac{C_n(N)}{h_y(N-1)} \text{Bern}\{\beta_y(N-1)\} + D_n \psi_0(M) ,$$

$$a_{23} = \frac{C_n(N)}{h_y(N-1)} \left[n^0(M, N-1)\ \mathrm{DBern}\ \{\beta_y(N-1)\} \right.$$

$$\left. + n^0(M, N)\ \mathrm{DBernm}\ \{\beta_y(N-1)\} \right] + D_n \left[n^0(M+1, N) - n^0(M-1, N) \right] ,$$

$$a_{31} = 0 , \quad a_{32} = 0 , \quad a_{33} = \frac{2}{h_y(N-1)\left[h_y(N) + h_y(N-1) \right]} .$$

$$c_{11} = - \frac{kT}{q} \frac{C_p(N)}{h_y(N)}\ \mathrm{Bern}\ \{\beta_y(N)\} - D_p\, \psi_0(M) , \quad c_{12} = 0 ,$$

$$c_{13} = \frac{C_p(N)}{h_y(N)} \left[p^0(M, N+1)\ \mathrm{DBern}\ \{\beta_y(N)\} \right.$$

$$\left. + p^0(M, N)\ \mathrm{DBernm}\ \{\beta_y(N)\} \right] - D_p \left[p^0(M+1, N) - p^0(M-1, N) \right] ,$$

$$c_{21} = 0 , \quad c_{22} = \frac{kT}{q} \frac{C_n(N)}{h_y(N)}\ \mathrm{Bernm}\ \{\beta_y(N)\} - D_n\, \psi_0(M) ,$$

$$c_{23} = \frac{C_n'(N)}{h_y(N)} \left[n^0(M, N+1)\ \mathrm{DBernm}\ \{\beta_y(N)\} \right.$$

$$\left. + n^0(M, N)\ \mathrm{DBern}\ \{\beta_y(N)\} \right] - D_n \left[n^0(M+1, N) - n^0(M-1, N) \right] ,$$

$$c_{31} = 0 , \quad c_{32} = 0 , \quad c_{33} = \frac{2}{h_y(N)\left[h_y(N) + h_y(N-1) \right]} .$$

$$d_{11} = -\frac{kT}{q}\ \frac{C_p(M)}{hx(M-1)}\ \text{Bernm}\{\beta_x(M-1)\} - D_p\,\psi_0(N)\},\qquad d_{12} = 0\ ,$$

$$d_{13} = \frac{C_p(M)}{h_x(M-1)}\ [p^0(M-1,\ N)\ \text{DBernm}\{\beta_x(M-1)\}$$

$$+\ p^0(M,\ N)\ \text{DBern}\{\beta_x(M)\}] - D_p\ [p^0(M,\ N+1) - p^0(M,\ N-1)]\ ,$$

$$d_{21} = 0\ ,\qquad d_{22} = \frac{kT}{q}\ \frac{C_n(M)}{h_x(M-1)}\ \text{Bern}\{\beta_x(M-1)\} - D_n\,\psi_0(N)\ ,$$

$$d_{23} = \frac{C_n(M)}{h_x(M-1)}\ [n^0(M-1,\ N)\ \text{DBern}\{\beta_x(M-1)\}$$

$$+\ n^0(M,\ N)\ \text{DBernm}\{\beta_x(M-1)\}] - D_n\ [n^0(M,\ N+1) - n^0(M,\ N-1)]\ ,$$

$$d_{31} = 0\ ,\qquad d_{32} = 0\ ,\qquad d_{33} = \frac{2}{h_x(M-1)[h_x(M) + h_x(M-1)]}\ .$$

$$e_{11} = -\frac{kT}{q}\ \frac{C_p(M)}{h_x(M)}\ \text{Bern}\{\beta_x(M)\} + D_p\,\psi_0(N)\ ,\qquad e_{12} = 0\ ,$$

$$e_{13} = \frac{C_p(M)}{h_x(M)}\ [p^0(M+1,\ N)\ \text{DBern}\{\beta_x(M)\}$$

$$+\ p^0(M,\ N)\ \text{DBernm}\{\beta_x(M)\}] + D_p\ [p^0(M,\ N+1) - p^0(M,\ N-1)]\ ,$$

$$e_{21} = 0 , \qquad e_{22} = \frac{kT}{q} \frac{C_n(M)}{h_x(M)} \text{ Bernm } \{\beta_x(M)\} + D_n \psi_0(N) ,$$

$$e_{23} = \frac{C_n(M)}{h_x(M)} \left[n^0(M+1, N) \text{ DBernm } \{\beta_x(M)\} \right.$$

$$\left. + n^0(M, N) \text{ DBern } \{\beta_x(M)\} \right] + D_n \left[n^0(M, N+1) - n^0(M, N-1) \right] ,$$

$$e_{31} = 0 , \qquad e_{32} = 0 , \qquad e_{33} = \frac{2}{h_x(M) \left[h_x(M) + h_x(M-1) \right]} .$$

$$b_{11} = \frac{kT}{q} C_p(N) \left[\frac{\text{Bern } \{\beta_y(N-1)\}}{h_y(N-1)} + \frac{\text{Bernm } \{\beta_y(N)\}}{h_y(N)} \right]$$

$$+ \frac{kT}{q} C_p(M) \left[\frac{\text{Bern } \{\beta_x(M-1)\}}{h_x(M-1)} + \frac{\text{Bernm } \{\beta_x(M)\}}{h_x(M)} \right]$$

$$+ \frac{n^0(M, N) - \tau_n R}{\tau_n \left[p^0(M, N) + n_i \right] + \tau_p \left[n^0(M, N) + n_i \right]} ,$$

$$b_{12} = \frac{p^0(M, N) - \tau_p R}{\tau_n \left[p^0(M, N) + n_i \right] + \tau_p \left[n^0(M, N) + n_i \right]} ,$$

$$b_{13} = - (a_{13} + c_{13} + d_{13} + e_{13}) \quad ,$$

$$b_{21} = - \frac{n^0(M, N) - \tau_n R}{\tau_n [p^0(M, N) + n_i] + \tau_p [n^0(M, N) + n_i]} \quad ,$$

$$b_{22} = - \frac{kT}{q} \; C_n(N) \left[\frac{\text{Bernm } \{\beta_y(N-1)\}}{h_y(N-1)} + \frac{\text{Bern } \{\beta_y(N)\}}{h_y(N)} \right]$$

$$- \frac{kT}{q} \; C_n(M) \left[\frac{\text{Bernm } \{\beta_x(M-1)\}}{h_x(M-1)} + \frac{\text{Bern } \{\beta_x(M)\}}{h_x(M)} \right] - b_{12} \quad ,$$

$$b_{23} = - (a_{23} + c_{23} + d_{23} + e_{23}) \quad ,$$

$$b_{31} = \frac{q}{\varepsilon_{Si}} \quad , \qquad b_{32} = - b_{31} \quad , \qquad b_{33} = - (a_{33} + c_{33} + d_{33} + e_{33}) \quad .$$

$$f_1 = - R - b_{21}\, p^0(M, N) + b_{12}\, n^0(M, N)$$

$$+ a_{13}\,[\psi^0(M, N-1) - \psi^0(M, N)] + c_{13}\,[\psi^0(M, N+1) - \psi^0(M, N)]$$

$$+ d_{13}\,[\psi^0(M-1, N) - \psi^0(M, N)] + e_{13}\,[\psi^0(M+1, N) - \psi^0(M, N)] \quad ,$$

$$f_2 = R + b_{21}\, p^0(M, N) - b_{12}\, n^0(M, N)$$

$$+ a_{23}\,[\psi^0(M, N-1) - \psi^0(M, N)] + c_{23}\,[\psi^0(M, N+1) - \psi^0(M, N)]$$

$$+ d_{23}\,[\psi^0(M-1, N) - \psi^0(M, N)] + e_{23}\,[\psi^0(M+1, N) - \psi^0(M, N)] \quad ,$$

$$f_3 = - \frac{q}{\varepsilon_{Si}}\, N(M, N) \quad .$$

In the elements b_{ij} and f_i, R denotes the discretised recombination given by eqn. (3.33).

APPENDIX D

CARRIER TRANSPORT IN SEMICONDUCTOR MAGNETIC FIELD SENSORS

L. Andor*, H.P. Baltes, A. Nathan and H.G. Schmidt-Weinmar

Department of Electrical Engineering

University of Alberta

Edmonton, Alberta, Canada T6G 2E1

ABSTRACT

We present the first two-dimensional numerical solutions of the coupled partial differential equations governing carrier drift, diffusion, generation, recombination and electric potential in the bulk of a semiconductor material in the presence of a magnetic field. Our solutions were obtained for a uniformly doped, quadratic semiconductor slab subject to boundary conditions which arise from two ohmic contacts supplying the device current.

INTRODUCTION

In the presence of a magnetic field, numerical modeling of a semiconductor device is required because of the complexity of the situation; in the bulk, the magnetic field, electric field, drift current, diffusion, generation and recombination of the carriers are all coupled to one another. Moreover, the actual bulk spatial distributions of these quantities in the device are determined by the boundary conditions specified due to the various (open or ohmic) device contacts.

BASIC EQUATIONS

In this paper, we present two-dimensional numerical solutions of the following system of coupled partial differential equations [1,2]:

$$\vec{J}_n = \frac{1}{1 + (\mu_n^* \vec{B})^2} [(q\mu_n n\vec{E} + qD_n \vec{\nabla} n) + \mu_n^* \vec{B} \times (q\mu_n nE + qD_n \vec{\nabla} n)], \quad (1)$$

$$\vec{J}_p = \frac{1}{1 + (\mu_p^* \vec{B})^2} [(q\mu_p p\vec{E} - qD_p \vec{\nabla} p) - \mu_p^* \vec{B} \times (q\mu_p p\vec{E} - qD_p \vec{\nabla} p)], \quad (2)$$

$$\frac{1}{q} \vec{\nabla} \cdot \vec{J}_n - R = 0, \quad (3)$$

$$-\frac{1}{q} \vec{\nabla} \cdot \vec{J}_p - R = 0, \quad (4)$$

$$(\vec{\nabla})^2 \psi = -\frac{q}{\varepsilon} (p - n + N), \quad (5)$$

$$R = \frac{(pn - n_i^2)}{\tau_n [p + n_i \exp(\frac{E_i - E_t}{kT})] + \tau_p [n + n_i \exp(\frac{E_t - E_i}{kT})]}. \quad (6)$$

Here, $\vec{J}_n$ and $\vec{J}_p$ represent electron and hole current densities, μ_n and μ_p the drift mobilities, μ_n^* and μ_p^* the Hall mobilities, n and p the electron and hole concentrations, D_n and D_p the diffusion constants, $\vec{E}$ the electric field, $\vec{B}$ the magnetic induction, ψ the electrostatic potential, $\vec{\nabla}$ the nabla operator, N the net doping density, q denotes the elementary charge, R is the net bulk recombination rate (SRH type), n_i the intrinsic concentration, τ_n and τ_p denote the bulk carrier lifetimes, E_t the energy level of trap centres, E_i the intrinsic Fermi level, k the Boltzmann's constant and T the absolute temperature.

Equations 3 and 4 represent the continuity equations for the stationary case and equation 5 represents Poisson's equation.

In this paper we consider a quadratic semiconductor slab with open boundaries along two opposite faces and ohmic contacts along the other two opposite faces of the slab. The magnetic field is assumed to be perpendicular to the device surface: $\vec{B} = (0, 0, B_z)$, so that all distributions in the device depend only on x and y.

For the mobilities we used [3]

$$\mu_n = (65.0 + \frac{1265}{1 + [N_T/(8.5 \cdot 10^{16} cm^{-3})]^{0.72}}) \frac{cm^2}{Vs}, \quad (7)$$

*Currently on leave from the Research Institute for Technical Physics of the Hungarian Academy of Sciences, Budapest 1, P.O.B. 76, H-1140, Hungary.

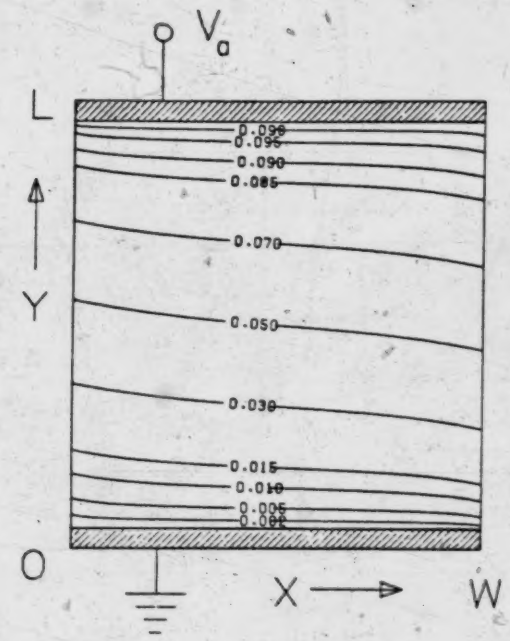

Fig. 1. Equipotential curves for the n-type silicon device, $N_- = -10^{16}\,cm^{-3}$, $V_a = 0.1$ volt, $L = W = 100\mu$ and $\vec{B} = 1$ Tesla.

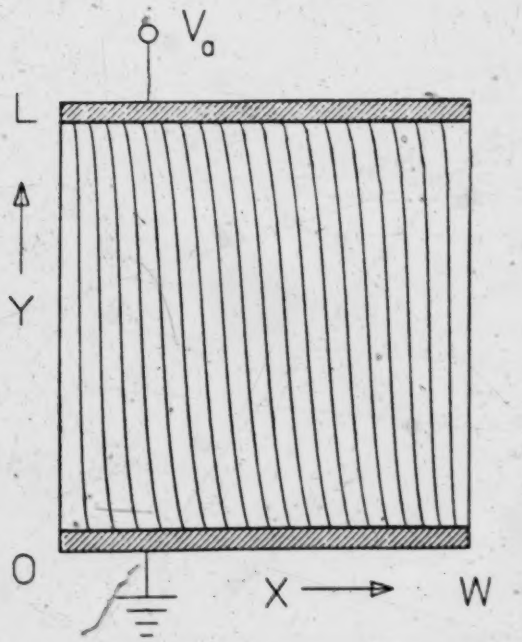

Fig. 2. Current lines corresponding to Fig. 1.

$$\mu_p = \left(47.7 + \frac{447.3}{1 + [N_I/(6.3\cdot 10^{16}\,cm^{-3})]^{0.76}}\right) \frac{cm^2}{Vs}, \quad (8)$$

where N_I denotes the total impurity concentration. For the Hall mobility, we used the relation, $\mu^* = r\mu$ where we adopted for r the value 1.92 [4].

BOUNDARY CONDITIONS

Along the ohmic contacts, we assumed [2,3]

$$pn = n_i^2. \quad (9)$$

Furthermore along the ohmic contacts we obtain for the electrostatic potential, from the condition of charge neutrality [2,3]

$$\psi = V_a + \frac{kT}{q} \sinh^{-1}\left(\frac{N}{2n_i}\right), \quad (10)$$

where V_a denotes the applied voltage.

Along the open boundaries, we have used the conditions [2,3]:

$$J_{nx} = 0, \quad (11a)$$

$$J_{px} = 0. \quad (11b)$$

In computing the equations (11), we used the equations (1) and (2), which contains the magnetic field.

Because of the non-zero magnetic field along the open boundary, we have chosen the boundary condition

$$\frac{\partial^2}{\partial x^2}(p - n + N) = 0. \quad (12)$$

This condition is considered somewhat less restrictive than proposed by Kurata [2].

NUMERICAL PROCEDURE

Following the technique given in References [2,3,5] we have put the equations (1) - (12) above in finite difference form. For the continuity equations, (3) and (4), which now include the magnetic field, we used a discretization technique similar to a generalization of the Scharfetter-Gummel scheme discussed recently by Rudan and Guerrieri [6].

Our iteration procedure is based on (i) the linearization of the equations by applying Newton's iteration principle, and (ii) the simultaneous solution of Poisson's and the continuity equations ("full coupling") [2].

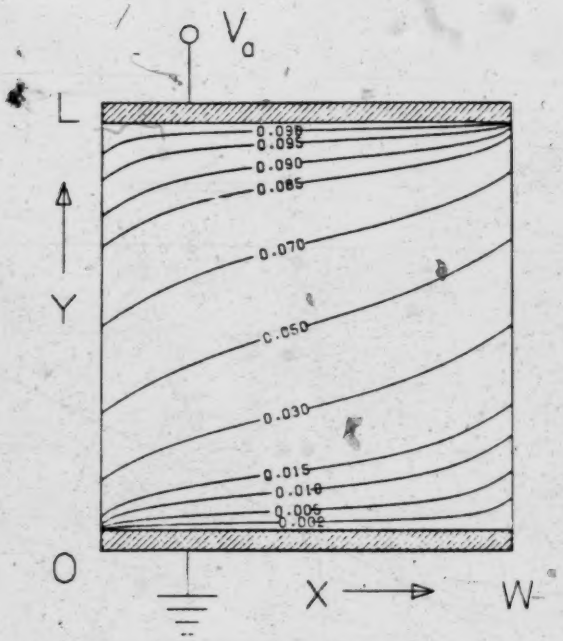

Fig. 3. Equipotential curves for the p-type silicon device, $N = 10^{16}cm^{-3}$, $V_a = 0.1$ volt, $L = W = 100\mu$ and $\vec{B} = 10$ Tesla.

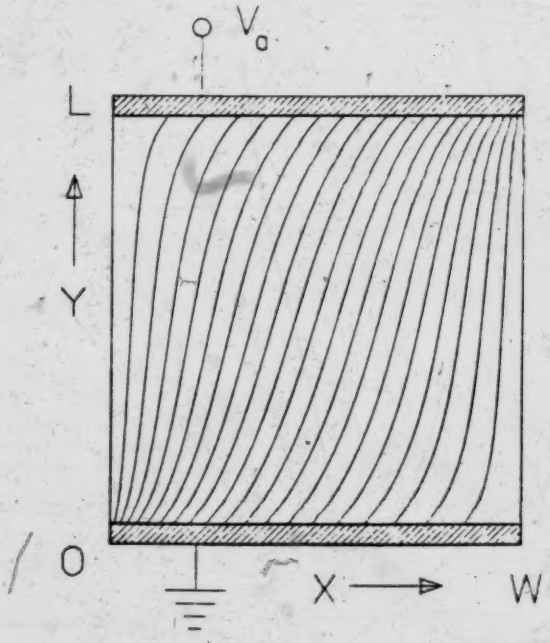

Fig. 4. Current lines correpsonding to Fig. 3.

RESULTS

We computed the electric potential and the current density in a square silicon slab with ohmic contacts for magnetic fields up to 10 Tesla, and with a doping level of $10^{16}cm^{-3}$ for both p and n type material.

Figures 1-4 show plots of the equipotential curves and the current lines. Under the conditions that apply to our computations, magnetoconcentration is found to be insignificant. Consequently, we did not make plots of the carrier densities. Also, our results depend very little on the linear dimensions of the square slab.

Due to the boundary conditions, equipotential lines close to the metal have to be parallel to the boundary. Thus carriers are deflected in this area. Close to the open boundary, however, current lines are parallel to the boundary; a Hall electric field is built up in this region.

Far from the boundaries, however, the operation of the device can be visualized neither in terms of Lorentz deflection nor Hall voltage; both of these mechanisms are involved in a complex way.

The deviation of our results from the limit $W/L \to 0$ (Vinal's case [7]) is demonstrated by the variation of the electric field component ratio E_x/E_y (see Figs. 5-6) across the device. In the limit $W/L \to 0$ this ratio is a constant.

DISCUSSION

To the best of our knowledge, we are presenting the first two-dimensional modeling of a magnetic-field-sensitive semiconductor device. Our results show the important point that the two-dimensional distributions of current density and potential cannot be easily described in terms of simple models such as Hall voltage or Lorentz deflection; this is due to the intricate combination of the magnetic field and the boundary conditions.

Thus our results lead to an accurate prediction of the Hall voltage even under extreme conditions in terms of the geometries and the magnetic fields such that the Hall voltage is a nonlinear function of the magnetic field strength.

Further work concerning magnetic field sensors that comprise intrinsic semiconductor materials and p-n junctions is in progress.

ACKNOWLEDGEMENTS

This work has been supported by grants from the Natural Sciences and Engineering Research Council of Canada (NSERC). We would like to thank Drs. W.S. Young and A.M.J. Huiser for helpful discussions.

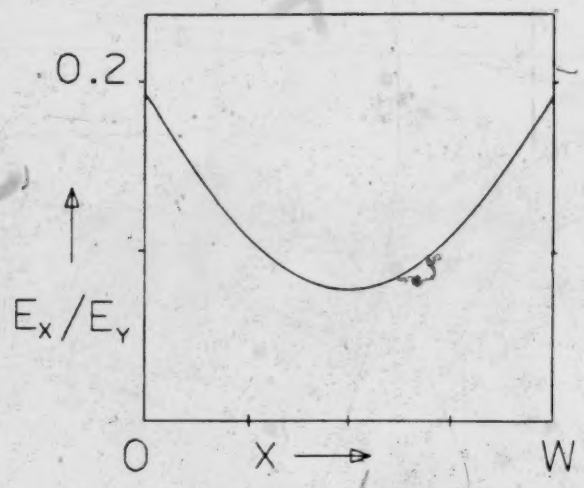

Fig. 5. Electric field ratio Ex/Ey across the middle (y = L/2) of device corresponding to Fig. 1.

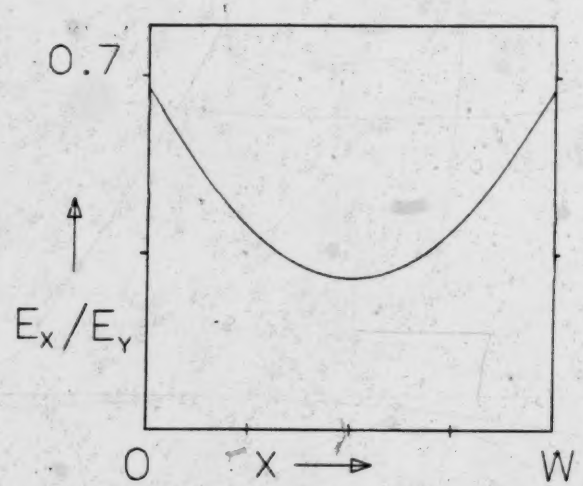

Fig. 6. Electric field ratio Ex/Ey across the middle (y = L/2) of device corresponding to Fig. 3.

REFERENCES

[1] H. Pfleiderer, "Magnetodiode model", *Solid State Electronics*, vol. 15, pp. 335-353, 1972.

[2] M. Kurata, *Numerical Analysis for Semiconductor Devices*. Lexington Mass.: Heath, 1982.

[3] H.H. Heimeier, "A two-dimensional numerical analysis of a silicon N-P-N transistor", *IEEE Trans. Electron. Devices*, vol. ED-20, pp. 708-714, 1973.

[4] S.M. Sze, *Physics of Semiconductor Devices*, 2nd ed., New York: Wiley, 1981, p. 34.

[5] W.L. Engl, H.K. Dirks, and B. Meinerzhagen, "Device Modelling", *Proc. IEEE*, vol. 71, pp. 10-33, 1983.

[6] M. Rudan and R. Guerrieri, "Relevant problems in the numerical simulation of semiconductor devices using the finite element method", in: *Numerical Analysis of Semiconductor Devices and Integrated Circuits*, ed. by J.J.H. Miller, Boole Press, Dublin, 1983.

[7] A.W. Vinal and N.A. Masnari, "PN junction injection modulated magnetic sensors (JIMMS)", in: *Solid State Transducers 83*, Program and Abstracts of 2nd Int. Conf. on Solid-State Sensors and Actuators, May 31 - June 3, 1983, Delft, The Netherlands, ed. by Dept. of Electrical Engineering, Delft University of Technology, 1983, p. 117.

APPENDIX E

Two-Dimensional Numerical Analysis of a Silicon Magnetic Field Sensor

H. P. BALTES, L. ANDOR, A. NATHAN, AND H. G. SCHMIDT-WEINMAR

Abstract—We present two-dimensional numerical solutions of the coupled, nonlinear, partial differential equations governing the electric potential, carrier drift, diffusion, generation, and recombination in a finite semiconductor slab in the presence of a magnetic field. This enables device modeling for general geometries, doping levels, and injection conditions, where the effect of the magnetic field cannot be expressed simply in terms of Hall voltage, Lorentz deflection, or magnetoconcentration.

INTRODUCTION

Currently, we see rapid growth in the area of magnetic-field-sensitive silicon microtransducers (see, e.g., [1]–[4] and references therein). The theoretical understanding of the electronic mechanisms underlying these devices, let alone device modeling, has not kept up with this rapid growth. This situation eventually has led to some dispute [5], [6].

Device modeling in the absence of a magnetic field is a highly developed area of research. Many devices can only be modeled by numerical solution of the well-known nonlinear system of partial differential equations comprising the continuity equations and Poisson's equation [7]–[10].

In the presence of a magnetic field, the numerical modeling of semiconductor devices is even more required for the following reasons:

i) In the bulk, the magnetic field causes a sequence of effects to take place: changes of the carrier motion, the carrier distributions, and the electrostatic potential. Only in certain limits the action of the field can be visualized simply in terms of, e.g., Hall voltage or carrier deflection.

ii) Any realistic device modeling has to account for the boundary conditions, such as "ohmic" or "oxide" contacts [10]. The magnetic field introduces some asymmetry into the current equations, while the boundary geometry retains any zero-field symmetry; this makes the problem even more difficult.

Manuscript received December 1, 1983. This work has been supported by grants from the Natural Sciences and Engineering Research Council of Canada (NSERC).

H. P. Baltes, A. Nathan, and H. G. Schmidt-Weinmar are with the Department of Electrical Engineering, University of Alberta, Edmonton, Alta., Canada T6G 2E1.

L. Andor is with the Department of Electrical Engineering, University of Alberta, currently on leave from the Research Institute for Technical Physics of the Hungarian Academy of Sciences, Budapest, 1, H-1440, Hungary.

BASIC EQUATIONS

Because of the Lorentz force, the current equations in a semiconductor, in the presence of a magnetic field read as follows [11]:

$$\vec{J}_n = \frac{1}{1+(\mu_n^*\vec{B})^2}\left[(q\mu_n n\vec{E} + qD_n\vec{\nabla}n) + \mu_n^*\vec{B}\times(q\mu_n n\vec{E} + qD_n\vec{\nabla}n)\right] \tag{1}$$

$$\vec{J}_p = \frac{1}{1+(\mu_p^*\vec{B})^2}\left[(q\mu_p p\vec{E} - qD_p\vec{\nabla}p) - \mu_p^*\vec{B}\times(q\mu_p p\vec{E} - qD_p\vec{\nabla}p)\right]. \tag{2}$$

Here, $\vec{B}$ is the magnetic induction, $\vec{J}_n$ and $\vec{J}_p$ denote the electron and hole current densities, μ_n and μ_p the drift mobilities, μ_n^* and μ_p^* the Hall mobilities, n and p the electron and hole concentrations, D_n and D_p the diffusion coefficients, q denotes the elementary charge, $\vec{E}$ the electric field, and $\vec{\nabla}$ the nabla operator. The continuity equations (stationary case) and Poisson's equation are as usual, viz.,

$$\frac{1}{q}\vec{\nabla}\cdot\vec{J}_n - R = 0 \tag{3}$$

$$-\frac{1}{q}\vec{\nabla}\cdot\vec{J}_p - R = 0 \tag{4}$$

$$(\vec{\nabla})^2\,\psi = -\frac{q}{\epsilon}(p - n + N). \tag{5}$$

By R we denote the net bulk recombination rate, N the net doping density, ϵ the dielectric constant, and ψ the electrostatic potential. For R, we use the Schockley–Read–Hall model, viz.,

$$R = \frac{(pn - n_i^2)}{\tau_n\left[p + n_i\exp\left(\frac{E_i - E_t}{kT}\right)\right] + \tau_p\left[n + n_i\exp\left(\frac{E_t - E_i}{kT}\right)\right]}. \tag{6}$$

Here τ_n and τ_p are the bulk carrier lifetimes, E_t is the energy level of trap centers, E_i the intrinsic Fermi level, k is the Boltzmann's constant, T the absolute temperature, and n_i denotes the intrinsic concentration. Following common practice [7], in our computations we assumed $E_t = E_i$.

Equations (1) to (6) constitute the system to be solved subject to appropriate boundary conditions. In this brief, we discuss only a rectangular semiconductor slab with the magnetic field perpendicular to the device surface, $\vec{B} = (0, 0, B_z)$, as shown in Fig. 1; then all distributions in the device depend only on x and y.

For the mobilities we used [12]

$$\mu_n = \left(65.0 + \frac{1265}{1 + [N_T/(8.5 \times 10^{16}\ \text{cm}^{-3})]^{0.72}}\right)\frac{\text{cm}^2}{\text{V}\cdot\text{s}} \quad (7)$$

$$\mu_p = \left(47.7 + \frac{447.3}{1 + [N_T/(6.3 \times 10^{16}\ \text{cm}^{-3})]^{0.76}}\right)\frac{\text{cm}^2}{\text{V}\cdot\text{s}} \quad (8)$$

where N_T denotes the total impurity concentration. For the Hall mobility, we used the relation, $\mu^* = r\mu$ where we adopted for r the value 1.92 [13].

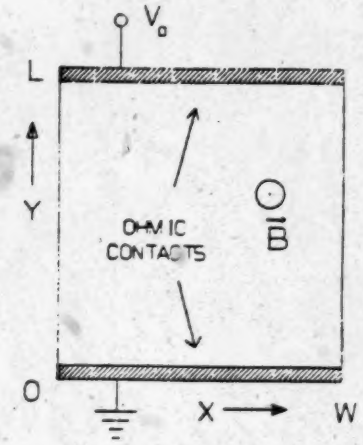

Fig. 1. Basic device geometry: semiconductor slab of length L and width W, with a magnetic field $\vec{B}$ perpendicular to the drawing plane. The applied voltage is V_a.

Boundary Conditions

We take ohmic contacts on two opposite faces of the device, as shown in Fig. 1. Along these contact boundaries, we assume [7], [9]

$$pn = n_i^2. \quad (9)$$

Moreover, charge neutrality leads to the condition [7], [9]

$$\psi = V_a + \frac{kT}{q}\sinh^{-1}\left(\frac{N}{2n_i}\right) \quad (10)$$

for the potential ψ. Here, V_a denotes the applied voltage and kT/q equals 25.7 mV at room temperature.

Along the other, "floating boundaries," we maintained the current conditions [7], [9]

$$J_{nx} = 0 \quad (11a)$$

$$J_{px} = 0. \quad (11b)$$

Computing the boundary conditions (11), we used (1) and (2) which contain the magnetic field.

As for the space charge condition along the floating boundary, we have adopted the condition

$$\frac{\partial^2}{\partial x^2}(p - n + N) = 0. \quad (12)$$

Equation (12) is less restrictive than the condition of zero space charge variation proposed by Kurata [9]. The choice of (12) was required because of the asymmetry introduced to our problem by the magnetic field.

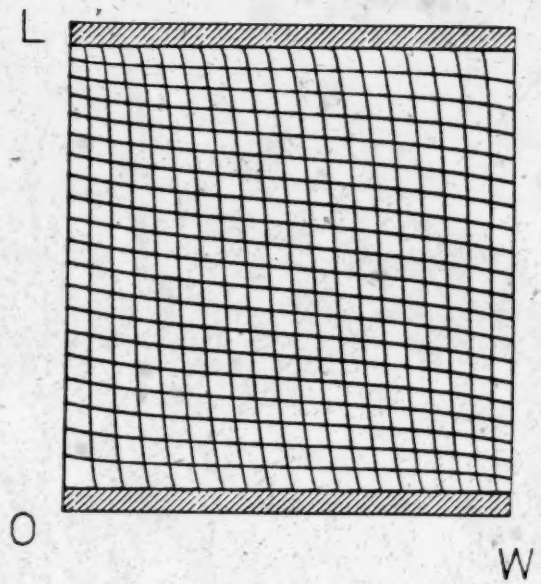

Fig. 2. Equipotential lines and current lines for a square device, $L = W = 100\ \mu\text{m}$, n-type silicon, doping level $10^{16}\ \text{cm}^{-3}$, $B_z = 1$ T.

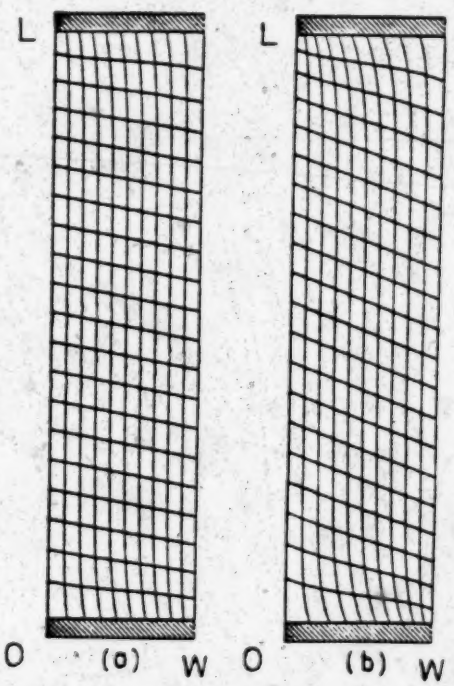

Fig. 3. (a) Same as Fig. 2, but $L = 4W$, $B_z = 1$ T. (b) Same as Fig. 2, but $L = 4W$, $B_z = 2$ T.

Numerical Procedure

We have set up (1)–(12) in finite difference form following the technique of [9] and [12]. Moreover, for the continuity equations (3) and (4), which include the field $\vec{B}$ through (1) and (2), we have used a discretization technique similar to the generalization of the Scharfetter–Gummel scheme discussed recently by Rudan and Guerrieri [14].

Our iteration procedure is based on i) the linearization of the equations by applying Newton's iteration principle, and ii) the simultaneous solution of Poisson's and the continuity equations ("full coupling") [9].

Results

To demonstrate the dependence of the solutions of the device geometry, we computed the electric potential and the current density for a variety of ratios W/L of width to length of the semiconductor slab. As an example, we chose n-type silicon with a doping level 10^{16} cm^{-3}; the magnetic field varied from 0 to 2 T; the applied voltage V_a was 0.1 V.

Plots of the equipotential lines and current lines are shown for $W/L = 1$ (Fig. 2), $W/L = \frac{1}{4}$ (Fig. 3), and $W/L = 4$ (Fig. 4(a)). The results strongly depend on the ratio W/L, but depend very little on the absolute values of W or L, provided these linear dimensions are not too small (larger than say, 1 μm).

In the long-slab limit ($W \ll L$, see Fig. 3), our results resemble those of Vinal's magnetic-field-sensor model [15], [16], i.e., there is a constant Hall field E_x, and the current lines are parallel to the slab boundaries, except for regions close to the ohmic contacts. In the opposite limit of a short device with broad contacts ($W \gg L$, see Fig. 4(a)) carrier deflection prevails in most of the device area, viz., there are horizontal equipotential lines and skew current lines showing the usual Hall angle, as discussed by Zieren [17].

In the general case between these extremes (e.g., the square-shaped device, see Fig. 2), the operation of the device can be visualized neither in terms of Lorentz deflection nor Hall voltage; both these mechanisms are involved in a complex way. It turns out that magnetoconcentration is insignificant under the circumstances considered in this paper. However, we found magnetoconcentration to be significant in other cases, e.g., under intrinsic conditions.

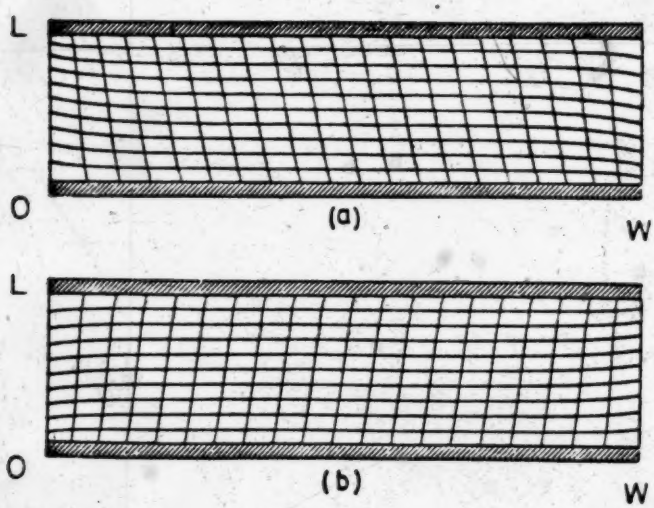

Fig. 4. (a) Same as Fig. 2, but $L = W/4$, $B_z = 1$ T. (b) Equipotential lines and current lines for a p-type silicon device, doping level 10^{16} cm^{-3}, $L = W/4$, $B_z = 2$ T.

The deviation from, say, Vinal's limit $W/L \to 0$, can be demonstrated in terms of the electric field component ratio E_x/E_y or the current deflection J_x/J_y across the device. We note that both ratios E_x/E_y and J_x/J_y have the maximum value of tan $\Theta_H = \mu_n^* B_z$ where Θ_H is the Hall angle (see Figs. 5 and 6).

We have furthermore computed the case of p-type silicon with 10^{16} cm^{-3} doping level for fields up to 5 T. Analogous results are obtained; the magnetic field effects are somewhat weaker because of the lower Hall mobility for holes (see Fig. 4(b)).

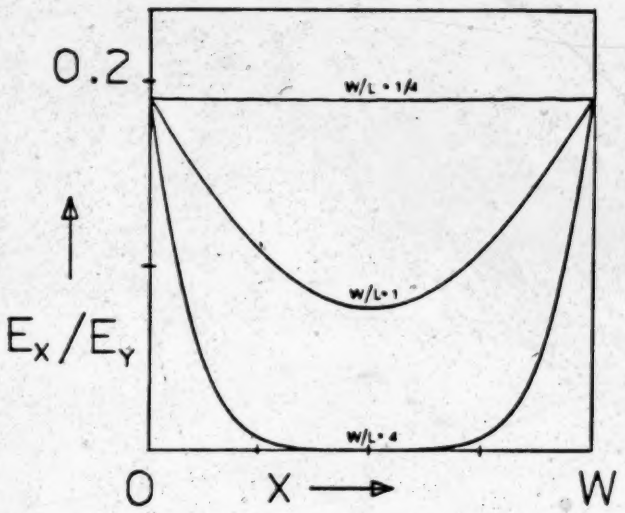

Fig. 5. Electric field component ratio E_x/E_y across the middle ($y = L/2$) of the device corresponding to Figs. 2, 3(a), and 4(a).

Discussion

To the best of our knowledge, in this brief we are reporting the first numerical modeling of a magnetic-field-sensitive semiconductor device. We have used standard methods [7]–[10], [12], [14] appropriately adapted to the problem with exterior magnetic field. The crucial point in modeling such a device is the intricate combination of the magnetic field and the boundary conditions; this may result in the failure of simpler analytical models based solely on, e.g., the Hall effect or the Lorentz deflection to describe these devices.

Our present iteration converges for not too large products of B_z and Hall mobility, say tan $\Theta_H < 0.3$. For all numerical computations reported in this brief, the use of a uniform grid was found to be sufficient. Work is in progress concerning devices in the presence of an exterior magnetic field under intrinsic conditions.

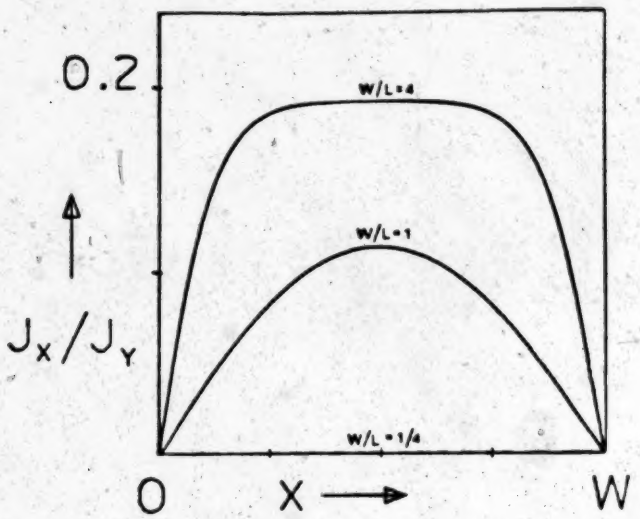

Fig. 6. Current deflection J_x/J_y across the middle ($y = L/2$) of the device corresponding to Figs. 2, 3(a), and 4(a).

ACKNOWLEDGMENT

The authors would like to thank Dr. W. S. Young and Dr. A. M. J. Huiser for helpful discussions.

REFERENCES

[1] V. Zieren and B. P. M. Duyndam, "Magnetic-field-sensitive multicollector n-p-n transistor," *IEEE Trans. Electron Devices*, vol. ED-29, pp. 83-90, 1982.

[2] A. W. Vinal and N. A. Masnari, "Magnetic transistor behaviour explained by modulation of emitter injection, not carrier deflection," *IEEE Electron Device Lett.*, vol. EDL-3, pp. 203-205, 1982.

[3] R. S. Popović and H. P. Baltes, "An investigation of the sensitivity of the magnetotransistors," *IEEE Electron Device Lett.*, vol. EDL-4, pp. 51-53, 1983.

[4] R. S. Popovic, H. P. Baltes, and F. Rudolf, "An integrated silicon magnetodiode," *IEEE Electron Devices*, in press.

[5] V. Zieren, S. Kordić, and S. Middelhoek, "Comment on magnetic transistor behaviour explained by modulation of emitter injection, not carrier deflection," *IEEE Electron Device Lett.*, vol. EDL-3, pp. 394-395, 1982.

[6] A. W. Vinal and N. A. Masnari, "Response to "Comment on 'Magnetic transistor behavior explained by modulation of emitter injection, not carrier deflection,'" " *IEEE Electron Device Lett.*, vol. EDL-3, pp. 396-397, 1982.

[7] W. L. Engl, H. K. Dirks, and B. Meinerzhagen, "Device modelling," *Proc. IEEE*, vol. 71, pp. 10-33, 1983.

[8] Proc. NASECODE III (Galway), June 1983, *Numerical Analysis of Semiconductor Devices and Integrated Circuits*, J. J. H. Miller, ed. Dublin: Boole, in press.

[9] M. Kurata, *Numerical Analysis for Semiconductor Devices*. Lexington MA: Heath,, 1982.

[10] M. S. Mock, *Analysis of Mathematical Models of Semiconductor Devices*. Dublin: Boole, 1983.

[11] H. Pfleiderer, "Magnetodiode model," *Solid-State Electron.*, vol. 15, pp. 335-353, 1972.

[12] H. H. Heimeier, "A two-dimensional numerical analysis of a silicon n-p-n transistor," *IEEE Trans. Electron Devices*, vol. ED-20, pp. 708-714, 1973.

[13] S. M. Sze, *Physics of Semiconductor Devices*, 2nd ed. New York: Wiley, 1981, p. 34.

[14] M. Rudan and R. Guerrieri, "Relevant problems in the numerical simulation of semiconductor devices using the finite element method," in: *Numerical Analysis of Semiconductor Devices and Integrated Circuits*, J. J. H. Miller, Ed. Dublin: Boole, 1983.

[15] A. W. Vinal and N. A. Masnari, "PN junction injection modulated magnetic sensors (JIMMS)," in: *Solid State Transducers 83*, Program and Abstracts of 2nd Int. Conf. on Solid-State Sensors and Actuators (Delft, The Netherlands), May 31-June 3, 1983. ed. by Dept. of Electrical Engineering, Delft University of Technology, 1983, p. 117.

[16] A. W. Vinal, private communication.

[17] V. Zieren, "Integrated silicon multicollector magnetotransistors," Ph.D. dissertation, Delft Technical University, 1983, pp. 26-28.

APPENDIX F

NUMERICAL MODELING OF SILICON MAGNETIC FIELD SENSORS: MAGNETOCONCENTRATION EFFECTS IN SPLIT-METAL-CONTACT DEVICES

H.G. Schmidt-Weinmar, L. Andor*, H.P. Baltes and A. Nathan
Department of Electrical Engineering
University of Alberta, Edmonton, Alberta, Canada T6G 2E1

Abstract: The two-dimensional distributions of the electric potential, the electron concentration and the hole concentration in a silicon slab exposed to a magnetic field have been computed numerically. Generalizing the well-known Scharfetter-Gummel scheme to the case of two dimensions and nonzero magnetic field, we have employed a finite-difference technique. In case of Hall plates, where space charge is negligible, our results are in support of previous results obtained by analytical models or by conformal-mapping technique. In intrinsic or closely intrinsic silicon, our results show both magnetoconcentration and space-charge effects; these can be exploited in the design of split-metal-contact magnetic field sensors.

Introduction

A large number of new magnetic-field-sensitive silicon devices have been realized recently (see [1] and references therein). The theoretical understanding of the electronic mechanisms underlying these devices, let alone device modeling, has not kept pace with this rapid growth. This situation has eventually led to some dispute [1].

Numerical semiconductor device modeling, a well-established art for zero magnetic field, is even more desirable for magnetic sensors;

> The basic magnetic effects (Hall voltage, Lorentz deflection, magnetoconcentration) are two-dimensional and cannot be simply superimposed to describe the device. Moreover, the role of the boundary conditions is crucial, since the magnetic-field effects are particularly strong close to the device boundaries.

The problem in question is made more difficult by the fact that the magnetic field breaks some of the symmetries exploited in the modeling of zero-field semiconductor devices. Apart from some early work in terms of the Hall plate model [2], numerical results on silicon magnetic field sensors have become available only recently [1]. While our previous note emphasizes geometrical aspects of semiconductor slabs with metal contacts in a magnetic field, this paper presents new results, focused on the magnetoconcentration effect and split-contact (current imbalance) applications. For a full presentation of the underlying numerical methods we refer to [3].

Equations and Boundary Conditions

In a stationary magnetic field, the continuity equations for electrons and holes and the Poisson equation are

$$\frac{\partial n}{\partial t} - \frac{1}{q}\vec{\nabla}\cdot\vec{J}_n + R = 0 \qquad (1)$$

$$\frac{\partial p}{\partial t} + \frac{1}{q}\vec{\nabla}\cdot\vec{J}_p + R = 0 \qquad (2)$$

$$\nabla^2\psi = \frac{q}{\varepsilon}(p - n + N). \qquad (3)$$

Here n and p are the electron and hole concentrations, ψ is the electric potential, $\vec{J}_n$ and $\vec{J}_p$ are the electron and hole current densities, q is the elementary charge, ε is the dielectric constant, R is the net bulk recombination rate and N the ionized net doping.

When the magnetic field is perpendicular to the current densities, the transport equations read [4].

$$\vec{J}_n = \frac{1}{1 + (\mu_n^* \vec{B})^2}\left[(q\mu_n n\vec{E} + qD_n\vec{\nabla}n) + \mu_n^*\vec{B}\times(q\mu_n n\vec{E} + qD_n\vec{\nabla}n)\right], \qquad (4)$$

$$\vec{J}_p = \frac{1}{1 + (\mu_p^* \vec{B})^2}\left[(q\mu_p p\vec{E} - qD_p\vec{\nabla}p) - \mu_p^*\vec{B}\times(q\mu_p p\vec{E} - qD_p\vec{\nabla}p)\right]. \qquad (5)$$

Here, $\vec{B}$ is the magnetic induction, μ_n and μ_p are the drift mobilities, μ_n^* and μ_p^* the Hall mobilities, D_n and D_p the diffusion coefficients.

For the bulk recombination rate we use the Schockley-Read-Hall model [5], [6]. For the drift mobilities we use well-known empirical expressions [7]. For the Hall mobilities we use the approximation [8] $\mu^* = r\mu$, with r given the value 1.92 [9].

In this paper, we consider semiconductor slabs of rectangular geometry with a magnetic field perpendicular to the device surface: $\vec{B} = (0, 0, B_z)$ (see Fig. 1). Then the distributions of carriers and potential in the device depend only on x and y; we solve a two-dimensional problem.

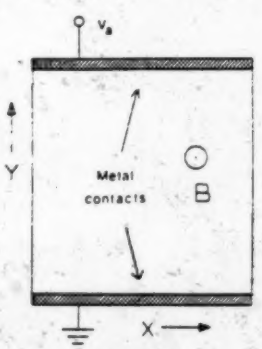

Fig. 1 Device geometry: semiconductor slab with a magnetic field $\vec{B}$ perpendicular to the drawing plane. The applied voltage is V_a.

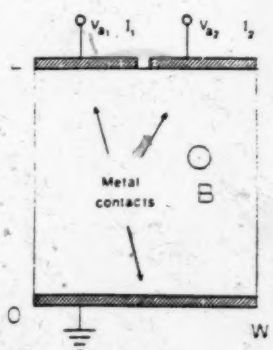

Fig. 2 Geometry of a silicon magnetic field sensor with a split-metal contact. W and L denote the device width and length respectively.

We assume metal contacts on two opposite faces of the device as shown in Fig. 1. Along these "fixed" boundaries, the values of n, p, and ψ are given by infinite recombination rate (6), charge neutrality (7), and the applied voltage V_a (8)

*Currently on leave from the Research Institute for Technical Physics of the Hungarian Academy of Sciences, Budapest 1, P.O.B. 76, H-1140 Hungary.

[5], [6]. Using $(kT/q) = D_n/\mu_n$, we write

$$p \cdot n = n_i^2 \tag{6}$$

$$p - n + N = 0 \tag{7}$$

$$\psi = V_a + \frac{kT}{q} \sinh^{-1}\left(\frac{N}{2n_i}\right). \tag{8}$$

Along the other, insulated "floating" boundaries we maintain the usual zero-normal-current-density conditions (see Fig. 1)

$$J_{nx} = 0 \tag{9}$$

$$J_{px} = 0. \tag{10}$$

For the third condition required along the floating boundaries, we use

$$\frac{\partial^2}{\partial x^2}(p - n + N) = 0. \tag{11}$$

While this condition is weaker than the conditions commonly used at floating boundaries, it still ensures that the space charge is a smooth function of the spatial coordinates.

Numerical Procedure

The partial differential equations (1) - (5) and the boundary conditions (6) - (11) were discretized for obtaining numerical solutions. In view of the rectangular geometry of our model devices we used for discretization the finite-difference technique [5] implemented on a non-uniform, rectangular grid. This technique, which allowed us to use the SLOR method [5], [10] achieves reasonably fast convergence even when the equations (1) - (5) were solved simultanously by a "coupled" [11] or "simultaneous" [5] algorithm.

After discretization, equations (1) - (5) were linearized by a Newton-iteration scheme [5]. The linear systems thus obtained were, however, in many cases of practical interest unsuited for an interative solution because of the numerical values the out-of-diagonal elements took on. We solved this problem [3] by generalizing the well-known Scharfetter-Gummel scheme [12] for the case of two-dimensions [11], [13] and nonzero magnetic field.

Using a grid with 50 x 50 nodes and working with double-precision arithmetic the computation of one solution required approximately 2 Mbytes of memory and 50 - 200 seconds of CPU time on our Amdahl 580 computer. For every Newton cycle, 15 - 30 SLOR iterations were implemented. For a relative precision of 10^{-4} typically 8 - 20 Newton cycles were required. In the SLOR iteration, we employed a relaxation factor between 0.1 and 1.9 depending on the device parameters and the initial guess value.

Results

Typical results obtained in silicon of various doping levels for the electric potential, the current density, the electron and hole concentrations are shown in Figs. 3-5. The effect of the device geometry has been presented elsewhere [1].

Fig. 3 and Fig. 5a show plots of equipotential and current lines. The effects of the boundary conditions on the equipotential and current lines can be described as follows:

(i) Close to the metal boundaries the equipotential lines are parallel to the boundaries.

(ii) Close to the open boundaries the current lines are parallel to the boundaries.

In the case of doped material, the results (see Fig. 3) agree well with those obtained earlier by the Hall-plate model [2], where the Poisson equation with zero space charge was solved. However, if the doping level is of the same order as the intrinsic concentration and if significant electric and magnetic fields are present, then the space charge cannot be neglected and the Hall-plate model does not apply. For example, Fig. 4 shows the computed space-charge distribution in a 4 μm x 4 μm n-type silicon slab, where a close-to-intrinsic condition is modeled by an assumed elevated temperature of 500°K.

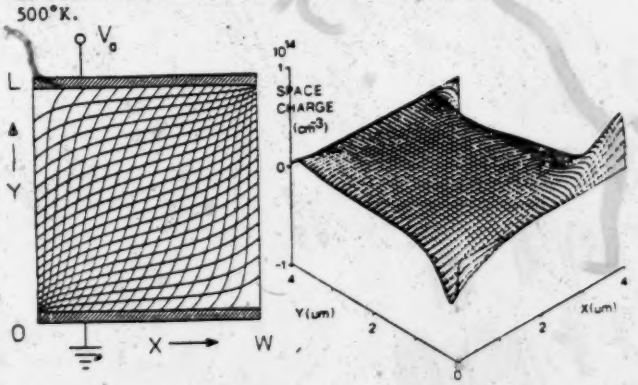

Fig. 3 Equipotential lines and current lines for a square device; L = W = 100 μm, p-type silicon, doping level 10^{16} cm^{-3}, B_z = 10 Tesla.

Fig. 4 Space charge distribution for a square device; L = W = 4 μm, n-type silicon, doping level 10^{15} cm^{-3}, B_z = 1 Tesla, T = 500°K.

In intrinsic material, where the net doping is much smaller than the intrinsic concentration, both electron and hole concentrations are strongly affected by the magnetoconcentration effect (see Figs. 5b and 5d). This results in an almost exponential increase of the concentrations in x direction along the middle of the slab. On the other hand, the metal boundaries impose a strong concentration gradient in the y direction on both electrons and holes. The interaction of magneto-concentration and boundary effects gives rise to the unexpected space-charge distribution shown in Fig. 5c. We note that in the intrinsic case the scaling rule breaks down, because the space charge depends on the local concentration gradients.

In Fig. 5a, the equipotential lines show only small Hall-field components, while the current lines crowd on the high-concentration side of the device. This result suggests that a device with split-metal contacts, as shown in Fig. 2, could be employed to measure a magnetic field. The sensitivity of such split-metal-contact devices can be defined by the relative current imbalance, viz. $S = (I_1 - I_2) / (I_1 + I_2)$. Table 1 shows the sensitivities computed for different doping levels and geometries. The intrinsic split-metal-contact device yields the highest sensitivity of all the ones we have modeled. This intrinsic device, however, is rather sensitive to size reduction;

a 4 μm x 4 μm split-metal-contact device would yield less than half of the sensitivity of a 100 μm x 100 μm device. This is the consequence of the building up of space charge mentioned earlier (see Fig. 5c), which acts against the magnetoconcentration effect and modifies the current density and potential distributions.

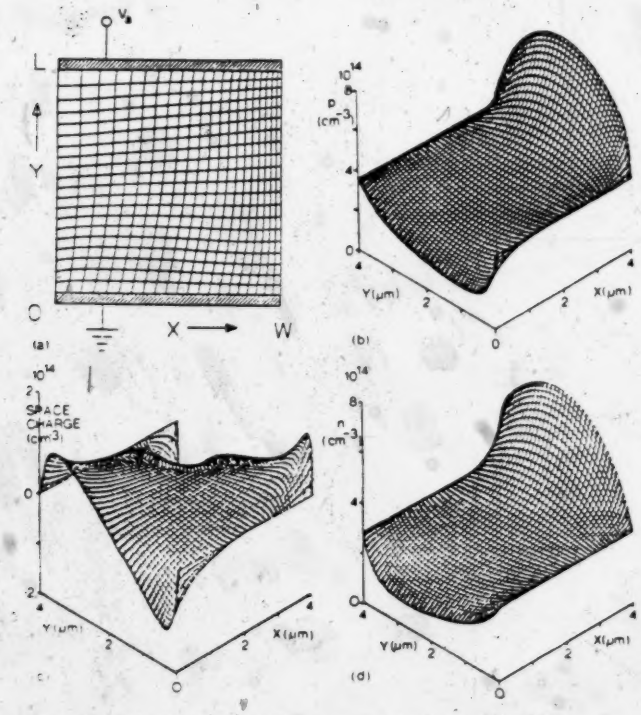

Fig. 5 Intrinsic silicon square device; L = W = 4 μm, B_z = 1 Tesla, T = 500°K. a) Equipotential lines and current lines. b) Hole concentration. c) Space-charge distribution. d) Electron concentration.

Type	L x W	$\frac{I_1-I_2}{I_1+I_2}$
Intrinsic	100 μm x 100 μm	0.443
Intrinsic	4 μm x 4 μm	0.338
n	100 μm x 100 μm	0.093
n	400 μm x 100 μm	0.101
n	100 μm x 400 μm	0.033
$n = 10^{16} cm^{-3}$	V_{a1} = 1.0 Volt	
B = 1 Tesla	V_{a2} = 1.0 Volt	

Table 1 Magnetic Sensitivity $(I_1-I_2)/(I_1+I_2)$ of silicon slabs of various dopings and geometries (see Fig. 2).

Discussion and Outlook

A semiconductor device exposed to a magnetic field has been modeled numerically. The asymmetries introduced by the magnetic field into the transport equations and the boundary conditions have been incorporated successfully into a computer algorithm by a generalization of the well-known Scharfetter-Gummel scheme to two dimensions and nonzero magnetic field; depending on the initial guess our computations may require only up to one third more CPU-time than the case of zero magnetic field.

In case of Hall plates, our results agree with prior results obtained by simple analytical models or conformal mapping technique. However, when magnetoconcentration and space-charge effects occur simultaneously, only numerical modeling will describe the functioning of the device. We have modeled devices with split-metal contacts which show promising sensitivities; our device principle has, however, to be explored further using more realistic ohmic contacts.

We plan to apply our numerical algorithm to magnetodiodes, magnetotransistors, and split-drain MOS magnetic field sensors. Modeling of more general directions of the magnetic field will, however, require three spatial dimensions. The questions of optimum sensitivity and signal-to-noise ratio will be studied for specific cases.

Acknowledgements

This work has been supported by grants from the Natural Sciences and Engineering Research Council of Canada (NSERC). We would like to thank Drs. W. Allegretto, A.M.J. Huiser and W.S. Young for helpful discussions.

References

[1] H.P. Baltes, L. Andor, A. Nathan, and H.G. Schmidt -Weinmar. IEEE Trans. on Electron Devices, in print.
[2] R.F. Wick. Journal of Applied Physics, vol. 25, pp. 741-756, 1954.
[3] L. Andor, H.P. Baltes, A. Nathan, and H.G. Schmidt -Weinmar - to be published.
[4] H. Pfleiderer. Solid State Electrinics, vol. 15, pp. 335-353, 1972.
[5] M. Kurata, *Numerical Analysis for Semiconductor Devices*. Lexington Mass.: Heath, 1982.
[6] W.L. Engl, H.K. Dirks, and B. Meinerzhagen. Proc. IEEE, vol. 7, pp. 10 - 33, 1983.
[7] H.H. Heimeier. IEEE Trans. on Electron Devices, vol. ED-20, pp. 708-714, 1973.
[8] R.A. Smith, *Semiconductors*, 2nd ed. New York: Cambridge University Press, 1978.
[9] S.M. Sze, *Physics of Semiconductor Devices* 2nd ed., New York: Wiley, 1981.
[10] R.S. Varga *Matrix Iterative Analysis*, Prentice- Hall, 1962.
[11] M. Rudan and R. Guerrieri. In: *Numerical Analysis of Semiconductor Devices and Integrated Circuits*, ed. by J.J.H Miller, Boole Press, Dublin, 1983.
[12] D.L. Scharfetter, and H.K. Gummel. IEEE Trans. on Electron Devices, ED-16, pp. 64. 1969.
[13] P.E. Cottrel, and E.M. Buturla. Proc. of NASECODE I Conf. pp. 31-64. 1979.

APPENDIX G

Matrix and Vector Elements for the Split-Drain MOSFET

The coefficients of the variable u associated with eqn. (4.31) for the bulk and eqns. (4.32) - (4.34) describing the floating boundaries of the split-drain MOSFET (see Figs. 4.3 - 4.5) are described in this appendix.

Associated with eqn. (4.30) are:

$$A_T(M, N) = \frac{2}{h_y(N-1)\left[h_y(N) + h_y(N-1)\right]},$$

$$B_T(M, N) = -\frac{2}{h_x(M)\, h_x(M-1)} - \frac{2}{h_y(N)\, h_y(N-1)},$$

$$C_T(M, N) = \frac{2}{h_y(N)\left[h_y(N) + h_y(N-1)\right]},$$

$$D_T(M, N) = \frac{2}{h_x(M-1)\left[h_x(M) + h_x(M-1)\right]},$$

$$E_T(M, N) = \frac{2}{h_x(M)\left[h_x(M) + h_x(M-1)\right]}$$

Eqn. (4.24) is discretised by a central difference scheme, i.e.,

$$\text{At } (1);\quad \frac{u(3, N) - u(1, N)}{h_x(1) + h_x(2)} = \mu_n^* B_z \frac{u(2, N+1) - u(2, N-1)}{h_y(N) + h_y(N-1)} \quad .$$

$$\text{At } (2);\quad \frac{u(XMAX, N) - u(XMAX-2, N)}{h_x(XMAX-1) + h_x(XMAX-2)} = \mu_n^* B_z \frac{u(XMAX-1, N+1) - u(XMAX-2)}{h_y(N) + h_y(N-1)} .$$

$$\text{Hence, at } (1);\quad G_T(2, N) = - \mu_n^* B_z \left[\frac{h_x(1) + h_x(2)}{h_y(N) + h_y(N-1)}\right] ,$$

$$H_T(2, N) = - G_T(2, N) ,$$

$$I_T(2, N) = 0 ,$$

$$\text{and } J_T(2, N) = 1 .$$

At the floating boundary (2);

$$G_T(XMAX-1, N) = \mu_n^* B_z \left[\frac{h_x(XMAX-1) + h_x(XMAX-2)}{h_y(N) + h_y(N-1)}\right] ,$$

$$H_T(XMAX-1, N) = - G_T(XMAX-1, N) ,$$

$$I_T(XMAX-1, N) = 0 \quad \text{and} \quad J_T(XMAX-1, N) = 1 .$$

At the floating boundary (3) ;

Using central differencing on eqn. (4.23);

$$\frac{u(M+1,\ YMAX-1) - u(M-1,\ YMAX-1)}{h_x(M-1) + h_x(M)}$$

$$= - \frac{1}{\mu_n^* B_z} \cdot \left[\frac{u(M,\ YMAX) - u(M,\ YMAX-2)}{h_y(YMAX-1) + h_y(YMAX-2)} \right].$$

This yields the coefficients;

$$P_T(M,\ YMAX-1) = - \mu_n^* B_z \left[\frac{h_y(YMAX-1) + h_y(YMAX-2)}{h_x(M) + h_x(M-1)} \right],$$

$$Q_T(M,\ YMAX-1) = - P_T(M,\ YMAX-1) ,$$

$$R_T(M,\ YMAX-1) = 0 \quad \text{and} \quad S_T(M,\ YMAX-1) = 1 .$$

APPENDIX H

TWO - DIMENSIONAL MODELING OF A MOS MAGNETIC FIELD SENSOR

A. NATHAN, STUDENT MEMBER, IEEE, L. ANDOR,
H. P. BALTES, MEMBER, IEEE and H. G. SCHMIDT-WEINMAR

Abstract - We present numerical results for the potential, current and surface charge distributions as well as the sensitivity of a magnetic-field-sensitive split-drain N-channel MOSFET operating in the linear region. We also present a suitable circuit configuration that incorporates this device and calculate the overall sensitivity of the resulting magnetic-field-sensitive circuit. Optimisation of the device geometry is discussed.

I. INTRODUCTION

A number of MOS magnetic field sensors(MFS) based on the splitdrain configuration have been devised and realised recently (see [1] and references therein). To the best of our knowledge, no numerical modeling of such sensors has been reported hitherto.

In this note we present the first results of a two-dimensional numerical analysis of split-drain NMOS MFS operating in the linear region, the magnetic field vector being perpendicular to the device plane. Our numerical method allows to calculate the sensitivity of these MFS for a variety of device geometries, i.e. different aspect ratios and drain separations.

In contrast to the MFS described previously [1], our model applies to the linear region of MOSFET operation. Therefore, in this note, we also present a circuit configuration suitably matched to the split-drain NMOS device.

H. P. Baltes, A. Nathan, and H. G. Schmidt-Weinmar are with the Department of Electrical Engineering, University of Alberta, Edmonton, Alta., Canada T6G 2E1.

L. Andor is with the Department of Electrical Engineering, University of Alberta, currently on leave from the Research Institute for Technical Physics of the Hungarian Academy of Sciences, Budapest 1, PO Box 76, H-1440, Hungary.

II. THEORY

We analyse the channel region of an N-channel MOSFET in the linear region, subject to a magnetic field perpendicular to the device plane, $\vec{B} = (0,0,B_z)$. Following [2], the charge in the inversion layer is given by

$$Q_n(x,y) = C_{ox}\,[\,V(x,y) + 2\psi_B - V_G\,] + \sqrt{2cqN_A\,[\,V(x,y) + 2\psi_B\,]} \tag{1}$$

in the usual notation [2]. While the continuity equations and Poisson's equation remain the the same as for zero field [3], the current density has to be modified [4], to account for the Lorentz force, viz.,

$$\vec{J}_n = \frac{1}{1 + (\mu_n^* \vec{B})^2}\,[(q\mu_n n\vec{E} + qD_n\vec{\nabla}n) + \mu_n^*\vec{B} \times (q\mu_n n\vec{E} + qD_n\vec{\nabla}n)]\,, \tag{2}$$

in the usual notation [2]. The hole current and net recombination are assumed zero in the channel. A two-dimensional model is obtained by integrating the current density over the channel depth, viz.,

$$J_{nx}(x,y) = \frac{1}{1 + (\mu_n^* B_z)^2}\left[\left(-\mu_n \frac{\partial V}{\partial x} + D_n \frac{\partial}{\partial x}\right) + \mu_n^* B_z \left(-\mu_n \frac{\partial V}{\partial y} + D_n \frac{\partial}{\partial y}\right)\right] Q_n(x,y)\,, \tag{3}$$

$$J_{ny}(x,y) = \frac{1}{1 + (\mu_n^* B_z)^2}\left[\left(-\mu_n \frac{\partial V}{\partial y} + D_n \frac{\partial}{\partial y}\right) - \mu_n^* B_z \left(-\mu_n \frac{\partial V}{\partial x} + D_n \frac{\partial}{\partial x}\right)\right] Q_n(x,y)\,. \tag{4}$$

where V(x,y) denotes the reverse bias voltage between a point (x,y) in the channel and the source electrode (which is grounded). We use a field dependent drift mobility model proposed by [5]. Eqns. (3) and (4) are solved numerically using a finite difference discretisation scheme described elsewhere [6]. Since the device is operated in the linear region, we average the gate electric field over the channel length and assume a constant drain-source field.

We study the sensitivity of the split drain N-channel MOS MFS in terms of the relative current imbalance in the two drains, (see Fig. 1) viz.,

$$\delta = (I_{D1} - I_{D2})/(I_{D1} + I_{D2}) \qquad (5)$$

III. RESULTS and DISCUSSION

The current imbalance, δ of the split-drain MOSFET was computed for various aspect ratios W/L and drain separations, d (see Fig. 1). The MOSFET is operated in the linear region with $V_{D1S} = V_{D2S} = 1$ V, $V_{GS} = 5$ V and $V_S = 0$ V. The oxide thickness $t_{ox} = 100$ nm, bulk doping density, $N_A = 10^{15}$ cm^{-3} and threshold voltage, $V_T = 1$ V.

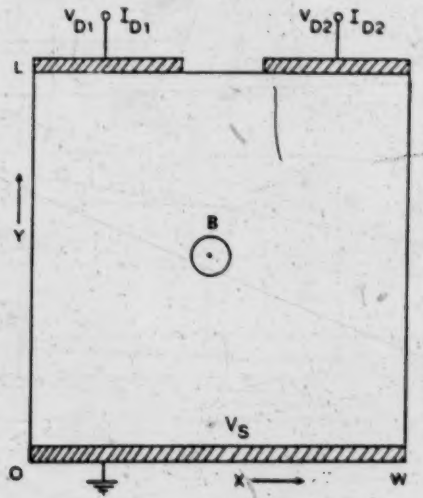

Fig. 1. MOSFET channel geometry

The case of the square device geometry with W = L = 25 μm is considered in Fig. 2 for the relative drain separations d/W = 0.05 (curve a), d/W = 0.2 (curve b) and d/W = 0.6 (curve c). The current imbalance, δ is a linear function of the flux density, B between -1 and +1 tesla, i.e. the sensitivity δ/B is constant. The linearity is not affected by the variation of d/W. For illustration, the distribution of potential, current and surface charge for the case d/W = 0.2 under 1 tesla field strength is shown in Fig. 3.

Fig. 2. Relative current imbalance, δ as a function of magnetic field, B for a square channel NMOS, W = L = 25 μm, for different relative drain separations (refer to text for curves a, b, and c)

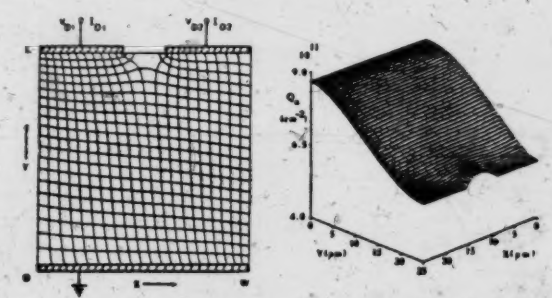

Fig. 3. (a) Equipotential and current lines (b) surface charge density of the NMOS MFS, W = L = 25 μm, d = 5 μm operated at $V_{D1S} = V_{D2S} = 1$ V, $V_{GS} = 5$ V and $V_S = 0$ V

The relative current imbalance δ for devices with aspect ratios W/L = 5 μm/25 μm and W/L = 100 μm/25 μm are shown in Figs. 4 and 5. The three relative drain separations are same as given in the previous paragraph.

We learn that narrowing the channel down from 25 μm to 5 μm (Fig. 4) leads to only a slight increase in sensitivity. Making the channel much broader (Fig. 5) results in a substantial sensitivity decrease.

For the W/L >> 1 geometry (Fig 5), we find a slight deviation

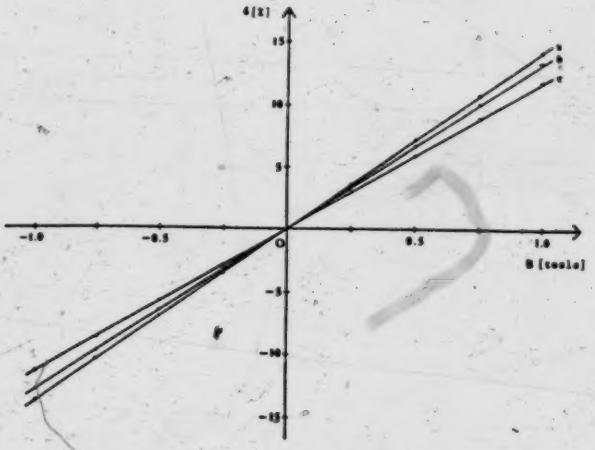

Fig. 4. Same as Fig. 2 but W/L = 5 μm/25 μm

from linear behaviour. This could possibly explain some of the non-linearity observed previously [1] for positive fields B ⩾ 0.7 tesla.

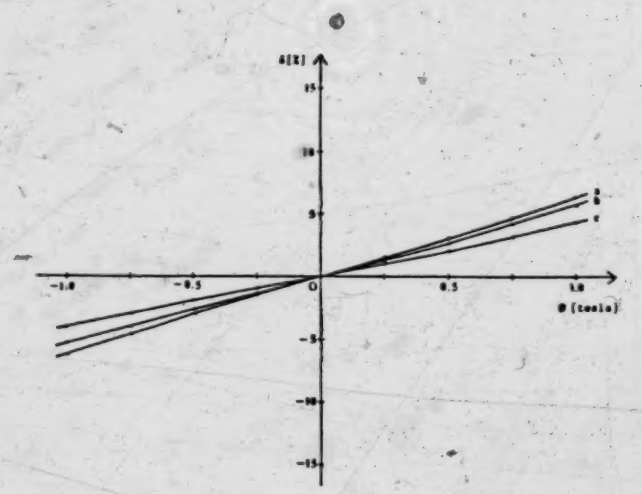

Fig. 5. Same as Fig. 2 but W/L = 100 μm/25 μm

From the point of view of keeping the device small, but allowing for the minimal drain separation required by the design rules the square geometry seems to be favourable.

IV. CIRCUIT DESCRIPTION

A circuit configuration matched to the square device (W = L = 25 μm, d = 5 μm) is shown in Fig. 6. The action of the Lorentz force leads to an increase of the current in one drain at the expense of the current in the other drain. The currents, I_{D1} , I_{D2} are

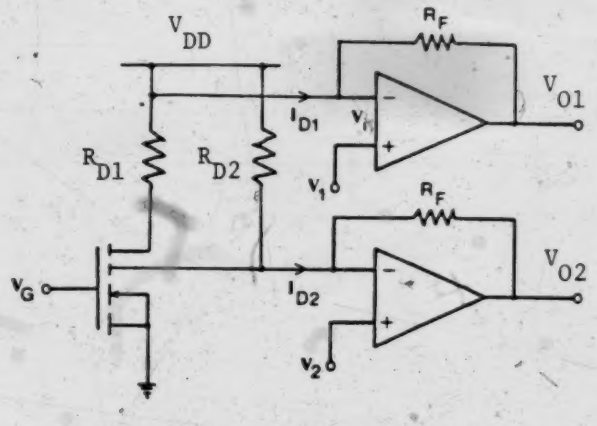

Fig. 6. Schemetic of the square channel device in circuit

converted into voltages, V_{O1} , V_{O2} by incorporating standard current to voltage convertors. The current to voltage convertors can be realised with inverting MOS operational amplifiers [7] using voltage shunt feedback. With reasonably high input impedance, R_i and high gain, A_v of the operational amplifiers, we have the amplifier inputs effectively shorted i.e. $V_1 \to 0$. Hence

$$V_{O1} - V_1 = - R_F I_{D1} \quad , \tag{6}$$

$$V_{O2} - V_2 = - R_F I_{D2} \quad . \tag{7}$$

Here, R_F denotes the feedback resistor (see Fig. 6). Moreover, any offsets at the amplifier inputs, $I_{D1} \neq I_{D2}$ with zero field, can be controlled by V_1 and V_2 . R_F is suitably chosen to match the input currents I_{D1} , I_{D2} and to meet the S/N ratio requirements.

Inserting (6) and (7) into (5), we finally obtain the overall sensitivity of the field sensitive circuit,

$$\bar{\delta}/B = \frac{(V_{O1} - V_{O2}) - (V_1 - V_2)}{(V_{O1} + V_{O2}) - (V_1 + V_2)} /B \tag{8}$$

The predicted sensitivity of the circuit considered above is $\bar{\delta}/B = 0.12$ /T. The drain currents I_{D1} , I_{D2} are 57 μA and 45 μA respectively.

To achieve the maximum attainable sensitivities, the drain voltages are put at the same potential in order to avoid any shunting effects between the drains and the device is operated at low gate voltages, e.g. $V_G \leq 5$ V.

V. CONCLUSION

In this note, we reported results of the first numerical modeling of magnetic-field-sensitive NMOS circuits. Our model allows to calculate the potential, current and surface charge distributions and the sensitivity for a variety of MOSFET geometries. In the case of P-channel MOSFET's, the mobilities μ_n and μ_n^* in eqns. (3) and (4) have to be replaced by μ_p and μ_p^*, respectively, etc.. Hence the sensitivity is reduced by a factor of μ_n/μ_p for an equivalent P-channel device in circuit. The device characteristics resulting from the above numerical analysis can be readily incorporated into a circuit simulation program such as SPICE for magnetic-field-sensitive circuit simulation.

ACKNOWLEDGEMENTS

This work has been supported by grants from the Natural Sciences and Engineering Research Council of Canada (NSERC). It is a pleasure to thank Drs. A. M. J. Huiser, I. Filanovsky and W. Allegretto for stimulating discussions.

REFERENCES

[1] R. S. Popovic and H. P. Baltes, "A CMOS Magnetic Field Sensor," *IEEE J. Solid-State Circuits*, vol. SC-18, pp. 426-428, 1983.

[2] S. M. Sze, *Physics of Semiconductor Devices*, 2nd ed., New York: Wiley, 1981.

[3] W. L. Engl, H. K. Dirks and B. Meinerzhagen, "Device Modeling," *Proc. IEEE*, vol. 71, pp.10-33, 1983.

[4] H. P. Baltes, L. Andor, A. Nathan and H. G. Schmidt-Weinmar, "Two-dimensional Numerical Analysis of a Silicon Magnetic Field Sensor," *IEEE Trans. Electron Devices*, vol. ED-18, 1984, in press.

[5] K. Yamaguchi, "Field-Dependent Mobility Model for Two-dimensional Numerical Analysis for MOSFET's," *IEEE Trans. Electron Devices*, vol. ED-26, pp.1068-1074, 1979.

[6] H. P. Baltes, L. Andor, A. Nathan and H. G. Schmidt-Weinmar, "Advances in Modeling Magnetic Semiconductor Devices," *Proc. MIEL-84*, May 7-9, Nis, Yugoslavia, 1984. A. Nathan, "*Numerical Analysis of MOS Magnetic Field Sensors*," M.Sc. Thesis, Department of Electrical Engineering, University of Alberta, 1984.

[7] P. R. Gray and R. G. Meyer, *Analysis and Design of Analog Integrated Circuits*, 2nd ed., New York: Wiley, pp.703-757, 1984.

APPENDIX I

Listing of Split-Drain MOSFET Simulation Program

```
      IMPLICIT REAL*8(A-H,L,O-Z)
      REAL*8 MUNH,MUN,MUNO,NA,NI
      REAL*8 S(50),SM(50),SP(50),SS(50),SSM(50),
     1       SSP(50),R(50),SR(50),SO(50),SSO(50),
     2       DSP(50),DSM(50),DSO(50),DS(50),DR(50),
     3       JN(50,50),QN(50,50),U(50,50),V(50,50)
      DIMENSION AT(50,50),BT(50,50),CT(50,50),DT(50,50),
     1       ET(50,50),FT(50,50),BTI(50,50),F(50),DBI(50,50)
      COMMON/KICSI/ UO(50,50),VO(50,50),H,NX,NX1,
     1       NY,NY1,HX(50),HY(50),NSD,NSDS,NSDE
      COMMON/MATR/ AT,BT,CT,DT,ET,FT
      COMMON/PREM/ DBI,BTI,S,SS,SM,SSM,SP,SSP,R,SR,SO,SSO,
     1             DSP,DSM,DSO,DS,DR
C
C     Q=ELEMENTARY CHARGE
C     CK=BOLTZMANN'S CONSTANT
C     EPS=PERMITIVITY OF FREE SPACE
C     RR=1.92 IS USED FOR HALL MOBILITY CALCULATIONS
C
      Q=1.6D-19
      CK=1.38D-23
      EPS=12.DO*8.86D-14
      EPSIO=3.9DO*8.86D-14
      RR=1.92DO
      PRINT34
C
C     NA=BULK DOPING DENSITY
C     H=MAGNETIC INDUCTION IN VOLT-SEC PER SQ. CM
C     W AND L ARE THE DEVICE DIMENSIONS(WIDTH AND LENGTH)
C     XWR=RELATIVE DRAIN SEPARATION(D/W)
C     NMC IS USED FOR TRIPLE-DRAIN DEVICE SIMULATIONS
C     TX AND TY ARE THE GRID SPACING RATIOS IN X AND Y
C     OMEGA=RELAXATION PARAMETER USED IN SLOR
C     VD, VS AND VG ARE DRAIN, SOURCE AND GATE VOLTAGES
C     ISLOR=MAX. NO. OF SLOR ITERATIONS
C     TOX=OXIDE THICKNESS
C     TT=TEMPERATURE
C     INGES=PARAMETER FOR EXTERNAL INITIAL GUESS
C
   34 FORMAT(' TYPE  NA,H,W,L,XWR,NMC,TX,TY,OMEGA,VD,VS,VG,'
     1       /'       ISOR,TOX,TT,INGES')
      READ*,NA,H,W,L,XWR,NMC,TX,TY,OMEGA,VD,VS,VG,
     1       IS,TOX,TT,INGES
C
C     NX AND NY ARE THE NO. OF GRID POINTS IN X AND Y
C
      NX=50
      NY=50
      NX1=NX-1
      NY1=NY-1

      CALL GRID(NX,NY,W,XWR,L,TX,TY,ND1E,ND2S,HX,HY)

      NSDS=ND1E+1
      NSDE=ND2S-1
      NSD=ND2S-ND1E
      TETA=Q/(CK*TT)
C
C     COX=OXIDE CAP. PER SQ. CM
C     NI=INTRINSIC CARRIER CONCENTRATION
```

```
      C     PSIB=BULK FERMI-LEVEL
      C     VT=THRESHOLD VOLTAGE
      C
            COX=EPSIO/TOX
            NI=3.88D16*TT**1.5*DEXP(-7.D3/TT)
            PSIB=(1/TETA)*(DLOG(NA/NI))
            VT=2*PSIB+(2.DO*DSQRT(EPS*Q*NA*PSIB)/COX)
            PRINT *,VT
            ALPHA=COX*(2*PSIB-VG)
            BETA=COX
            GAMMA=2*EPS*NA*Q
            DELTA=4*EPS*NA*Q*PSIB

            CALL MBLTY(VD,VS,L,COX,EPS,VG,PSIB,NA,MUN,RR,MUNH)
            PRINT *,MUN
      C
      C     TGDN=TANGENT OF HALL ANGLE
      C
            TGDN=MUNH*H

            CALL INGUES(VD,VS,TETA,ALPHA,BETA,GAMMA,DELTA,INGES)
            CALL FLBC(S,SS,SP,SSP,SM,SSM,R,SR,SO,SSO,
           1          DSP,DSM,DSO,DS,DR,TGDN)
            CALL MATRCO
            CALL PREMAT(NX,NX1,NY,NY1,NSD,NSDS,NSDE)
      C
      C     SLOR ITERATION BEGINS FOR THE SOLUTION OF U
      C
            JAJ=-1
            DO 98 ISOR=1,IS
            JAJ=-JAJ
            ICON=0
            DO 97 NNN=2,NY1
            N=NNN
            IF(JAJ.LE.0) N=NY1+2-NNN

            CALL FN(UO,NX1,NY1,NSD,ND1E,NSDS,NSDE,ND2S,
           1        N,R,SR,DR,F)
            CALL MATCA(NX1,N,DBI,BTI,ET,U,F)

            DO 96 M=2,NX1
            IF(DABS(U(M,N)/(UO(M,N))-1.DO).GE.1.D-5) ICON=1
            UO(M,N)=OMEGA*U(M,N)+(1.DO-OMEGA)*UO(M,N)
        96  CONTINUE
        97  CONTINUE
      C
      C     BOUNDARY VALUES ARE CALCULATED
      C
            DO 95 N=2,NY1
            UO(1,N)=SP(N)*UO(2,N+1)
           1       +SM(N)*UO(2,N-1)+ SO(N)*UO(3,N)
        95  UO(NX,N)=SSP(N)*UO(NX1,N+1)
           1         +SSM(N)*UO(NX1,N-1)+ SSO(N)*UO(NX1-1,N)
            IF(NSD.EQ.0) GO TO 98
            DO 94 M=NSDS,NSDE
        94  UO(M,50)=DSP(M)*UO(M+1,49)+DSM(M)*UO(M-1,49)
           1         +DSO(M)*UO(M,48)+DS(M)*UO(M,49)+DR(M)
        98  IF(ICON.EQ.0) GO TO 99
      C
      C     CALCULATION OF THE POTENTIAL DIST.
```

```
121      C
122        99  CALL NEWRAP(NX,NY,ALPHA,BETA,GAMMA,DELTA,TETA,VO,UO)
123      C
124      C      SURFACE CHARGE AND CURRENT DISTS. ARE CALCULATED
125      C
126            DO 103 N=1,NY
127            DO 103 M=1,NX
128       103  QN(M,N)=-(ALPHA+BETA*VO(M,N)+DSQRT(GAMMA*VO(M,N)+DELTA))/Q
129
130            CALL CRNT(UO,HX,HY,MUN,TGDN,JN,NX,NY,
131           1                  ND1E,NSDS,NSDE,ND2S,NSD,NMC,SENS)
132
133            WRITE (10) ((QN(M,N),M=1,NX),N=1,NY)
134            WRITE (11) ((UO(M,N),M=1,NX),N=1,NY)
135            WRITE (12) ((VO(M,N),M=1,NX),N=1,NY)
136            WRITE (13) ((JN(M,N),M=1,NX),N=1,NY1)
137            WRITE (15) (HX(M),M=1,NX1)
138            WRITE (15) (HY(N),N=1,NY1)
139            WRITE (20) ND1E,ND2S,MUN,TGDN
140            WRITE (20) NX,NY
141
142            PRINT*,SENS
143            PRINT *,ND1E,NSD,ND2S
144
145            STOP
146            END
147      C
148      C      GRID GENERATION
149      C
150            SUBROUTINE GRID(NX,NY,W,XWR,L,TX,TY,NW1,NW2,HX,HY)
151            IMPLICIT REAL*8(A-H,L,O-Z)
152            REAL*8 HY(50),HX(50),L,W1,W2,W3
153
154            W2=XWR*W
155            W1=(W-W2)/2.DO
156            W3=W1
157            NX1=NX-1
158            NY1=NY-1
159
160            CONST=NX/(DSQRT(W1)+DSQRT(W2)+DSQRT(W3))
161            WW1=CONST*DSQRT(W1)
162            WW2=CONST*DSQRT(W2)
163            WW3=CONST*DSQRT(W3)
164
165            NW1=WW1+0.7
166            NW2=WW2+WW1+0.7
167            NW3=WW1+WW2+WW3+0.7
168
169            NS=1
170            CALL NUGRID(NS,NW1,W1,TX,HX)
171            NS=NW1
172            CALL NUGRID(NS,NW2,W2,TX,HX)
173            NS=NW2
174            CALL NUGRID(NS,NW3,W3,TX,HX)
175            NS=1
176            CALL NUGRID(NS,NY,L,TY,HY)
177
178            RETURN
179            END
180      C
```

```
      C     NON-UNIFORM GRID
      C
            SUBROUTINE NUGRID(NS,N,XY,TXY,HXY)
            IMPLICIT REAL*8(A-H,L,O-Z)
            REAL*8 HXY(50),XY
            N1=N-1
            N2=N-(NS+1)
            SCA=4.DO*(TXY-1)/(N2)**2
            HXYS=0.DO
            DO 4 M=NS,N1
            HXY(M)=1.DO+SCA*(N1-M)*(M-NS)
        4   HXYS=HXYS+HXY(M)

            SCA=XY/HXYS
            DO 5 M=NS,N1
        5   HXY(M)=SCA*HXY(M)
            RETURN
            END
      C
      C     CALC. OF THE FIELD DEPENDENT MOBILITY
      C     MUN=DRIFT MOBILITY FOR ELECTRONS
      C     MUNH=HALL MOBILITY FOR ELECTRONS
      C
            SUBROUTINE MBLTY(VD,VS,L,COX,EPS,VG,PSIB,NA,MUN,RR,MUNH)
            IMPLICIT REAL*8(A-H,L,O-Z)
            REAL*8 MUNO,NA,MUN,MUNH

            MUNO=1.6D3
            EP=(VD-VS)/L
        6   EPA=EP/3.5D3
            EPB=(EP/7.4D3)**2
            ETR=(COX/EPS)*(VG-PSIB-VD/2)
            FEP=1.DO/DSQRT(1.DO+NA/(NA/3.5D2+3.D16) +
           1     (EPA**2)/(EPA+8.8DO)+EPB)
            GETR=1.DO/DSQRT(1.DO+1.539D-5*ETR)
            MUN=MUNO*FEP*GETR
            MUNH=MUN*RR

            RETURN
            END
      C
      C     GENERATION OF INITIAL GUESS FOR VARIABLES U AND V
      C
            SUBROUTINE INGUES(VD,VS,TETA,ALPHA,BETA,GAMMA,DELTA,INGES)
            IMPLICIT REAL*8(A-H,L,O-Z)
            REAL*8 GUESS(50,50)
            COMMON/KICSI/ UO(50,50),VO(50,50),H,NX,NX1,
           1        NY,NY1,HX(50),HY(50),NSD,NSDS,NSDE

            READ (14) ((GUESS(M,N),M=1,NX),N=1,NY)
            DO 1 N=1,NY
            DO 1 M=1,NX

            UD=ALPHA/TETA +(BETA/TETA-ALPHA)*VD
           1   -BETA*(VD**2)/2
           2   +DSQRT(GAMMA*VD+DELTA)/TETA
           3   -2*((GAMMA*VD+DELTA)**1.5)/(3*GAMMA)

            US=ALPHA/TETA +(BETA/TETA-ALPHA)*VS
           1   -BETA*(VS**2)/2
```

```
241           2   +DSQRT(GAMMA*VS+DELTA)/TETA
242           3   -2*((GAMMA*VS+DELTA)**1.5)/(3*GAMMA)
243
244           UO(M,N)=(UD-US)/NY1*(N-1)+US
245           IF(INGES.NE.1) GO TO 1
246           UO(M,N)=GUESS(M,N)
247         1 VO(M,N)=(VD-VS)/NY1*(N-1)+VS
248
249           RETURN
250           END
251       C
252       C     EVALUATION THE COEFFS. FOR FLOATING BOUNDARY MESHPOINTS
253       C
254           SUBROUTINE FLBC(S,SS,SP,SSP,SM,SSM,R,SR,SO,SSO,
255          1                DSP,DSM,DSO,DS,DR,TGDN)
256           IMPLICIT REAL*8(A-H,L,O-Z)
257           COMMON/KICSI/ UO(50,50),VO(50,50),H,NX,NX1,
258          1       NY,NY1,HX(50),HY(50),NSD,NSDS,NSDE
259           REAL*8 S(50),SM(50),SP(50),SS(50),SSM(50),SSP(50),R(50),
260          1       SR(50),SO(50),SSO(50),DSP(50),DSM(50),DSO(50),
261          2       DS(50),DR(50)
262
263           DO 1 N=2,NY1
264
265           R(N)=0.DO
266           S(N)=0.DO
267           SM(N)=(TGDN*(HX(1)+HX(2)))/(HY(N)+HY(N-1))
268           SP(N)=-SM(N)
269           SO(N)=1.DO
270
271           NX2=NX1-1
272           SR(N)=0.DO
273           SS(N)=0.DO
274           SSM(N)=-(TGDN*(HX(NX1)+HX(NX2)))/(HY(N)+HY(N-1))
275           SSP(N)=-SSM(N)
276         1 SSO(N)=1.DO
277
278           IF(NSD.EQ.0) GO TO 3
279           NY2=NY1-1
280
281           DO 2 M=NSDS,NSDE
282           DR(M)=0.DO
283           DS(M)=0.DO
284           DSM(M)=TGDN*(HY(NY1)+HY(NY2))/(HX(M)+HX(M-1))
285           DSP(M)=-DSM(M)
286         2 DSO(M)=1.DO
287
288         3 RETURN
289           END
290       C
291       C     COMPUTING OF THE COEFFS. IN THE DEVICE INTERIOR
292       C
293           SUBROUTINE MATRCO
294           IMPLICIT REAL*8(A-H,L,O-Z)
295           DIMENSION AT(50,50),BT(50,50),CT(50,50),
296          1          DT(50,50),ET(50,50),FT(50,50)
297           COMMON/KICSI/ UO(50,50),VO(50,50),H,NX,NX1,
298          1       NY,NY1,HX(50),HY(50),NSD,NSDS,NSDE
299           COMMON/MATR/    AT,BT,CT,DT,ET,FT
300
```

```
      DO 1 N=2,NY1
      DO 1 M=2,NX1

      AT(M,N)=2.DO/HY(N-1)/(HY(N)+HY(N-1))
      CT(M,N)=AT(M,N)*HY(N-1)/HY(N)
      DT(M,N)=2.DO/HX(M-1)/(HX(M)+HX(M-1))
      ET(M,N)=DT(M,N)*HX(M-1)/HX(M)
      BT(M,N)=-(AT(M,N)+CT(M,N)+DT(M,N)+ET(M,N))
    1 FT(M,N)=0.DO

      RETURN
      END
C
C     INVERSION OF THE COEFFS. B PRIOR TO SLOR(SEE [5])
C
      SUBROUTINE PREMAT(NX,NX1,NY,NY1,NSD,NSDS,NSDE)
      IMPLICIT REAL*8(A-H,L,O-Z)
      REAL*8 S(50),SM(50),SP(50),SS(50),SSM(50),
     1       SSP(50),R(50),SR(50),SO(50),SSO(50),
     2       DSP(50),DSM(50),DSO(50),DS(50),DR(50)
      DIMENSION AT(50,50),BT(50,50),CT(50,50),
     1       DT(50,50),ET(50,50),FT(50,50),
     2       BTI(50,50),DBI(50,50)
      COMMON/MATR/ AT,BT,CT,DT,ET,FT
      COMMON/PREM/ DBI,BTI,S,SS,SM,SSM,SP,SSP,R,SR,SO,SSO,
     1             DSP,DSM,DSO,DS,DR

      DO 1 N=2,NY1

      CE=DT(2,N)*SO(N)
      CA=DT(2,N)*SM(N)
      CB=DT(2,N)*S(N)
      CC=DT(2,N)*SP(N)

      ET(2,N)=ET(2,N)+CE
      AT(2,N)=AT(2,N)+CA
      BT(2,N)=BT(2,N)+CB
      CT(2,N)=CT(2,N)+CC

      CD=ET(NX1,N)*SSO(N)
      CA=ET(NX1,N)*SSM(N)
      CB=ET(NX1,N)*SS(N)
      CC=ET(NX1,N)*SSP(N)

      DT(NX1,N)=DT(NX1,N)+CD
      AT(NX1,N)=AT(NX1,N)+CA
      BT(NX1,N)=BT(NX1,N)+CB
      CT(NX1,N)=CT(NX1,N)+CC

    1 CONTINUE
      IF(NSD.EQ.0) GO TO 3

      DO 2 M=NSDS,NSDE

      DA=CT(M,NY1)*DSO(M)
      DB=CT(M,NY1)*DS(M)
      DD=CT(M,NY1)*DSM(M)
      DE=CT(M,NY1)*DSP(M)

      AT(M,NY1)=AT(M,NY1)+DA
```

```
361           BT(M,NY1)=BT(M,NY1)+DB
362           DT(M,NY1)=DT(M,NY1)+DD
363           ET(M,NY1)=ET(M,NY1)+DE
364
365         2 CONTINUE
366         3 CONTINUE
367
368           DO 6 N=2,NY1
369
370           BTI(2,N)=1.DO/BT(2,N)
371           DO 6 M=3,NX1
372           DBI(M,N)=DT(M,N)*BTI(M-1,N)
373           BT(M,N)=BT(M,N)-(DBI(M,N)*ET(M-1,N))
374           BTI(M,N)=1.DO/BT(M,N)
375         6 CONTINUE
376
377           RETURN
378           END
379       C
380       C     CALCULATION OF RHS OF SLOR EQN.
381       C
382           SUBROUTINE FN(UO,NX1,NY1,NSD,ND1E,NSDS,NSDE,ND2S,
383          1              N,R,SR,DR,F)
384           REAL*8  UO(50,50),R(50),SR(50),DR(50),
385          2        AT(50,50),CT(50,50),BT(50,50),
386          3        DT(50,50),ET(50,50),FT(50,50),
387          4        F(50),FD,FE,FA,FC,DFC
388           COMMON/MATR/ AT,BT,CT,DT,ET,FT
389
390           IF(NSD.NE.0) GO TO 4
391           DO 1 M=2,NX1
392
393           FA=AT(M,N)*UO(M,N-1)
394           FC=CT(M,N)*UO(M,N+1)
395           F(M)=FT(M,N)-FA-FC
396         1 CONTINUE
397
398           FD=DT(2,N)*R(N)
399           FE=ET(NX1,N)*SR(N)
400           F(2)=F(2)-FD
401           F(NX1)=F(NX1)-FE
402
403           RETURN
404
405         4 DO 6 M=2,ND1E
406
407           FA=AT(M,N)*UO(M,N-1)
408           FC=CT(M,N)*UO(M,N+1)
409           F(M)=FT(M,N)-FA-FC
410
411         6 CONTINUE
412           DO 5 M=ND2S,NX1
413
414           FA=AT(M,N)*UO(M,N-1)
415           FC=CT(M,N)*UO(M,N+1)
416           F(M)=FT(M,N)-FA-FC
417
418         5 CONTINUE
419
420           FD=DT(2,N)*R(N)
```

```
421           FE=ET(NX1,N)*SR(N)
422           F(2)=F(2)-FD
423           F(NX1)=F(NX1)-FE
424
425           DO 2 M=NSDS,NSDE
426           IF(N.NE.NY1) GO TO 7
427
428           DFC=CT(M,N)*DR(M)
429           FA=AT(M,N)*UO(M,N-1)
430           F(M)=FT(M,N)-FA-DFC
431           GO TO 2
432
433         7 FA=AT(M,N)*UO(M,N-1)
434           FC=CT(M,N)*UO(M,N+1)
435           F(M)=FT(M,N)-FA-FC
436
437         2 CONTINUE
438           RETURN
439           END
440     C
441     C     SOLUTION OF U AT EACH MESHPOINT
442     C
443           SUBROUTINE MATCA(NX1,N,DBI,BTI,ET,U,F)
444           REAL*8 AF,CW,DBI(50,50),BTI(50,50),ET(50,50),
445          1       U(50,50),F(50)
446
447           DO 1 M=3,NX1
448
449           AF=DBI(M,N)*F(M-1)
450           F(M)=F(M)-AF
451
452         1 CONTINUE
453           U(NX1,N)=BTI(NX1,N)*F(NX1)
454
455           DO 6 K=3,NX1
456
457           M=NX1-K+2
458           CW=ET(M,N)*U(M+1,N)
459           U(M,N)=BTI(M,N)*(F(M)-CW)
460
461         6 CONTINUE
462           RETURN
463           END
464     C
465     C     CALC. OF V USING NEWTON-RAPHSON
466     C
467           SUBROUTINE NEWRAP(NX,NY,ALPHA,BETA,GAMMA,DELTA,TETA,VO,UO)
468           IMPLICIT REAL*8(A-H,L,O-Z)
469           REAL*8 VO(50,50),UO(50,50)
470
471           DO 1 N=1,NY
472           DO 1 M=1,NX
473           DO 2 INR=1,100
474
475           IF(VO(M,N).LE.0.D0) VO(M,N)=0.D0
476           FV=UO(M,N)-ALPHA/TETA -(BETA/TETA-ALPHA)*VO(M,N)
477          1   +BETA*(VO(M,N)**2)/2
478          2   -DSQRT(GAMMA*VO(M,N)+DELTA)/TETA
479          3   +2*((GAMMA*VO(M,N)+DELTA)**1.5)/(3*GAMMA)
480
```

```
      FPV=ALPHA-BETA/TETA
     1   +BETA*VO(M,N)
     2   -GAMMA/(DSQRT(GAMMA*VO(M,N)+DELTA))/TETA/2
     3   +DSQRT(GAMMA*VO(M,N)+DELTA)

      IF(DABS(FV).LE.1.D-19) GO TO 1
    2 VO(M,N)=VO(M,N)-FV/FPV
      IF(VO(M,N).LE.0.D0) VO(M,N)=0.D0

    1 CONTINUE
      RETURN
      END
C
C     CALC. OF THE CURRENT DIST. IN THE CHANNEL,
C     THE DRAIN CURRENTS AND EVALUATION OF THE
C     DEVICE SENSITIVITY (DEFINED IN TERMS OF
C     THE CURRENT IMBALANCE IN THE DRAINS).
C     A CHECK FOR THE CONSERVATION OF TERMINAL
C     CURRENTS IS MADE.
C
      SUBROUTINE CRNT(UO,HX,HY,MUN,TGDN,JN,NX,NY,
     1                ND1E,NSDS,NSDE,ND2S,NSD,NMC,SENS)
      IMPLICIT REAL*8(A-H,L,O-Z)
      REAL*8 UO(50,50),HX(50),HY(50),MUN,JN(50,50)

      NX1=NX-1
      NY1=NY-1

      MS=2
      ML=NX
      DO 1 N=1,NY1
    1 CALL JNY(JN,UO,HX,HY,N,MS,ML,MUN,TGDN)

      DO 2 N=1,NY1
      DO 2 M=1,NX
    2 JN(M,N)=JN(M,N)/JN(NX,N)

      MS=2
      ML=NX
      N=1
      CALL YCRNT(CRNT,UO,HX,HY,N,MS,ML,MUN,TGDN)
      SCR=CRNT

      N=NY1
      MS=2
      ML=ND1E
      CALL YCRNT(CRNT,UO,HX,HY,N,MS,ML,MUN,TGDN)
      DCR1=CRNT

      MS=ND2S+1
      ML=NX
      CALL YCRNT(CRNT,UO,HX,HY,N,MS,ML,MUN,TGDN)
      DCR2=CRNT

      CHECK=SCR-DCR1-DCR2
      PRINT*,SCR,DCR1,DCR2,CHECK
      SENS=(DCR1-DCR2)/(DCR1+DCR2)

      RETURN
      END
```

```
      SUBROUTINE JNY(JN,UO,HX,HY,N,MS,ML,MUN,TGDN)
      IMPLICIT REAL*8(A-H,L,O-Z)
      REAL*8 UO(50,50),HX(50),HY(50),JN(50,50),MUN

      JN(1,N)=0.DO
      DO 20 M=MS,ML
      AUO=(UO(M-1,N)+UO(M,N))/2.DO
      AU1=(UO(M-1,N+1)+UO(M,N+1))/2.DO
      DYU=(AU1-AUO)/HY(N)
      AUO=(UO(M-1,N)+UO(M-1,N+1))/2.DO
      AU1=(UO(M,N)+UO(M,N+1))/2.DO
      DXU=(AU1-AUO)/HX(M-1)
   20 JN(M,N)=JN(M-1,N)+(DYU+TGDN*DXU)*MUN*HX(M-1)/(1.DO+TGDN**2)

      RETURN
      END

      SUBROUTINE YCRNT(CRNT,UO,HX,HY,N,MS,ML,MUN,TGDN)
      IMPLICIT REAL*8(A-H,L,O-Z)
      REAL*8 UO(50,50),HX(50),HY(50),MUN

      CRNT=0.DO
      DO 20 M=MS,ML
      AUO=(UO(M-1,N)+UO(M,N))/2.DO
      AU1=(UO(M-1,N+1)+UO(M,N+1))/2.DO
      DYU=(AU1-AUO)/HY(N)
      AUO=(UO(M-1,N)+UO(M-1,N+1))/2.DO
      AU1=(UO(M,N)+UO(M,N+1))/2.DO
      DXU=(AU1-AUO)/HX(M-1)
   20 CRNT=CRNT+(DYU+TGDN*DXU)*MUN*HX(M-1)/(1.DO+TGDN**2)

      RETURN
      END
```